Improving Surface Plasmon Resonance Sensor and Nanoaperture Optical Tweezers for Biomolecule Analysis

by

Elham Babaei

B.Sc., University of Tehran, 2011

M.Sc., University of Tehran, 2015

A Dissertation Submitted in Partial Fulfillment of the

Requirements for the Degree of

DOCTOR OF PHILOSOPHY

in the Department of Electrical Engineering and Computer Sciences

University of Victoria

Improving Surface Plasmon Resonance Sensor and Nanoaperture Optical Tweezers for Biomolecule Analysis

by

Elham Babaei

B.Sc., University of Tehran, 2011

M.Sc., University of Tehran, 2015

Supervisory Committee

Dr. Reuven Gordon , Supervisor

(Department of Electrical Engineering and Computer Sciences)

Dr. Jens Bornemann, Departmental Member

(Department of Electrical Engineering and Computer Sciences)

Dr. Josh W Giles, Outside Member

(Department of Mechanical Engineering)

Abstract

This thesis explores innovative approaches to improve sensitivity of surface plasmon resonance (SPR) sensors and nanoaperture optical tweezers (NOT) technique for biomolecule analysis.

A significant enhancement in the sensitivity of surface plasmon sensors by 3.3 times and a quadrupling of resolution are presented compared to conventional SPR sensors. The optimal design parameters for generating short-range modes on a gold film (period: 250 nm, gap size: 40 nm, thickness: 10 nm) are identified using rigorous coupled wave analysis (RCWA) to achieve minima for incident angle and wavelength, following the same configuration as conventional SPR sensors which employ a standard 50 nm thick gold film and Kretschmann-Raether coupling with a light wavelength of 760 nm. Finite difference time domain simulations confirm the correspondence of short-range surface plasmon modes to localized surface plasmons (LSP). By using the field confinement capability of short-range surface plasmon (SRSP) modes, higher sensitivity in SPR is achieved, facilitating the characterization of biomolecule interactions.

The second study introduces novel approaches to enhance the colloidal lithography technique commonly used. The simplification of nanoaperture detection and characterization is achieved by charge coupled device (CCD) images and polarization-dependent transmission, eliminating the need for a scanning electron microscope (SEM), which otherwise makes the process time-consuming and costly. By employing polarization analysis, configurations of the holes, including single, trimers, and other

clusters, along with their orientations, can be identified. Furthermore, changing the substrate of the sample from glass to polyvinyl chloride (PVC) results in a sevenfold decrease in the minimum required power for trapping 20 nm polystyrene beads, attributed to reduced surface repulsion. Lastly, the utilization of tape exfoliation instead of sonication in ethanol is presented, which preserves the uniform apertures on the gold surface.

In the third study, an innovative method is presented for rapidly trapping single, unlabeled proteins in a NOT system. By integrating the principles of dielectrophoresis and NOT, a significant 10-fold reduction in trapping time is achieved, along with the successful trapping of Neuropeptide Y, which has a molecular weight of only 4 kDa. This improvement is obtained by placing the counter electrode on a glass substrate outside the solution, thereby creating a fringe field that enhances the trapping performance. Placing the counter electrode directly in the solution does not generally lead to faster protein trapping. However, it is observed that electrophoresis can expedite the trapping of polystyrene spheres, especially with increasing applied voltage. This effect is attributed to changes in the repulsive surface potential. This voltage-dependent trapping enhancement is only observed with positive applied voltages.

Furthermore, in other projects, extraordinary acoustic Raman (EAR) spectroscopy was used to trap a 20 nm polystyrene sphere. An optimal power level is observed for exciting the vibrational modes in the nanoparticle and simultaneously obtaining sharp peaks in the normalized standard deviation (NSTD) of the noise versus beat fre-

quency spectrum. Additionally, PR65, which is a subunit of the protein phosphatase 2A (PP2A), is trapped, and its acoustic vibration modes are excited using the EAR technique. The experimental results demonstrate that the vibrational modes occur at frequencies of 9.29 GHz, 19.28 GHz, 30.23 GHz, and 41.18 GHz, which align with the results obtained through normal mode analysis (NMA). It is noteworthy that this technique offers the advantage of being single-molecule and label-free compared to conventional methods used for biomolecule characterization. The characterization of PR65 serves as a valuable model for understanding the structural regulation of various repeat proteins.

Table of Contents

List of Figures

Glossary

Common Abbreviations

Abbreviation	Meaning
APD	avalanche photodiode
RCWA	rigorous coupled wave analysis
SPR	surface plasmon resonance
LRSP	long range surface plasmon
SRSP	short range surface plasmon
TM	transverse magnetic
TE	transverse electric
IMI	insulator metal insulator
NOT	nano-aperture optical tweezers
SIBA	self induced back action
MST	Maxwell stress tensor
SNR	signal to noise ratio
EAR	extraordinary acoustic Raman
STD	standard deviation
ISO	isolator
FPC	polarization controller
DI	dichroic mirror
PP2A	protein phosphatase 2A
PVC	polyvinyl chloride
BE	beam expander
CCD	charge-coupled device
CW	continuous wave
DNH	double nanohole
FDTD	finite-difference time-domain
FIB	focused ion beam
HWP	half-wave plate
LP	linear polarizer
LSP	localized surface plasmon

Glossary

Common Abbreviations

MO	microscope objective
ODF	optical density filter
OI	oil immersion
SEM	scanning electron microscope
SPP	surface plasmon polariton

Common Abbreviations

Symbols	Meaning
β	propagation constant
ϵ_0	vacuum permittivity
ϵ_d	dielectric permittivity
ϵ_m	metal permittivity
η	quantum yield
Φ	phase of reflection
λ	wavelength
ρ	electron density
ω	angular frequency

ACKNOWLEDGEMENTS

I would like to express my sincere gratitude and appreciation to my supervisor, Prof. Reuven Gordon, for his invaluable guidance and support throughout the journey of completing this thesis. I am truly grateful for his unwavering availability to answer my questions, his up-to-date knowledge in the field, and his exceptional ideas, which have significantly enriched my research. I would also like to express my gratitude to Laura Itzhaki's group at the University of Cambridge and Ivet Bahar's group at the University of Pittsburgh for their valuable collaboration, which was essential for my research. I would also like to extend my thanks to the members of my supervisory committee, Prof. Jens Bornemann and Prof. Josh Giles, for their help in shaping my dissertation path. I am also deeply thankful to my lab mates, Dr. Demelza Wright, Dr. Ghazal Hajisalem, Dr. Mirali Shariatdoust, Michael Dobinson, and Shohei Iwamoto, for their support, collaboration, and assistance in various aspects of my work. Furthermore, I would like to acknowledge the support and encouragement from my family and friends who have been a source of strength and motivation throughout this endeavor. Lastly, I would like to acknowledge the assistance provided by ChatGPT during the writing of my thesis. The use of this AI model helped me generate content and explore different ideas. However, it is important to note that all the information generated by ChatGPT was thoroughly checked and revised by myself to ensure its accuracy and appropriateness for my thesis.

DEDICATION

To all those who believe in the transformative power of knowledge, the pursuit of scientific understanding, and the sheer joy of exploring the wonders of our world.

Chapter 1

Introduction

This thesis explores novel approaches to enhance sensitivity and trapping techniques for protein analysis. By employing local resonances from periodically arranged short-range modes in a configuration similar to traditional SPR sensors, the sensitivity can be increased threefold, and the resolution can be quadrupled, considering shot noise. Furthermore, applying certain ideas to existing sample fabrication and measurement procedures can enhance the trapping process. In the conventional colloidal lithography process used for sample fabrication, the detection of double nanohole (DNH) structures can be simplified by utilizing CCD images and polarization-dependent transmission, eliminating the need for expensive and time-consuming scanning electron microscopy (SEM) images. Additionally, tape exfoliation provides a more uniform removal of polystyrene beads without the damage that can occur with sonication or chemical methods. Changing the sample substrate from glass to vinyl significantly reduces surface repulsion and enables faster particle trapping. Time to trap can be increased tenfold by integrating dielectrophoresis and NOT techniques, utilizing voltage, and creating fringe fields to overcome the diffusion limit. Lastly, the thesis demonstrates the feasibility of utilizing EARS to identify the vibrational modes of PR65, a subunit of PP2A. These findings align with the results obtained through normal mode analysis, thereby providing a deeper understanding of the structural regulation of repeat proteins.

1.1 Motivation

Three works have been completed in this thesis. Here, the motivation for each work is discussed.

1.1.1 Increasing sensitivity in SPR biosensors

The SPP is exponentially bound to the surface, which gives good sensitivity to changes in refractive index near the surface, and this is the theory behind the SPR sensors. The sensitivity and limits of detection of the various SPR sensors show variations depending on the method employed to excite the surface plasmon [1, 2, 3, 4]. However, they can be adjusted to the order of 10^{-5} in bulk refractive index changes, corresponding to a detection limit of 1–5 pg mm^{-2} for biomolecules adsorbed at the sensor surface. Nonetheless, this resolution proves inadequate for directly detecting low concentrations of small molecules, necessitating detection limits of 0.1 pg mm^{-2} or lower [5]. The engineering of these commercial systems takes into account several factors, including the wavelength and type (LED vs. laser) of the light source, the type of metal used, the thickness of the metal layer, the detector type (single channel vs. detector array), data acquisition parameters (dynamic range, analog-to-digital conversion, and acquisition time), and cost. Nonetheless, a potential exists to improve surface sensitivity and resolution by employing short-range surface plasmon modes alongside localized surface plasmon (LSP) resonances. This study aims to leverage the existing commercial SPR platform and explore the application of SRSP modes in sensing. By incorporating a rectangular stripe grating on a 10 nm thick gold film, a 3.3 times higher surface sensitivity and four-fold improvement in resolution are achieved. Thus, using these chips is promising for more sensitive SPR sensing in future applications.

1.1.2 Improving the colloidal lithography technique for fabrication of double nanohole samples

Although many existing methods involve labeling or tethering, which disrupts natural function, nanohole optical tweezers have shown great potential in studying nanoparticles and various molecular interactions without the need for modifications of the nanoparticles. However, the fabrication and localization of double nanohole (DNH) apertures have been limited to specialized facilities and require additional registration steps. The second work aims to overcome these limitations by introducing a polarization and transmission-dependent technique for localizing and characterizing DNHs on a substrate and determining their orientation. Additionally, using low-repulsion substrates and tape fabrication is explored to enhance trapping efficiency and preserve high-quality apertures. These advancements make DNH aperture trapping more accessible and efficient for various applications.

1.1.3 Decreasing time to trap in nanoaperture optical trapping

In addition to fabrication, the trapping process is slow due to diffusion limitations. The trapping time duration can be from minutes to even hours. This significantly complicates the study of particles, making it more difficult and time-consuming. The third work aims to overcome these limitations by introducing a novel approach using NOTs and electric fields. By placing the counter electrode on the dielectric substrate opposite the solution, a fringe field is created, significantly reducing trapping time for unlabeled proteins. This innovative technique enhances the speed and efficiency of single protein analysis, opening new avenues for studying biomolecular dynamics in physiological environments.

1.2 Organization of the dessertation

This dissertation consists of three papers, each incorporating substantial contributions from the author. The forthcoming sections will delve into these papers, along with additional research that remains unpublished in a journal but has been presented at two conferences.

1.3 Contributions

1.3.1 Improving the sensitivity of existing surface plasmon resonance systems with grating-coupled short-range surface plasmons

E.B. was responsible for calculations, simulations, and analysis tasks. Z.S. observed the entire procedure and helped with preparing the figures. R.G. conceived the method, provided assistance with data analysis, and took the lead in writing the manuscript.

1.3.2 Accessible high-performance double nanohole tweezers

E.B. conducted nanofabrication and measurements associated with modifying the substrate. G.H. performed measurements, analysis, and simulation regarding polarization-dependent DNH localization and orientation and wrote the manuscript. M.D. performed the fabrication process for tape exfoliation. S.I. provided assistance in writing the manuscript. J.E. helped with measurements related to polarization-dependent DNH localization. M.S. and L.S. provided the PR65 protein. R.G. devised the experiments, assisted with data analysis, and contributed to writing the manuscript.

1.3.3 Fringe dielectrophoresis nanoaperture optical trapping with an order of magnitude speed-up for unmodified proteins

E.B. was responsible for conducting all nanofabrication, measurements, and analysis tasks, as well as writing the manuscript. D.W. provided assistance with data analysis and also contributed to manuscript writing. R.G. devised the experiments, provided guidance in data analysis, and participated in manuscript writing.

Chapter 2

Theoretical foundations, methodology, and experimental techniques

2.1 Introduction

This chapter of the thesis delves into a comprehensive explanation of the fundamental principles and concepts underlying the projects. It provides a detailed account of the theoretical framework that forms the basis of the research, elucidating the methodologies employed and the experimental techniques utilized. This chapter serves as a vital resource for understanding the groundwork and approach adopted throughout the thesis, shedding light on the theoretical underpinnings and the practical aspects of the projects undertaken.

2.2 Plasmonics

In this section, the surface plasmon polariton SPP and the dispersion relation for the propagation of SPPs at the interface are explained. Additionally, two methods of phase matching, namely prism coupling and grating coupling, are introduced to excite the SPPs at the planar interface. The RCWA is also explained to determine the interaction of light with periodic structures. Furthermore, important parameters that demonstrate the efficiency of SPR sensors, such as resolution and sensitivity, are defined.

2.2.1 Surface plasmon polaritons at a single interface

By considering the transverse magnetic (TM) modes and defining the direction of the propagation of light along the x axis as can be seen in Figure 2.1, the following relations can be obtained from Maxwell's equations:

$$E_x = -i\frac{1}{\omega\epsilon_0\epsilon}\frac{\partial H_y}{\partial z} \tag{2.1a}$$

$$E_z = -\frac{\beta}{\omega\epsilon_0\epsilon}H_y \tag{2.1b}$$

$$\frac{\partial^2 H_y}{\partial z^2} + (k_0^2\epsilon - \beta^2)H_y = 0, \tag{2.1c}$$

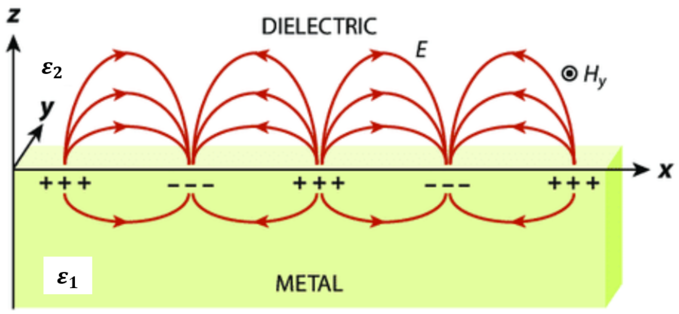

Figure 2.1: Surface plasmon polariton at the interface of metal and dielectric . [6]Copyright ©2017, Annual Reviews

and for transverse electric (TE) modes:

$$H_x = i\frac{1}{\omega\mu_0}\frac{\partial E_y}{\partial z} \tag{2.2a}$$

$$H_z = \frac{\beta}{\omega\mu_0}E_y \tag{2.2b}$$

$$\frac{\partial^2 E_y}{\partial z^2} + (k_0^2\epsilon - \beta^2)E_y = 0 \tag{2.2c}$$

where μ_0 and ϵ_0 are the permeability and permitivity of free space. k_0 is the wave vector in free space and β is propagation constant. We consider half of the space (z $>$ 0) with the positive real dielectric constant of ϵ_2 and the other half ($z < 0$) filled with metal with the dielectric function of $\epsilon_1(\omega)$. Due to metallic characteristics, we know $Re[\epsilon_1] < 0$. Using the equation set of 2.1, we can derive the following equations:

$$H_y = A_2 e^{i\beta x} e^{-k_2 z} \tag{2.3a}$$

$$E_x(z) = iA_2\frac{\beta}{\omega\epsilon_0\epsilon_2}k_2 e^{i\beta x} e^{-k_2 z} \tag{2.3b}$$

$$E_z(z) = -A_2\frac{\beta}{\omega\epsilon_0\epsilon_2}e^{i\beta x} e^{-k_2 z} \tag{2.3c}$$

for $z < 0$ and,

$$H_y = A_1 e^{i\beta x} e^{k_1 z} \tag{2.4a}$$

$$E_x(z) = -iA_1 \frac{1}{\omega\epsilon_0\epsilon_1} k_1 e^{i\beta x} e^{k_1 z} \tag{2.4b}$$

$$E_z(z) = -A_1 \frac{\beta}{\omega\epsilon_0\epsilon_1} e^{i\beta x} e^{k_1 z} \tag{2.4c}$$

for $z > 0$.

Considering continuity of electric field flux (D) and magnetic field at the interface we obtain $A_1 = A_2$, so:

$$\frac{k_2}{k_1} = -\frac{\epsilon_2}{\epsilon_1} \tag{2.5}$$

We should note that we only have surface waves when the signs of the real components of the dielectric permittivity are opposite on the two sides. By considering Equation 2.1 for H_y:

$$k_1^2 = \beta^2 - k_0^2\epsilon_1 \tag{2.6a}$$

$$k_2^2 = \beta^2 - k_0^2\epsilon_2 \tag{2.6b}$$

from the above equations and Equation 2.5, we have the following dispersion relation for propagating of SPPs at the interface:

$$\beta = k_0\sqrt{\frac{\epsilon_1\epsilon_2}{\epsilon_1+\epsilon_2}} \tag{2.7}$$

from Equations 2.2a - 2.2c, for electric field components:

$$E_y(z) = A_2 e^{i\beta x} e^{-k_2 z} \tag{2.8a}$$

$$H_x(z) = -iA_2\frac{\beta}{\omega\mu_0}k_2 e^{i\beta x} e^{-k_2 z} \tag{2.8b}$$

$$H_z(z) = A_2\frac{\beta}{\omega\mu_0} e^{i\beta x} e^{-k_2 z} \tag{2.8c}$$

for $z > 0$ and,

$$E_y(z) = A_1 e^{i\beta x} e^{k_1 z} \tag{2.9a}$$

$$H_x(z) = iA_1\frac{\beta}{\omega\mu_0}k_1 e^{i\beta x} e^{k_1 z} \tag{2.9b}$$

$$H_z(z) = A_1\frac{\beta}{\omega\mu_0} e^{i\beta x} e^{k_1 z} \tag{2.9c}$$

for $z < 0$. Applying the boundary conditions for the electric and magnetic field at the interface:

$$A_1(k_1+k_2) = 0 \tag{2.10}$$

To have confinement, the real part of k_1 and k_2 should be both positive, meaning that

$A_1 = A_2 = 0$. Therefore, there are no surface plasmon polaritons for TE modes.

2.2.2 Extraction of surface plasmon polaritons (SPPs) at planar interfaces

This chapter introduces two important methods: prism and grating coupling. These methods are used for phase matching to excite SPPs.

Prism coupling

At the interface of the metal and dielectric, SPP cannot occur since $\beta > k$, where k is the wave vector in the dielectric medium. Also, $k_x = k\sin(\theta)$ is smaller than the SPP propagation constant β for any angle to the surface normal, θ, even the grazing angle. So, phase matching never happens. However, phase matching can be achieved when a metal layer is sandwiched between two dielectric layers with different dielectric constants. In this way, the momentum of $k_x = k\sqrt{\epsilon}\sin(\theta)$ that is related to the reflected incident light from the higher index dielectric side in the shape of a prism can excite the SPP at the interface of a metal and lower index dielectric, which is air here as it can be seen in Figure 2.2. A dip can be seen in the reflected light when an SPP occurs since most of the light propagates on the surface. Therefore, coupling occurs by tunneling the excitation beam into the metal/air interface, which is known as attenuated total internal reflection. There are two configurations for prism coupling. One is the Kretschmann method [7] in which metal is evaporated onto one side of the glass prism. Incident light with an angle greater than the critical angle of total internal reflection can excite the SPP at the metal-air interface by tunneling. The other method is Otto configuration [8]. Excitation of SPP, through mode matching, is a leaky process since there is always absorption in the metal and radiation through the prism. When the reflected part of the excitation beam and leakage radiation have destructive interference, the minimum intensity can be seen in the reflected light. For an optimum thickness of the metal, destructive interference is zero, so the leakage radiation can be eliminated from the reflected beam intensity.

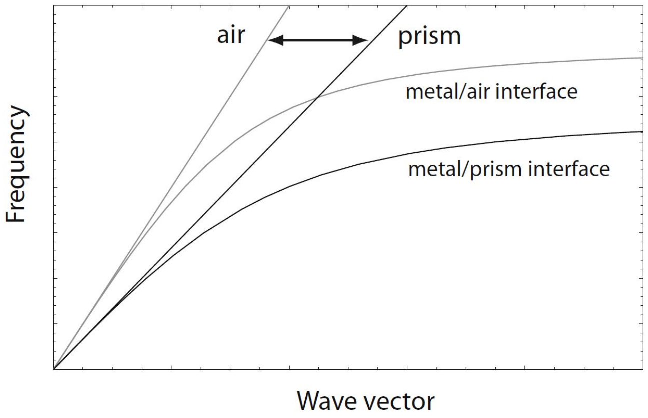

Figure 2.2: Prism coupling and dispersion relation curves [9]Copyright ©2007, Springer

Grating Coupling

Another way to create mode coupling at the interface of metal and dielectric is to create grooves on the metal with a specified lattice constant. Fulfilling the following condition, mode matching can take place at the interface [9]:

$$\beta = k \sin(\theta) \pm \ \nu g \tag{2.11}$$

In the above condition, $g = \frac{2\pi}{a}$ is the reciprocal vector of grating, a is the lattice constant, and $\nu = (1, 2, 3, ...)$. Like the prism coupling, excitation of SPP can be detected when there is a minimum in the reflected light. As shown in Figure 2.3 $k_{||}$ equals to ksin(θ).

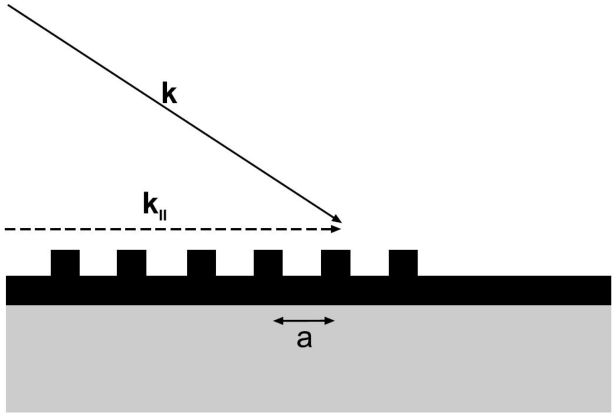

Figure 2.3: Phase matching of light to the SPP using grating configuration. k shows the wave vector of incident light and $k_{||}$ is it's component parallel to the surface [9] Copyright ©2007, Springer

Rigorous coupled wave analysis (RCWA)

Rigorous Coupled Wave Analysis (RCWA) is a method for studying electromagnetic waves in periodic structures. RCWA solves Maxwell's equations in Fourier space for layered structures along the Z direction. It uses matrices, eigenvectors, and eigenvalues to compute electromagnetic field solutions. Mode coefficients and exponential factors depict mode propagation. RCWA is suited for structures with moderate periodicity and index contrast, and it models interactions between layers using scattering matrices. The method involves calculating parameters within each layer, linking layers with boundary conditions, and deriving mode coefficients for wave propagation. So, by applying that, the reflection and transmission coefficient at the upper and lower space can be related to each other and be determined. The RCWA codes were used from an open-source package prepared by Bo Zhao at the Georgia Institute of Technology.

2.2.3 SRSP, LRSP, and the motivation for utilizing SRSP in SPR sensor

In this section, the short-range surface plasmon (SRSP) and long-range surface plasmon (LRSP) are explained, and the reasons why SRSP can be used as a modification to existing SPR sensors are discussed.

Long-range surface plasmon: Long-range SPPs refer to the conventional SPPs that are excited in systems with a thicker metal film (e.g., 50 nm thick gold film). These SPPs have a smaller propagation constant and are less confined to the metal surface. They are typically used in commercial SPR biosensors [10].

Short-range surface plasmon: Short-range SPPs (SRSPs) are a type of SPP that can be obtained by using insulator-metal-insulator (IMI) structures with a reduced metal thickness (e.g., 10 nm gold film). These SRSPs are more tightly confined to the metal surface, leading to increased sensitivity to changes in the refractive index near the surface [11].

The motivation for modifying the existing thin film SPR sensor by making the film thinner and adding a grating is to achieve even greater surface sensitivity. By reducing the gold film thickness and employing a periodic grating structure, light can be coupled into the SRSP modes while the same prism coupling configuration is retained. The grating-assisted coupling enhances the coupling efficiency and allows for better excitation of the SRSP modes. The LSP resonances arising from the propagation and reflection of the SRSP modes are utilized to improve the coupling.

In this context, the objective is to address the problem of designing a more sensitive SPR sensor chip. This goal can be achieved using the SRSP modes and LSP resonances within the existing commercial SPR platform. The application of RCWA enables the determination of the modified sensor's surface sensitivity, consisting of a 10 nm thick gold film and a rectangular stripe grating configuration. Importantly, if the modified chip operates within the same range as the existing devices, it will facilitate integration and compatibility with the well-established SPR technology.

The same angle and wavelength as the existing devices can be utilized to ensure compatibility and easy integration with widely used commercial SPR systems in laboratories worldwide. By adopting these parameters, the modified chip can effectively interface with the established commercial SPR systems, thereby enhancing its practicality and accessibility.

2.2.4 Resolution, sensitivity, Q-factor

In this section, the important parameters in SPR sensors are discussed both conceptually and mathematically.

Resolution

Resolution refers to the ability of a sensor to distinguish small changes or variations in a measured quantity. In the context of this work, resolution refers to the ability of the sensor chip to detect and differentiate changes in the refractive index near the surface. Mathematically, resolution can be calculated by determining the smallest detectable change in the measured quantity that can be distinguished from the noise.

Following equations show how resolution can be obtained in the SPR sensors.

$$f_{\text{noise}}(\theta, 0) = f(\theta, 0) + \text{noise} \tag{2.12}$$

$$A = \int \left(f(\theta, \Delta n) - f_{\text{noise}}(\theta, 0) \right)^2 d\theta \tag{2.13}$$

In equation 2.12 f shows the function of reflection versus incident angle in the SPR sensor. Δn shows the difference between the refractive index of water and the refractive index of the adhesion layer on the gold surface. f_{noise} shows the function of f when shot noise and digitization noise are applied to it. Shot noise arises due to the statistical fluctuations in the number of photons detected by the sensor. Shot noise is inherent in any optical detection system and is caused by the discrete nature of light. To find the resolution in the sensor, we need to find the amount of Δn, which makes the A minimum. In this way, we find the minimum detectable Δn.

Sensitivity

Sensitivity refers to the ability of the sensor to respond to changes in the refractive index near the surface. It measures how much the sensor output changes in response to a given change in the measured quantity. In this case, the sensitivity of the sensor chip is specifically related to changes in the refractive index of an adlayer on the gold film. Sensitivity can be calculated by measuring the change in the output signal of the sensor for a known change in the input quantity.

Q-factor

The highest Q factor (quality factor) does not always give the best sensor because the Q factor measures the sharpness or narrowness of a peak. While a high Q factor can provide a narrow peak and potentially enhance the sensor's ability to detect small changes, it also makes the system more sensitive to noise and environmental fluctuations. Therefore, in practical applications, a balance needs to be struck between a high Q factor and the overall performance of the sensor, taking into account factors such as noise, stability, and ease of fabrication. In some cases, a broader resonance peak may actually lead to better overall performance and resolution.

2.3 Optical trapping setup and EARs fundamentals

This section provides an explanation of the NOTs principle. It covers the setup fundamentals, the application of aperture forces on particles, and the process of trapping. Additionally, it outlines the crucial parameters for assessing efficiency and analyzing the trapping signal. The section then proceeds to describe the functioning of the Extraordinary Acoustic Raman spectroscopy (EARs) method used to identify the vibrational modes of individual nanoparticles. It introduces PR65 as the specific target for obtaining EARs data and highlights the significance of studying it.

2.3.1 Optical trapping setup

In 1986, Arthur Ashkin used a single beam to trap single nanoparticles [12, 13]. In the conventional trapping, in the Rayleigh regime ($d << \lambda$) [12], one of the effective forces that is applied to a particle in a trap, is related to the scattering in the direction of propagation of the light, and can be presented as [12]:

$$F_{\text{scat}} = \frac{I_0}{c} \frac{128\pi^5 (\frac{d}{2})^6}{3\lambda^4} (\frac{{n_p}^2 - {n_m}^2}{{n_p}^2 + 2{n_m}^2})^2 n_m \propto \frac{d^6}{\lambda^4} \tag{2.14}$$

where I_0 is the light intensity, d is the diameter of the particle, λ is the wavelength of the laser, n_p and n_m are particle and medium refractive index, respectively. The other force is associated with the gradient of the electric field, is named F_{grad} and is formulated as follows [14], [15]:

$$F_{\text{grad}} = \frac{1}{2} n_m \alpha \nabla \mid E \mid^2 = \frac{n_m^3 (\frac{d}{2})^3}{2} (\frac{{n_p}^2 - {n_m}^2}{{n_p}^2 + 2{n_m}^2})^2 \nabla \mid E \mid^2 \tag{2.15}$$

where α is the polarizability of the particle. From the formulae for the particles in the Rayleigh regime, the scattering field can be neglected, and the required power is proportional to the inverse third power of diameter according to Equation 2.15. So, higher powers are needed for trapping small particles in conventional trapping. However, higher power intensity could cause damage to particles, specifically biological molecules, which are very sensitive to temperature. Trapping by using an aperture in metal films can overcome this problem for particles with $d < 100$ nm. Bethe obtained the transmission of light through a sub-wavelength circular hole on an infinite perfect electrical conductor PEC plane which is known as Bethe's theory and can be expressed as:

$$T = \frac{1}{2}\frac{4Z_0\pi^3}{3{\lambda_0}^4}(\frac{8r^3}{3}H_0)^2 \propto \frac{r^6}{\lambda^4} \tag{2.16}$$

where Z_0 is the free space impedance, r is the hole radius, H_0, and λ_0 are magnetic fields and wavelength of an incident plane wave, respectively. Moreover, having a particle with a refractive index of n_p inside the aperture scales the wavelength in the medium to $\lambda = \frac{\lambda_0}{n_p}$ and so an abrupt jump in transmitted light through the aperture can be observed, which is another advantage of using an aperture for trapping particles.

Using apertures on real metals with a finite thickness also has plasmonic effects that increase the transmission through the aperture [16, 17, 18, 19]. The particle inside the aperture affects the surrounding electromagnetic field in the way that transmitted light will be increased more. More importantly than the power limitation, the plasmonic trap has a small trapping volume, allowing only one protein to be trapped at a time, in contrast to conventional trapping methods [20].

As mentioned, based on Bethe's theory, when a particle with a refractive index of n_p more than the refractive index of the medium is trapped, the transmitted light will be increased. As the particle escapes from the aperture, the total photon momentum through the aperture decreases. According to Newton's third law, a force is applied to the particle to pull it back to the previous position to keep the total amount of photon momentum. This effect is called self induced back action

(SIBA) and explains how particles in the Rayleigh regime can be trapped effectively with low powers [21, 22, 23]. SIBA trapping enables the detection of the trapping simply by altering the transmission of light through the apertures due to particle movement. This is in contrast to other methods that require advanced scattering schemes [24] [25] [26] and fluorescent labeling for monitoring the particles [27].

Simulations show that the force that is calculated by the perturbative gradient force Equation 2.15 is larger than the force calculated by the rigorous Maxwell stress tensor MST analysis of Equation 2.16 [28]. Indeed, SIBA trapping in the aperture causes larger changes in the electromagnetic force than that predicted by the Rayleigh scattering field, which is not accounted for in the perturbative regime. In plasmonic based trapping, localized surface plasmons or resonances from quantum dots or atoms are needed to enhance the electric field [29, 30, 31]. However, in aperture based SIBA trapping, it is the particle that changes the electromagnetic field around it and generates robust changes in transmission. Also, for detection, high resonance quality is needed for plasmonic based trapping, but for SIBA trapping, detection can be much easier since the apertures that are used for trapping do not add any signal to the transmitted light data. Considering the effects of SIBA trapping, nanoaperture optical tweezers can be used as sensors with signal to noise ratio (SNR) of up to 33 [32]. This characteristic makes aperture SIBA trapping effective for single molecule detection and molecule interactions.

2.3.2 Nano-aperture trap stiffness

In general, the motion of the particle in the trap can be caused by two movements: Brownian motion, which is the fluctuations in trapping, and displacement from the equilibrium [33]. Trap stiffness is a method that gives us the strength of an optical trap. Stiffness can be obtained in two ways. First, by measuring the rise time from untrapped to trapped state for transmitted light from the particle in a trap. Second, with the auto-correlation of the data, which gives us the time constant. Furthermore, the time constant can be derived by obtaining the power spectral density of the noise data, fitting it to a Lorentzian function, and extracting the corner frequency, which represents the inverse of the time constant.

Single-particle nano-aperture trapping can be utilized for characterizing various parameters in nanoparticles or solutions, including diameter, concentration, and refractive index of the particles [34]. The time it takes for particles to be trapped and the duration required for a particle to become trapped after the laser is activated is directly proportional to the particle's diffusion time in the solution. Based on particle diffusion theory in a solution, the time to trap a particle exhibits a linear relationship with the nanoparticle size and a power-law dependence of -2/3 on the concentration [35, 34].

The refractive index of the particle can also be calculated according to the Clausius–Mossotti factor K given by:

$$K = \frac{\epsilon_p - \epsilon_m}{\epsilon_p + \epsilon_m} \tag{2.17}$$

K is a factor that quantifies the changes in the transmission level when the particle transitions from an untrapped state to a trapped state.

Although trapping with circular apertures can be achieved with lower laser powers compared to conventional trapping, studies have indicated that trapping using double nanoholes offers greater stability than trapping using a single circular aperture. Utilizing double nanoholes causes nanoparticles to hop between two minimum energy points on the aperture structure located at the cusps of the aperture [36].

2.3.3 Nanoaperture optical tweezer for protein studies

Typically, when studying proteins, single protein binding is employed, and the investigation focuses on the free side of the proteins. However, this approach presents some disadvantages, as one side of the protein becomes blocked, thereby restricting the protein's natural motion. This problem can be addressed by utilizing a double nanohole aperture trapping method. When a single protein is trapped between the cusps of the double nanohole aperture, it can retain its natural motion. The presence of the particle leads to a change in the refractive index of the surrounding region, resulting in an increase in light transmission.

Figure 2.4a shows a schematic of an optical tweezers setup that enables the acquisition of extraordinary acoustic Raman spectroscopy (EARs) of nanoparticles. This setup utilizes two lasers instead of a single laser for typical trapping. One laser is employed for particle trapping within the double nanohole region at the fixed wavelength, as explained earlier, as shown in scanning electron microscope (SEM) Figure 2.4b. The wavelength of the other laser is adjusted to sweep the beat frequency, which corresponds to the difference between the frequencies of the two lasers. When this beat frequency coincides with the vibrational mode frequency of the trapped particle, the vibrational mode becomes excited, resulting in a peak in the standard deviation (STD) of the noise signal as a function of the beat frequency.

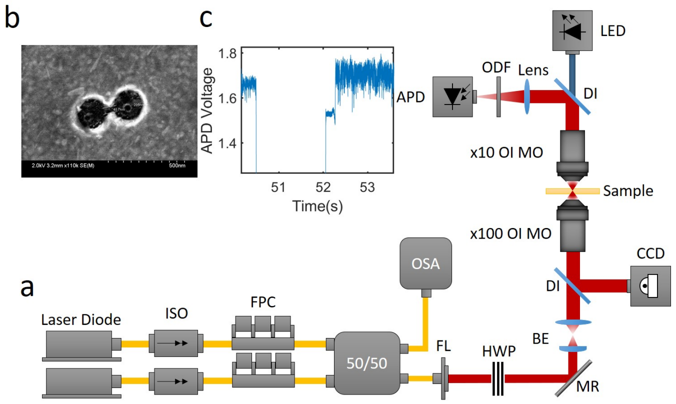

Figure 2.4: a. Schematic of dual laser optical tweezers setup: optical isolator (ISO), fiber polarization controller (FPC), optical spectrum analyzer (OSA), fiber launcher (FL), half-wave plate (HWP), mirror (MR), beam expander (BE), dichroic reflector (DI), CCD camera (CCD), microscope objective (MO), optical density filter (ODF), avalanche photodiode (APD). b. SEM image of a DNH c. Trapping event of 20 nm polystyrene Copyright ©2021, IEEE

2.3.4 PR65

PR65 is a scaffold protein subunit in the protein phosphatase 2A (PP2A) enzyme as can be seen in Figure 2.5. PR65 is highly susceptible to mutations, and these mutations can affect its mechanics and dynamics, potentially leading to pathogenic effects. Therefore, investigating the effect of mutations on the conformational dynamics of PR65 is of the highest importance.

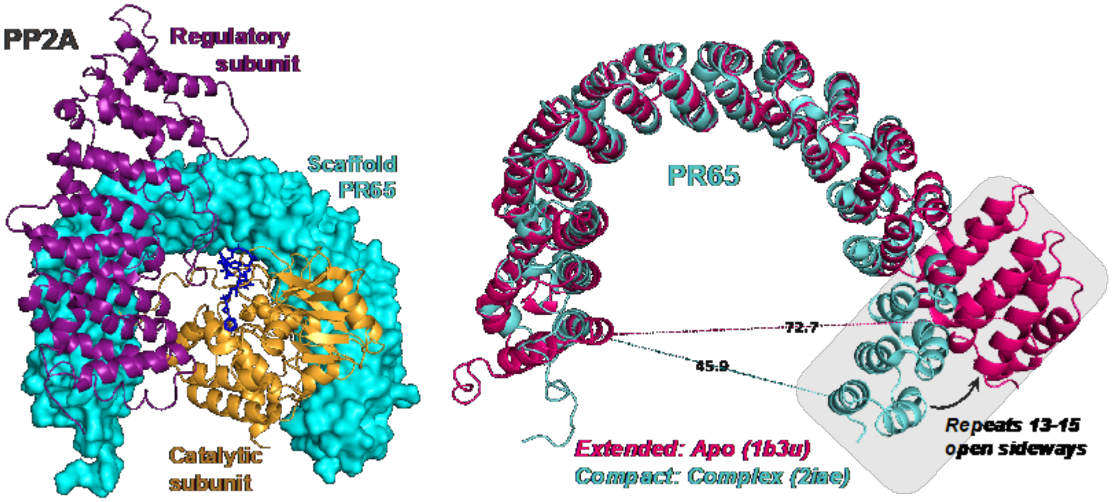

Figure 2.5: PR65 functions as a scaffolding protein subunit within the protein phosphatase 2A (PP2A) complex. [37][38] Copyright ©2007, Nature Publishing Group UK London Copyright ©1999, Elsevier

Studies on PR65 have investigated its role in PP2A enzyme regulation, its response to mechanical forces, and its interaction with other proteins. Previous studies have used molecular dynamics simulations and elastic network models to explore the dynamics and functional aspects of PR65. However, the atomic-level investigations into the effects of mutations on PR65's structure and dynamics have been limited.

The utilization of extraordinary Raman spectroscopy in an optical tweezers setup aims to offer additional insights into PR65. By employing this technique, it becomes possible to investigate the conformational changes, mechanical properties, and interaction dynamics of PR65 under controlled conditions. The EAR setup provides the ability to understand the role of PR65 in PP2A regulation and potential implications for disease development.

In summary, vibrational modes of proteins are important because they play a crucial role in their structure, function, and dynamics. Proteins are dynamic molecules that constantly undergo internal motions, and these motions are facilitated by their vibrational modes. The combination of computational simulations, experimental analysis, and extraordinary Raman spectroscopy in an optical tweezers setup provides a comprehensive approach to studying the effects of mutations on PR65 and understanding its role in enzyme regulation and disease development. To establish the credibility of the EAR spectra, it is necessary to ensure experimental reproducibility and compare the results with other theoretical and simulation studies.

2.3.5 Sample preparation

For the preparation, polystyrene beads and protein solution were used. Polystyrene beads were suspended in water and proteins were suspended in 0.01 M phosphate-buffered saline (PBS). The concentration for both of them was 0.1% w/v.

2.4 Using PVC as the substrate in fabrication with colloidal lithography

2.4.1 Surface charge effects on DNH optical trapping

With the use of double nanohole gold apertures, we have been able to trap at much lower powers than conventional optical trapping, but it is still desirable to minimize the required power as much as possible in order to trap particles that are very temperature sensitive. Thus far these double nanohole samples were prepared on glass slides and the nanoparticles were suspended in water. Due to the high dielectric constant of water at low frequencies, most surfaces become charged when immersed in water [39]. This charging of a material's surface creates an electric field that attracts counterions in solution, and the charged surface along with the layer of counterions, is commonly described as an "electrostatic double layer". A common model of the electrostatic double layer proposed by Stern can be seen in Figure 2.6. This model combines ideas of previous models by Helmholtz and Gouy-Chapman and consists of the inner Stern layer where ions are directly absorbed on the surface and immobile, and the outer Gouy diffuse layer where mobile ions are distributed according to Poission-Boltzman statistics [39]. With the electrostatic double layer there also arises electrostatic double layer forces between two charged surfaces. Simply, when the two double layers approach the concentration of free ions increases, causing an osmotic pressure that

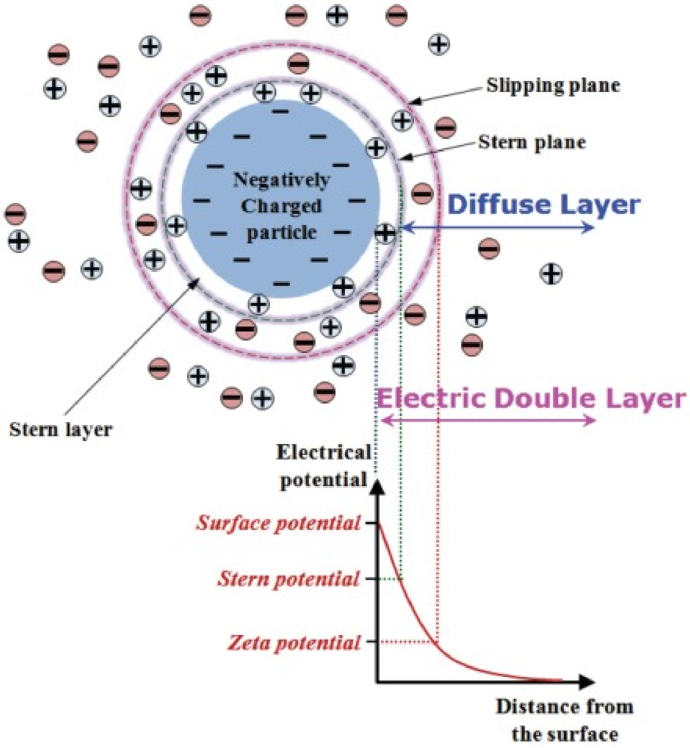

Figure 2.6: A common model of dielectric double layer [40]Copyright ©2011, Academic Press

repels the two surfaces, making the electrostatic repulsion force fundamentally different from the Coulomb force [39]. This repulsion force is true for surfaces of constant charge or constant potential that have equal signs and even unequal plates of opposite signs since is predominantly depends on the increasing concentration of ions in between the surfaces [39]. Furthermore, it can be shown that the magnitude of this force depends on the surface charge density of the two surfaces [39]. When trapping polystyrene submersed in water with a glass sample, a repulsion force is expected since glass gains a negative surface charge in water [41] and polystyrene also has a negative surface charge [42]. The repulsion forces scale exponentially with distance and are present at relatively large distances [43]. Since the electrostatic double force depends on the surface charge densities of surfaces, there are several ways that the repulsion force can be minimized. First, by adding salts to the solution the solubility of water decreases as the salt ions attract the water molecules, and in the case of glass immersed in water cause less of the silanol groups to become ionized by denoting protons to H_2O to form hydronium [41]. Therefore, due to the lower surface charge density on the surfaces, the repulsion forces are therefore minimized. This effect scales with increasing salt concentration [43].

Since the presence of surface charges is necessary for the electrostatic double layer force, by choosing a solvent in which the surfaces do not ionize the repulsive force can be minimized [39]. In the case of glass and polystyrene, a non-polar solvent can minimize the ionization of the glass surface and reduce the forces between glass and polystyrene [43].

By using a more hydrophobic substrate such as polyvinyl chloride (PVC) which is a kind of plastic to prepare the sample, the surface molecules do not ionize as easily which also decreases the surface charge density and thus the repulsion force. Quantitatively, the surface repulsion can affect the trapping forces acting on particles or molecules near the surface. It can modify the equilibrium positions, stability, and dynamics of the trapped species. Specifically, the magnitude of the surface repulsion determines the distance at which the trapping forces become significant and can counteract other attractive forces.

In some cases, the surface repulsion can lead to a repulsive barrier that prevents particles from approaching the glass surface closely since glass is a hydrophilic substrate. This barrier hinders the efficient trapping of particles.

2.4.2 Method of fabrication with PVC substrate

In this section, the process of fabricating the double nanohole apertures on PVC is explained. The effect of the incident power is compared, on the same aperture sizes, on vinyl versus glass substrates.

We used colloidal lithography to fabricate double nanohole apertures on a gold film. Microscope coverslips made of PVC, with a size of 22 mm × 22 mm, were plasma etched for 10 minutes and then sonicated in an ethanol bath for 8 minutes. $10\mu L$ solution of polystyrene spheres in ethanol, with a diameter of 300 nm and a concentration of 0.01% w/v, was evenly drop coated on the slides. This concentration is optimal to have a sufficient amount of double spheres on the surface. Using a lower concentration only produces single particles, and higher concentrations cause particle aggregation. After drying the slides through evaporation, the slides were plasma etched for 200 seconds. Plasma etching causes the nano-spheres to shrink, and by controlling the time of plasma etching, the desired size of particles can be obtained. At this point, the slides were sputtered (using the MANTIS Sputtering System) first with 5 nm Ti as an adhesion layer and then with 70 nm Au. After sputtering, the samples were sonicated in an ethanol bath for 8 minutes to remove the nanoparticles. A thickness of 70 nm of gold provides an optimal amount of gold that still allows the particles to be removed. Figure 2.7 shows how this process takes place.

Following this process and specifications, double nanoholes with a cusp size of 50 nm and a diameter of 215 nm were fabricated on thin gold film, vinyl, and glass substrates, as can be seen in Figure 2.8.

2.5 Electrophoretic and dielectrophoretic double nanohole trapping

Optical tweezers have become a highly effective method for trapping and analyzing colloidal and biological particles without causing any damage to them. However, the diffraction limit prevents the low-power trapping of objects at the nanometer scale.

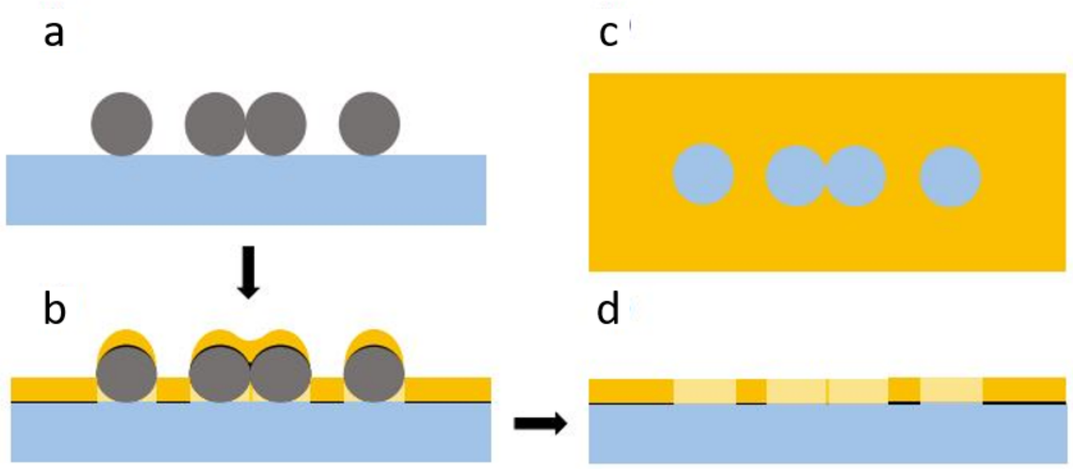

Figure 2.7: The process of fabricating double nanohole apertures on a thin gold film. a) The polystyrene solution is applied to the slides through drop-coating and then the sample is subjected to plasma etching. b) The sample is coated with titanium (Ti) and gold (Au) through sputtering. c) A top view of the sample. d) The sample is sonicated in an ethanol bath to eliminate the nanoparticles. [44] Copyright ©2019, Optics Express

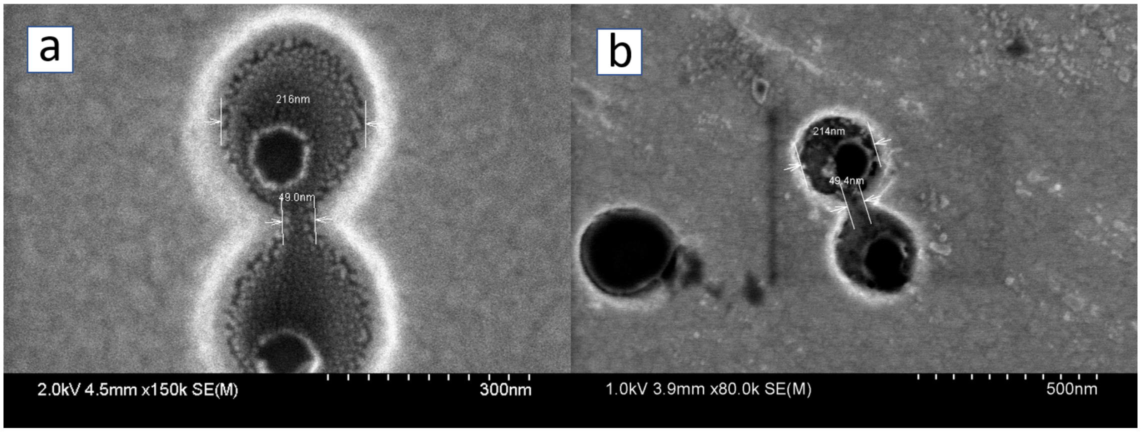

Figure 2.8: SEM image of double nanohole apertures a) on plastic substrate b) on glass substrate

Several previous studies have been conducted to facilitate trapping by employing various methods of applying an electric field to the sample, effectively surpassing the diffusion limit. To achieve this, either alternating current (AC) or direct current (DC) voltage can be utilized to generate an electric field that directs the particles toward the intended area for further examination. In one of these works, through the application of an AC electric field, along with a laser beam, a balance was achieved between electroosmotic and thermophoretic forces. This balance enabled the trapping of fluorescently labeled proteins at a distance from an array of holes [45]. Additionally, dielectrophoresis was employed using gold-coated nanopipettes to trap individual fluorescently labeled DNA, where the counter electrode was once again positioned in the solution [46]. Likewise, the integration of nanohole-enhanced dielectrophoresis, electroosmosis, and optical transmission through a periodic gold nanohole array allows for the trapping and analysis of proteins and polystyrene particles [47].

On the other hand, the utilization of plasmonic double nanohole (DNH) apertures in optical trapping has demonstrated its effectiveness in trapping particles smaller than 50 nm. This is attributed to the reduced plasmonic heating effect and the significant enhancement of the electric field within the aperture's gap region. For a typical solution with a concentration of μM to nM, the diffusion time is on the order of milliseconds, as determined by the Stokes-Einstein formula:

$$t = \frac{x^2}{6D} \tag{2.18}$$

In this equation, x represents the mean distance between the particles, D is the diffusion coefficient, and t is the diffusion time. However, other forces, such as thermophoresis force and repulsion due to surface charge, hinder the motion of particles toward the aperture, resulting in loading times ranging from several minutes to a few hours to target particles onto the plasmonic hotspots.

Taking into account the aforementioned considerations, as well as the impact of applying voltage in previous studies, researchers in another work demonstrated the rapid trapping of a 25 nm polystyrene particle by utilizing an electrothermoplasmonic flow generated by an AC field and a laser-induced temperature gradient using double nanohole in a thin gold film. They achieved the rapid transport of the particle over a distance of 63 μm and its trapping at the DNH in just 16 seconds. Again in this work a counter electrode is placed in the solution [48]. In this part of the thesis, firstly, we introduce the use of electrodes in NOTs without relying on labeling the proteins. Secondly, we are modifying the placement of the counter electrode to generate a fringe field, which significantly improves performance. In our investigation, we explore the utilization of an electrode to enhance the trapping speed of unlabeled proteins using NOTs. We achieve this by placing the counter electrode on the dielectric substrate beneath the gold film (opposite side from the solution), thus creating a fringe field in the solution through the nanohole. This modification results in a tenfold reduction in trapping time. This effect is observed for positive and negative applied voltages, including AC voltage, indicating that the speed improvement is due to dielectrophoresis. Conversely, when the counter electrode is placed in the solution (the more common approach), applying a positive voltage to the gold film relative to the counter electrode speeds up the trapping of polystyrene nanospheres. To gain a clearer understanding of the concepts presented in the mentioned works, it is necessary to delve into the mechanisms of electrophoresis and dielectrophoresis, as well as the interaction of forces. The subsequent sections will provide a more detailed explanation of these processes.

2.5.1 Electrophoresis

Electrophoresis is a technique used to separate charged particles in a solution under the influence of an electric field. It relies on the principle that charged particles will migrate in response to the electric field, with their movement determined by their size, charge, and shape. As the electric field is established, negatively charged particles (anions) move toward the positively charged electrode (anode), while positively charged particles (cations) move toward the negatively charged electrode (cathode). Their charge-to-mass ratio influences the migration of the particles, as smaller, more highly charged molecules will move more rapidly than larger or less charged particles. This allows researchers to determine the separated particles' presence, quantity, and size. Electrophoresis has numerous applications in various scientific fields, including molecular biology, genetics, forensics, and biochemistry. It is commonly used for DNA analysis, protein characterization, and the study of molecular interactions. In electrophoresis, several forces come into play to determine the movement and behavior of charged particles. These forces include the electric force, electrostatic force, friction force, and electrophoretic retardation force. The interaction of forces is shown in Figure 2.9(a). The electric force is the primary driving force in electrophoresis. It arises from the applied electric field and acts on charged particles, causing them to migrate toward the electrode of the opposite charge. The electric force is proportional to the charge of the particle and the strength of the electric field. The electrostatic force arises from the interaction between charged particles. When multiple charged particles are present in a system, they can exert attractive or repulsive forces on each other based on their charges. The electrostatic force influences the movement and distribution of charged particles during electrophoresis. The friction force, also known as the drag force, is a resistive force experienced by charged particles as they move through a medium. It opposes the motion of the particles and depends on factors such as the particle size, shape, and velocity. The friction force tends to slow down the movement of particles during electrophoresis. Following equation shows the drag force:

$$F_d = \frac{1}{2}\rho v^2 C_d A \tag{2.19}$$

F_d is the drag force, ρ is the density of the fluid, ν is the velocity of the object relative to the fluid, C_d is the drag coefficient, which depends on the shape and properties of the object, and A is the reference area, typically the cross-sectional area of the object perpendicular to the flow direction.

The electrophoretic retardation force is a resistive force that counteracts the electric force. It arises due to the motion of charged particles through a medium with finite conductivity. As particles move, they create a localized region of charge imbalance, leading to a potential difference. This potential difference generates an opposing force that acts against the electric force and slows down the particles. These forces interact with each other to determine the behavior of charged particles during electrophoresis. The electric force drives particles towards the electrode of opposite charge, while the electrostatic force influences particle-particle interactions. The friction force opposes particle motion, and the electrophoretic retardation force acts as a resistive force against the electric force. The interplay of these forces determines the speed, direction, and separation of charged particles during electrophoresis experiments.

2.5.2 Dielectrophoresis

Dielectrophoresis (DEP) is a phenomenon where neutral particles are induced to move in a non-uniform electric field due to their inherent polarizability. It occurs when a non-uniform electric field is applied to a medium with particles, such as a suspension or fluid. In dielectrophoresis, the movement of particles is influenced by the interaction between the electric field and the polarizability of the particles. When a polarizable particle is subjected to a non-uniform electric field, dielectrophoresis occurs. The electric field causes the particle to become polarized, causing the poles to experience an electric force along the field lines. This force can be either attractive or repulsive, depending on the orientation of the dipole. Since the field is non-uniform, the pole experiencing the strongest electric field dominates over the other pole, resulting in particle movement. Importantly, the direction of the force depends on the field gradient rather than the field direction, enabling DEP (Dielectrophoresis) to occur in both AC and DC conditions. The direction of particle movement in dielectrophoresis depends on the relative dielectric properties of the particles and the surrounding medium. The movement can be classified into two types: positive DEP and negative DEP.

Positive DEP

In positive DEP, the particles have a lower dielectric constant than the surrounding medium. When an electric field is applied, the particles experience an attractive force toward high electric field intensity regions. This occurs because the particles tend to align themselves with the electric field lines, leading to a net movement toward the high-field regions.

Negative DEP

In negative DEP, the particles have a higher dielectric constant than the surrounding medium. In this case, the particles experience a repulsive force away from the high-field regions. They tend to align themselves against the electric field lines, resulting in a net movement away from the high-field regions. The direction and magnitude of particle movement in dielectrophoresis depend on various factors, including the electric field strength, frequency, and the physical properties of the particles and the surrounding medium. By manipulating these factors, researchers can control and direct the movement of particles in dielectrophoresis experiments. Dielectrophoresis has several applications, such as particle sorting, cell manipulation, and microfluidic device-based assays. It offers a versatile tool for the precise manipulation and positioning of particles and cells in lab-on-a-chip systems and biological research. Figure 2.9(b) demonstrates how the presence of an electric field gradient can influence a polarized particle.

For a spherical particle of radius a, the dielectrophoresis force is:

$$F_{\text{DEP}} = 2\pi a^3 \varepsilon_L \text{Re}\left(\frac{\varepsilon_P^* - \varepsilon_L^*}{\varepsilon_P^* + 2\varepsilon_L^*}\right) \nabla E^2 \tag{2.20}$$

in which E shows the electric field, ε_P^* and ε_L^* are the complex permittivities of the particles and the liquid, respectively. As can be seen in Equation 2.20, F_{DEP} and F_{grad} from Equation 2.15 are both originated from the gradient of the electric field.

2.6 Conclusion

In summary, this chapter serves as an exposition of key theoretical foundations underpinning this thesis's research. It provides a comprehensive overview of the the-

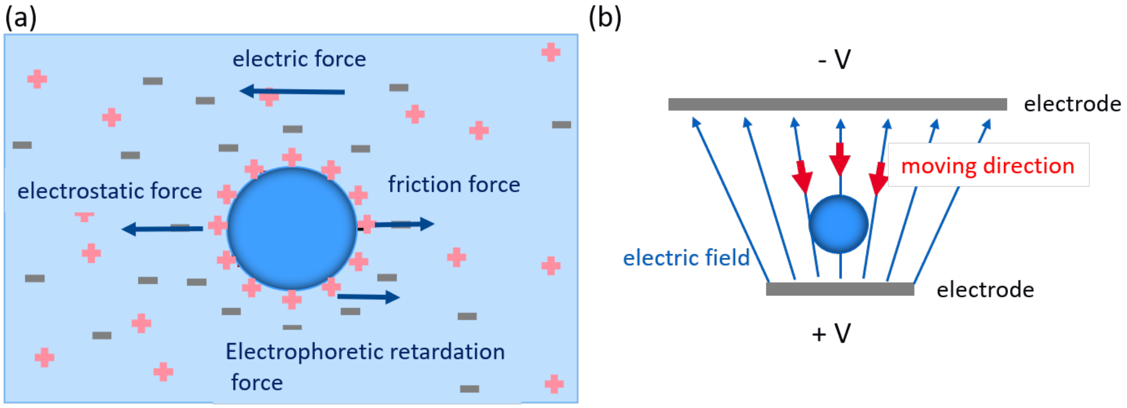

Figure 2.9: (a) Interaction of forces in electrophoresis technique (b) Interaction of forces on a polarized particle located in a non-uniform electric field (Dielectrophoresis technique)

ory behind surface plasmon resonance sensors, optical tweezers, and surface charge repulsion, which form the fundamental basis for the investigations carried out. Furthermore, the chapter includes a detailed explanation of the fabrication process for double nanoholes using colloidal lithography. By presenting these essential concepts and methodologies, this chapter establishes a solid foundation for the subsequent work conducted in the thesis.

Chapter 3

Contributions

This chapter highlights the author's contributions through three published papers. The subsequent section presents an overview of each paper. The complete manuscripts are included as appendices in the dissertation. In the first subsection, the discussion revolves around enhancing the sensitivity of SPR sensors by utilizing SRSP. The subsequent part delves into the investigation of employing PVC substrate instead of the glass substrate in colloidal lithography to fabricate DNHs on a thin gold film. Lastly, the final section explores using voltage to speed up trapping in NOTs.

3.1 Improving the sensitivity of existing surface plasmon resonance systems with grating-coupled short-range surface plasmons

SPR sensors, based on the excitation of surface plasmon polaritons (SPPs) on a metal surface, are widely used for detecting biomolecule interactions.

By incorporating localized resonances from periodically arranged short-range modes in a similar configuration to traditional SPR sensors, the sensitivity of the surface can be increased three-fold. Optimal design parameters, such as the period and gap length of the grating, are determined through RCWA, with finite difference time domain (FDTD) simulations confirming the correspondence of the short-range modes to localized surface plasmon resonances. This approach significantly enhances sensitivity and resolution for monitoring biomolecule interactions using SPR sensors.

This work is significant as it improves the performance of existing SPR systems without requiring substantial modifications. With the widespread use and commercialization of SPR sensors in laboratories worldwide, leveraging the existing platform while enhancing sensitivity has profound implications for biomedical research, diagnostics, and drug development. Integrating grating-coupled short-range surface plasmons enables more precise detection and analysis of biomolecular interactions, enhancing accuracy in research and diagnostics.

This improvement is achieved by utilizing the concept of short-range surface plasmon (SRSP) modes, which exhibit tighter confinement to the surface as the metal film thickness decreases. Light is coupled into these SRSP modes using a periodic structure with localized surface plasmon (LSP) resonances, demonstrating enhanced surface sensitivity compared to conventional SPR sensors. Importantly, this proposed approach maintains compatibility with existing commercial SPR systems using prism coupling, facilitating its adoption in various research and diagnostic settings.

In summary, this work presents a novel approach to enhance the sensitivity of existing SPR systems by incorporating grating-coupled short-range surface plasmons. The proposed method offers three times higher surface sensitivity and four-fold improved resolution compared to traditional SPR sensors. These findings have significant implications for biosensing, enabling more accurate and precise detection of biomolecular interactions. Moreover, this approach can be readily implemented in commercial SPR platforms without major modifications.

3.2 Accessible high-performance double nanohole tweezers

This work consists of three different projects aimed at improving the existing colloidal lithography method for fabricating double nanoholes (DNHs) and consequently enhancing optical trapping efficiency. Colloidal lithography is a fabrication method utilized to create nanoapertures on a glass substrate with a gold film sputtered on it. By adjusting the size of polystyrene nanospheres and the etching time, precise control over the size and configuration of the nanoapertures can be achieved.

The first project focuses on detecting and characterizing nanoapertures without relying on scanning electron microscopy (SEM). Combining camera CCD images with the polarization-dependent transmission of a laser beam makes it possible to identify and differentiate between various nanoaperture structures. The brightness and polarization response of the transmitted light exhibit variations across different structures, facilitating rapid identification of DNH apertures.

The second project explores the use of a polyvinyl chloride (PVC) substrate, which is a kind of plastic, instead of glass to enhance trapping efficiency in the current colloidal lithography method. Trapping experiments conducted with 20 nm polystyrene nanospheres demonstrate that employing a plastic substrate leads to a stiffer trap, enabling the use of lower laser powers and reducing heating effects. The plastic substrate also exhibits reduced noise levels during trapping, indicating improved stability. The transition from glass to plastic substrate reduces the minimum laser power required by a factor of 7. Using the apertures that were shown in figure 2.8 and the same incident laser power of 5.4 mW for both of them, 20 nm polystyrene in water (0.03% v/w) was trapped. Figure 3.1 shows the jumps in transmission signal from the untrapped to the trapped state. On average ($N > 5$), a jump of 5% for glass and 10% for vinyl was observed after unblocking the laser.

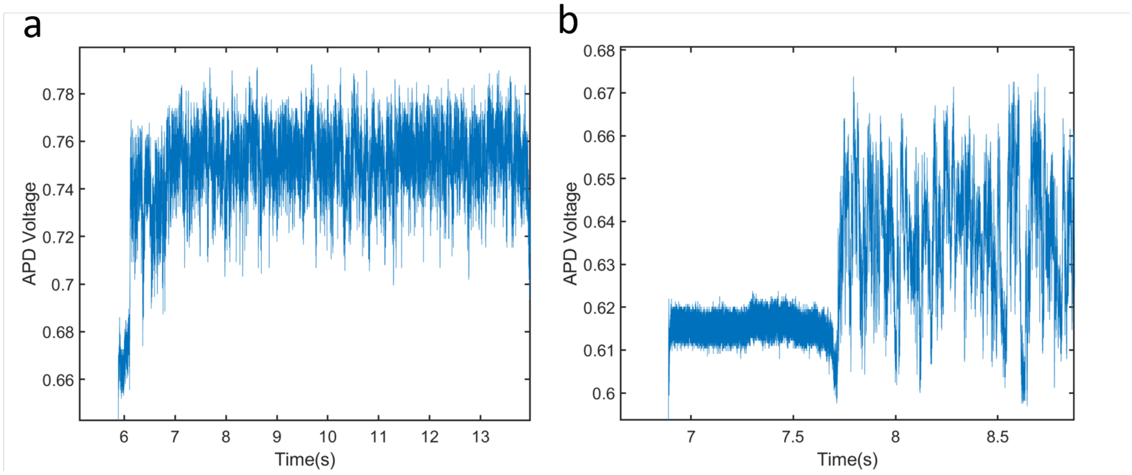

Figure 3.1: Trapping 20 nm polystyrene nanosphere at the same laser power and on the same aperture size on a) vinyl substrate b) glass substrate

According to our experiments, less laser power is needed on vinyl substrates compared to glass, both for trapping initiation and keeping particles in the trap. Incident power was measured when trapping of 20 nm polystyrene was stable, using the same aperture sizes on vinyl and glass substrates. On average ($N > 6$), the initial laser power was 5.76 mW for the glass substrate and 1.38 mW for the vinyl substrate. Also, the minimum average power ($N > 9$) for keeping the particles in the trap was measured and which was 0.63 mW for vinyl and 4.7 mW for glass substrates. Figure 3.2 shows the minimum laser power needed for keeping particles in the trap on the glass substrate in comparison to vinyl.

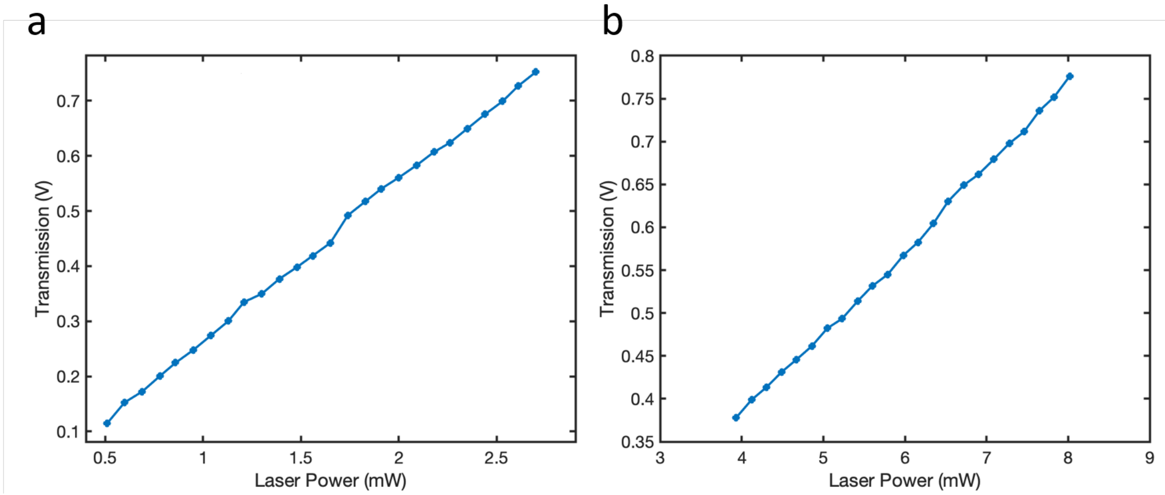

Figure 3.2: Comparing minimum power needed for keeping particle in the trap for a) vinyl sample b) glass sample

In the third project, a novel method is developed for removing polystyrene nanospheres without relying on sonication in ethanol, as commonly employed in colloidal lithography. Instead, Scotch tape is utilized to exfoliate the nanoparticles from the surface, followed by washing in ethanol. This tape exfoliation method ensures a more uniform removal of spheres compared to sonication, resulting in high-quality apertures without surface damage.

Overall, these projects contribute to improving the fabrication process of DNHs. The ability to detect and characterize nanoapertures using CCD images and polarization-dependent transmission simplifies the characterization process. Using a plastic substrate improves trapping efficiency and stability. Also, it enables low-power trapping, which is particularly crucial for biological materials. Introducing the tape exfoliation method provides a viable alternative to sonication for removing nanospheres, yielding high-quality apertures without surface damage. These advancements have significant implications for various applications involving DNHs, such as sensing, imaging, and trapping of biological materials.

3.3 Fringe dielectrophoresis nanoaperture optical trapping with an order of magnitude speed-up for unmodified proteins

Single-molecule techniques play a crucial role in understanding the behavior and dynamics of biomolecules [49]. Analyzing proteins in their unmodified state is essential to avoid disrupting their natural function and causing significant changes in their properties like diffusion, surface potential, and binding kinetics [50]. Various single-molecule techniques, including nanopores, iScat, and NOTs, enable the study of unmodified proteins in water-based environments. NEOtrap, a nanopore technique, allows the trapping of proteins as small as 14 kDa [51]. iScat has achieved a detection limit of 40 kDa [52], which can be further improved to below 9 kDa using advanced machine learning [53]. NOTs have successfully trapped single particles as small as 6.5 kDa [52] [35]. NOTs face a diffusion limitation wherein particles must disperse and reach areas with a high-intensity electric field within a distance of a few tens of nanometers from apertures in order for them to be effectively trapped [54]. To overcome this, previous studies have utilized voltage to surpass the diffusion limit. For example, a study achieved trapping of fluorescently labeled proteins by carefully balancing electroosmotic and thermophoretic forces using an alternating current (AC) electric field and a laser beam [45]. Another approach involved using gold-coated nanopipettes and dielectrophoresis to trap individual fluorescently labeled DNA, with the counter electrode placed in the solution [46]. Furthermore, integrating nanohole-enhanced dielectrophoresis, electroosmosis, and optical transmission through a periodic gold nanohole array allowed trapping and analysis of proteins and polystyrene particles [45]. On the other hand, plasmonic double nanohole (DNH) apertures have demonstrated effectiveness in trapping particles smaller than 50 nm by reducing plasmonic heating and enhancing the electric field within the aperture's gap region. Considering the factors mentioned above, including the influence of voltage application observed in earlier research, another study showed the fast trapping of a 25 nm polystyrene particle. The researchers achieved this by employing an electrothermoplasmonic flow produced through an alternating current (AC) field and a laser-induced temperature gradient, utilizing a double nanohole (DNH) structure within a thin gold film. They successfully transported the particle over a distance of 63 μm and trapped it at the DNH in a mere 16 seconds. Again, in this experiment, a counter electrode was positioned in the solution [48]. In this thesis, two significant modifications are introduced. Firstly, an approach for employing electrodes in NOTs without the need for protein labeling is proposed. Secondly, the positioning of the counter electrode is adjusted to generate a fringe field, resulting in a significant enhancement of trapping performance. This investigation focuses on utilizing electrodes to improve the speed of trapping unlabeled proteins using NOTs. To achieve this, the counter electrode is placed on the dielectric substrate beneath the gold film, on the opposite side of the solution. This positioning creates a fringe field within the solution through the nanohole. As a result of this modification, the trapping time is reduced by a factor of ten, with both negative and positive potentials demonstrating a dielectrophoretic effect. The applied DC voltage proves to be the most effective in this approach. Importantly, this method successfully traps neuro peptide Y, with a low molecular weight of only 4 kDa. Conversely, placing the counter electrode in the solution generally does not accelerate protein trapping. However, it does lead to voltage-dependent faster trapping of polystyrene spheres as the applied voltage increases, likely due to changes in the repulsive surface potential.

Chapter 4

Additional research contributions

This chapter focuses on two works that have been submitted to conferences but have not yet been published in journals. These works explore the identification of vibrational modes of particles through the utilization of Extraordinary Acoustic Raman Spectroscopy EARs. The first part of the chapter discusses the investigation of vibrational modes in PR65. The second work examines the effect of laser power on the spectrum quality obtained in the EAR technique, emphasizing the importance of using optimum power to achieve optimum results.

4.1 Extraordinary acoustic Raman spectroscopy of PR65 [55]

Using a DNH optical tweezer setup and applying two lasers, we trapped and excited acoustic vibration modes of the PP2A heterotrimeric complex composed of PR65. Our experiment shows that the vibrational modes are at frequencies of 9.29 GHz, 19.28 GHz, 30.23 GHz, and 41.18 GHz, which matches the normal mode analysis results. This technique is single molecule and label free compared to typical methods of characterization of biomolecules. Characterizing PR65 can be used as a paradigm for understanding the structural regulation of many repeat proteins.

4.1.1 Introduction

Conventional optical trapping has been successful at trapping a wide range of molecules such as dielectric particles, nano-wires, and crystal nanorods [56, 57, 58, 59]. But, with conventional (gradient force) optical tweezers there are limitations on which particles can be trapped [36]. Conventional traps often require high powers and/or the use of tethering to trap biological molecules [60], [61], and other small molecules which can disturb the particles' natural state and are not always practical [62]. To trap small particles with low powers, apertures that localized the electric field intensity was introduced. These nanoplasmonic apertures utilize the fact that the presence of a particle in the aperture results in much larger transmission, which creates larger restoring forces that contribute to trapping [63]. Trapping with a double nanohole (DNH) aperture has shown to be much more efficient than conventional optical traps, allowing for the trapping of small nanoparticles and single proteins at low powers [36, 44]. With the use of DNH optical trapping, the characteristics of small molecules, such as protein-protein interactions and protein-DNA interactions can be determined[62].

Raman spectroscopy has been used to identify the acoustic vibrational modes of numerous molecules but still has limited use for biological molecules in the nanometer range, due to its low spectral resolution [64]. Conventional Raman spectroscopy requires that any elastic scattering from the excitation source is filtered out resulting in a low frequency limit of 10 cm^{-1} [65]. However, molecules such as proteins and DNA have acoustic modes on the scale of 100 GHz [66]. To excite the Raman modes of proteins we use extraordinary acoustic Raman spectroscopy (EAR) [66], where two lasers are mixed at slightly different wavelengths producing a beat frequency. The beating laser acts on the particle as an electrostriction force, causing mechanical deformations of the particle that result in fluctuations in the scattered light. These fluctuations in scattered light are directly measured by an avalanche photodiode (APD). As the beat frequency is tuned to the resonant frequency of the particle, the particle oscillates resonantly.

In this paper, we demonstrate that DNH apertures can be used to trap the protein phosphatase subunit PR65 without the use of tethering or dyes. Previously, we demonstrated the use of EAR to identify the characteristic acoustic frequency modes of polystyrene [66], and in this work, we extend the use of EAR to the enzyme protein phosphatase 2A (PP2A) subunit, PR65. Protein phosphatase 2A regulates many activities in the body including DNA replication, transcription, and the cell cycle, and is dysregulated in many diseases [37]. PR65 is an allosteric regulator within PP2A, and by identifying its acoustic Raman modes, we can better understand the conformational changes and binding that contribute to biological signaling.

4.1.2 Experimental setup

Figure 2.4.a shows the optical tweezers setup, which can be used for trapping nanoparticles, proteins, viruses, etc. To trap a single nanoparticle, a DNH aperture in a gold film was used in order to localize the laser field applied to the particle. The DNH can be seen in Figure 2.4.b. As shown in Figure 2.4.c, when the particle is trapped in a DNH, the level of the signal is changed in the avalanche photodiode (APD). This step, which shows an increase in transmitted light through the aperture, is because of the change in the refractive index of the area after the particle is trapped. While trapping polystyrene beads, a 10-20% jump in transmitted light is normal. However, the jump is only 2-7% for proteins because of the smaller size and polarizability. Fluctuations are also increased after trapping due to the higher motion of particles in the trap.

EAR

The main difference of the EAR trapping setup is the use of two lasers instead of one. One of the laser frequencies is kept constant and the frequency of the other laser can be controlled by controlling the temperature in the laser controller. The two frequencies mix to create the beat frequency, which modulates the electrostriction force on the particle. By changing the frequency of one laser, the beat frequency can be tuned from 1 GHz to 0.3 THz. Using modulation of two lasers, the particle is thermally excited with incoherent low frequency light instead of the high frequency coherent light used for other techniques [33]. When the beat frequency matches the vibrational modes of the particle, the vibration in the particle increases. Higher vibrational motions cause more fluctuations in the transmitted light to the APD. Therefore, the standard deviation (STD) of the signal for the resonant beat frequencies shows more intensity. With this technique, we can get the resonances of particles without any energy relaxation, which is typical in conventional Raman spectroscopy. We also avoid losing data caused by viscous damping since our data comes from the heating of the particles at the resonance frequency [66].

4.1.3 Experimental results and discussion

In this work, the EARs of 20 nm, 30 nm polystyrene beads, and PR65 are presented and the resonance peaks are compared with calculated values and simulation results.

EARs of polystyrene nanospheres

Figure 4.1 shows the EAR spectrum of polystyrene nanoparticles with diameters of 20 ± 2 nm and 30 ± 3 nm. It shows the STD of the data from transmitted light through the aperture vs the beat frequency which is the difference of the frequencies of the two lasers. For 20 nm polystyrene beads, the peak frequencies are predicted by Lamb's theory to be at 44 GHz [67] and 68 GHz which are related to quadrupolar accordion mode (n=0, l=2) and spherical breathing mode (n=0, l=0), respectively. The physical mechanism of electrostriction is related to the inversion-symmetry modes ($l = 0$ and $l = 2$) and the Brownian motion of the particle is related to heating. For 30 nm nanospheres, the peaks are predicted to be at 29 GHz and 45 GHz [68, 69, 70]. In Figure 4.1 predicted peak values are shown with dashed lines. For the 20 nm nanoparticle, the measured peaks are at 47.85 GHz and 68.72 GHz, and for the 30 nm nanoparticle, the peaks are at 29.44 GHz and 45.21 GHz. Considering the error within the optical spectrum analyzer (3 GHz) and the size variation of particles, these experimental values are in agreement with the calculated values.

These data are reproducible. Figure 4.2 shows the confirmation of the position of l=2 peaks for 20 nm and 30 nm polystyrene.

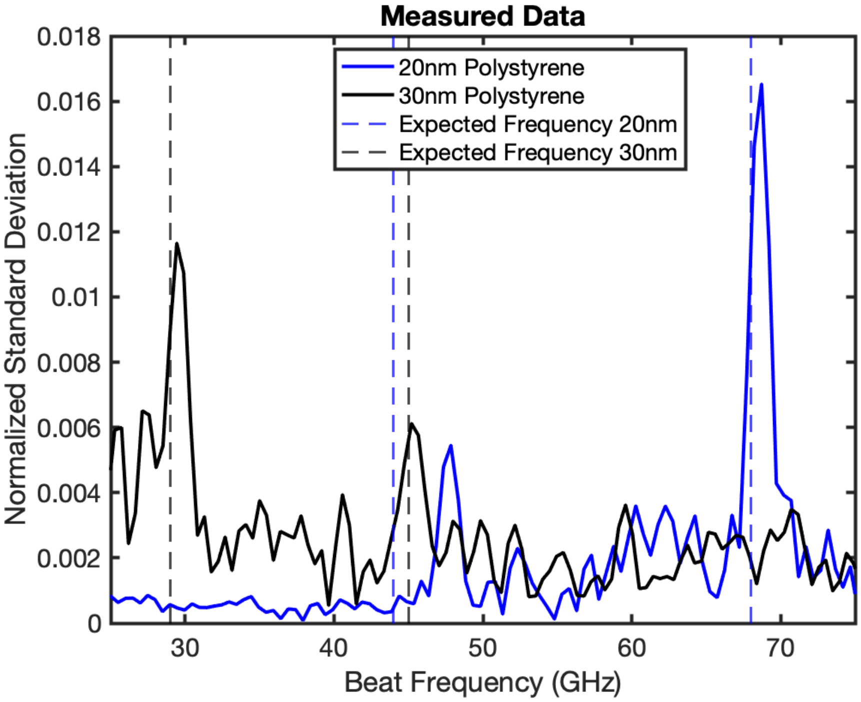

Figure 4.1: EAR spectrum of polystyrene with the diameters of 20 nm and 30 nm

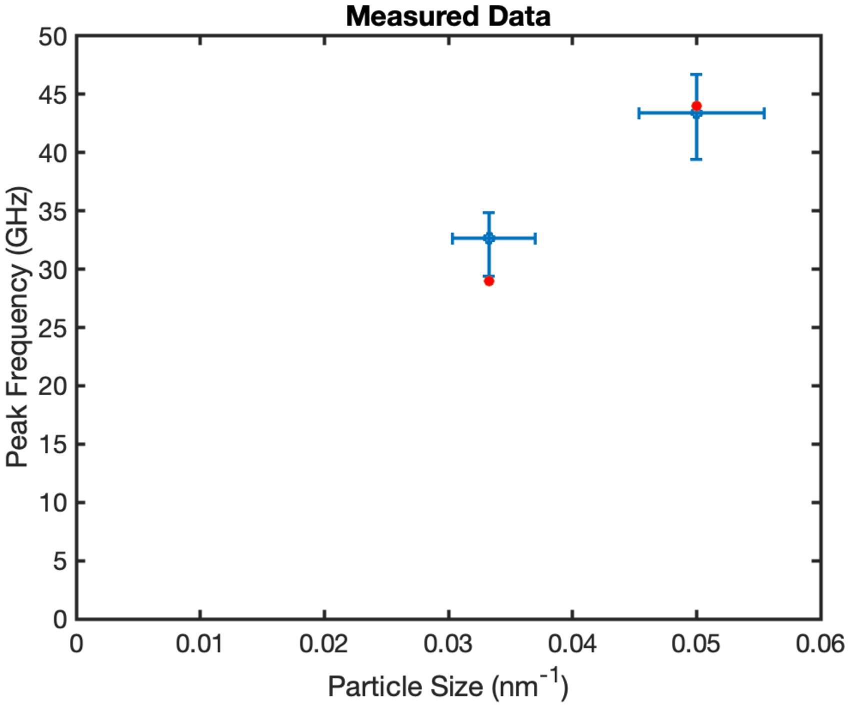

Figure 4.2: Measured l=2 peaks of 20 nm and 30 nm polystyrene spheres compared with their predicted values for multiple runs Copyright ©2021 IEEE

EARs of PR65

Figure 4.3 shows one trapping event of a PP2A heterotrimeric complex composed of PR65 using just one laser after blocking the laser and unblocking again. A higher noise level is obvious after the particle has been trapped. After trapping the protein, the second laser is introduced to get the EAR spectra [71]. Figure 4.4 shows the EAR spectra of the PP2A heterotrimeric complex composed of PR65. The dashed lines are the result of Normal Mode Analysis (NMA) for the compact PR65 scaffold. The frequencies related to modes 2-5 are reported as 11.06 GHz, 20.79 GHz, 31.54 GHz, 37.95. As it can be seen in Figure 4.4, the peaks in our measurements are at 9.29 GHz, 19.28 GHz, 30.23 GHz, and 41.18 GHz. The experimental values match well with the NMA considering that there is frequency variation for each of the NMA results.

4.1.4 Conclusion

In this paper, we have shown that the vibration modes of PR65 can be excited and detected using the EAR setup. This characterization can be obtained with single molecule excitation and in a spectrum range of 0.1-10 cm^{-1} with 0.1cm^{-1} resolution which has not been accessible with other techniques. Characterizing PR65 paves the way to understanding the structural regulation of many repeat proteins.

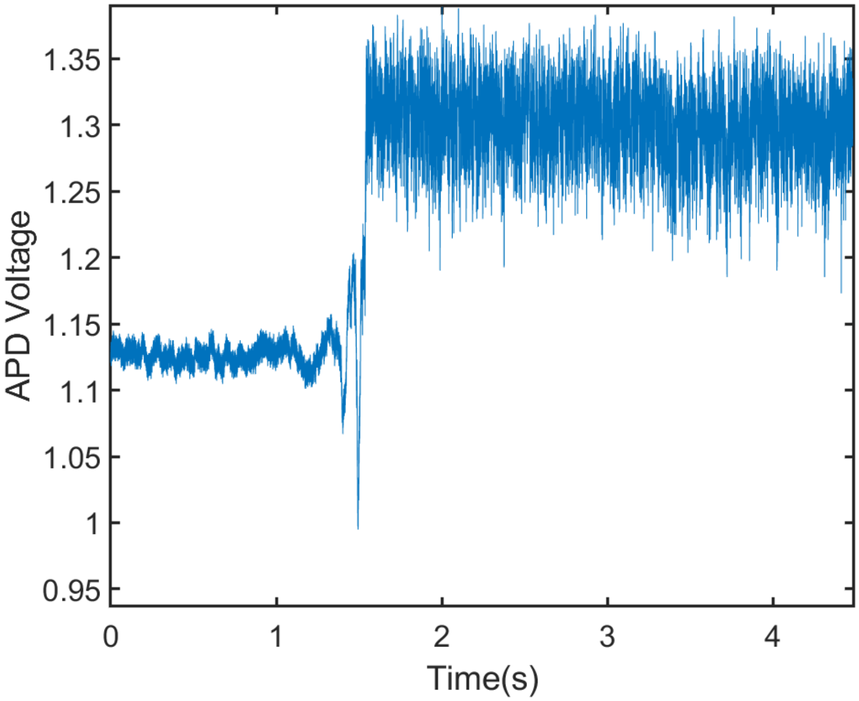

Figure 4.3: Trapping event of a PP2A heterotrimeric complex composed of PR65 using optical trapping setup Copyright ©2021 IEEE

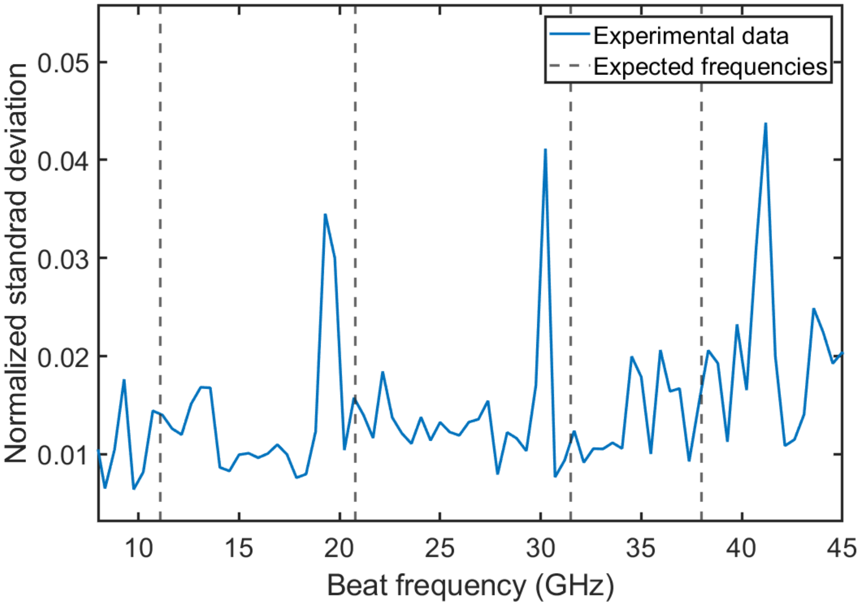

Figure 4.4: Acoustic Raman spectra of PR65. Solid lines are the experimental measurements and the dashed lines show the NMA results Copyright ©2021 IEEE

4.2 Probing optimum applied power for extraordinary acoustic Raman spectroscopy [72]

We applied a two laser extraordinary Raman spectroscopy technique in a double nanohole optical tweezers setup to excite and detect the vibrational modes of 20 nm polystyrene beads. We measured the quadrupolar accordion mode frequency to be 47.85 GHz and the spherical breathing mode frequency to be 68.72 GHz which are very close to their predicted values. According to our measurements, there is an optimum power to excite the vibrational modes and to get sharp peaks in the beat frequency spectrum, simultaneously. Improving the resolution of our present Raman spectroscopy system provides a way to more accurately detect changes in resonance frequency, characterize DNA unzipping, and protein-DNA interactions, and classify mutant proteins.

4.2.1 Introduction

Since the first demonstration of single beam gradient force optical trapping [73], optical traps have been used widely in biological science as well as material science. While conventional gradient force optical traps have been successful in trapping dielectric particles [74], metallic particles [75], and even some larger viruses and bacteria [76], the use of conventional optical tweezers for particles and biomolecules in the nanometer range has been limited. With a conventional optical trap, the power required for trapping scales with the inverse third of the particle size [77], meaning high powers are required to trap small particles, which can disturb a particle's natural conformation, especially those of temperature sensitive biomolecules [78, 79]. To overcome the limitations of conventional optical traps, nanoplasmonic apertures were used to enhance and localize the electric field acting on the particle. These nanoapertures created a self-induced back action effect, where the particle within the aperture increased the transmission through the aperture, in turn increasing the optical restoring forces. Double nanohole (DNH) apertures have shown to be quite effective, trapping particles in the 10 nm scale as well as single proteins and DNA hairpins at low powers [80, 81]. Optical trapping with DNH apertures has shown large potential for studying the characteristics of biomolecules such as DNA unzipping, protein-DNA interactions, and classifying mutant proteins [81].

Conventional Raman spectroscopy has long been able to identify molecules by their characteristic frequency modes, but it has certain limitations. Conventional Raman has low spectral resolution and elastic scattering from the laser source must be filtered out, restricting the lowest frequency to 10 cm^{-1} [82]. With these limitations, using Raman spectroscopy to characterize nanoparticles and many proteins, that have frequency modes in the range of 0.7-10 cm^{-1} [83], has been unfeasible. To characterize nanoparticles with Raman spectroscopy we use extraordinary acoustic Raman spectroscopy (EAR), a technique previously described by our group that uses two lasers to excite the particle [82]. The two lasers are mixed at a slightly different wavelength, creating a beat frequency that modulates an electrostriction force in the particle that causes vibrations in the particle. The beat frequency can then be temperature tuned to the resonant frequency, causing the particle to oscillate resonantly.

In this work, we look at probing the optimum power for EAR measurements. Previously, our group identified the characteristic resonant frequencies of polystyrene particles as well as some proteins [82], but now we look at the effect of power on the EAR spectrum. We show that the clarity of the EAR response is dependent on the incident laser power of which the particle is excited. We also show that if the incident laser power is beneath a certain level, the resonant vibrations can not be excited.

4.2.2 Experimental results

In this paper we present the EAR for 20 nm polystyrene, showing the measured resonant frequencies and comparing them to the calculated frequencies. We then look at the effects of power on the EAR signal, to determine the optimum probing power for EAR measurements.

EAR of polystyrene nanoparticles

Fig. 4.6 shows the EAR of a 20±2 nm diameter polystyrene sphere. The measured resonant frequencies can be determined by finding at what beat frequencies there

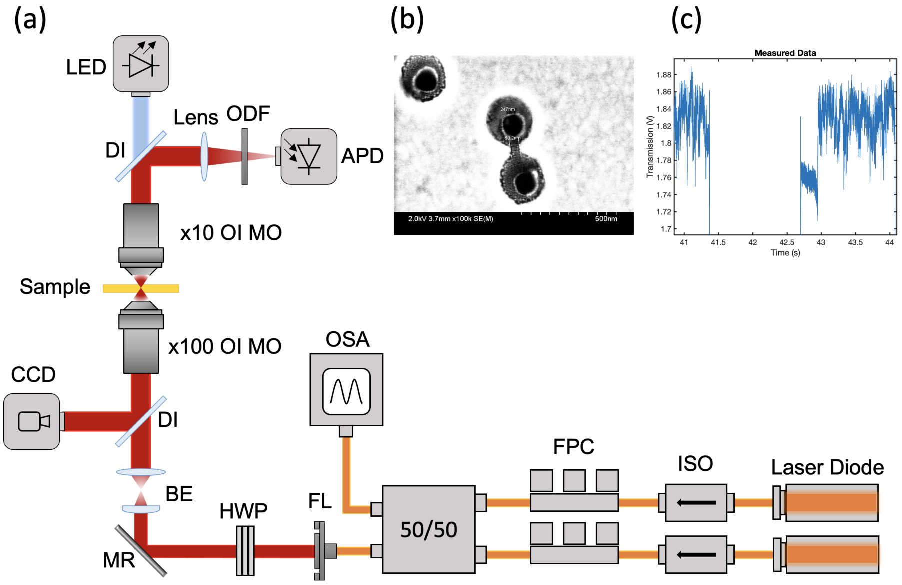

Figure 4.5: Experimental setup (a) schematic of two-laser EAR trapping setup: avalanche photodiode (APD), optical density filter (ODF), dichroic reflector (DI), oil immersion microscope objective (OI MO), CCD camera (CCD), beam expander (BE), half-wave plate (HWP), mirror (MR), fiber launcher (FL), optical spectrum analyzer (OSA), fiber polarization controller (FPC), optical isolator (ISO) (b) SEM image of a DNH in a gold film (c) trapping event of a 20 nm polystyrene sphere. Copyright ©2021 SPIE

are peaks in the normalized standard deviation (NSTD). The expected resonant beat frequencies are calculated using Lamb's theory and were found to be 44 GHz and 68 GHz for 20 nm polystyrene nanospheres [67]. These frequencies correspond to the quadrupolar accordion mode (n = 0, l = 2) and the spherical breathing mode (n = 0, l = 0), for 44 GHz and 68 GHz respectively. Here, we measured the quadrupolar accordion mode frequency to be 47.85 GHz and the spherical breathing mode frequency to be 68.72 GHz. The measured values are comparable with the expected values, considering a slight variation in polystyrene particle size and the ±3 GHz error in the beat frequency from the optical spectrum analyzer.

Effect of incident laser power on EARs

The quality of the EAR measurements can be affected by the power of the excitation laser source. As seen in Fig. 4.6, when the power is 9.06 mW after the objective lens, the peaks within the EAR are very distinctive and sharp. This allows us to easily determine the resonant frequencies of the particle. However, when the incident laser power is too high, we see a much broader peak, seen in Fig. 4.7 in which the laser power is 11.04 mW. It seems that at higher powers, the particle continues to oscillate resonantly after it is excited even for non-resonant beat frequencies, and slowly returns to its non-resonant state. Although the frequencies of the acoustic mode at these high powers can be inferred from the step in the STD, the exact frequency becomes ambiguous due to the maintained high STD level. Contrarily, if the incident power is too low the resonant mode can fail to become excited altogether. Fig. 4.8 shows the EAR spectrum of 20 nm polystyrene when the incident power is 5.44 mW. With a power that is too low neither of the acoustic modes can clearly be identified, there are no distinct peaks around 44 or 68 GHz, and the EAR spectrum resembles random noise. These results demonstrate that there is an optimum power range at which to excite the particles for EAR measurements, but further research is needed to limit the range and determine how particle size affects the optimum power range.

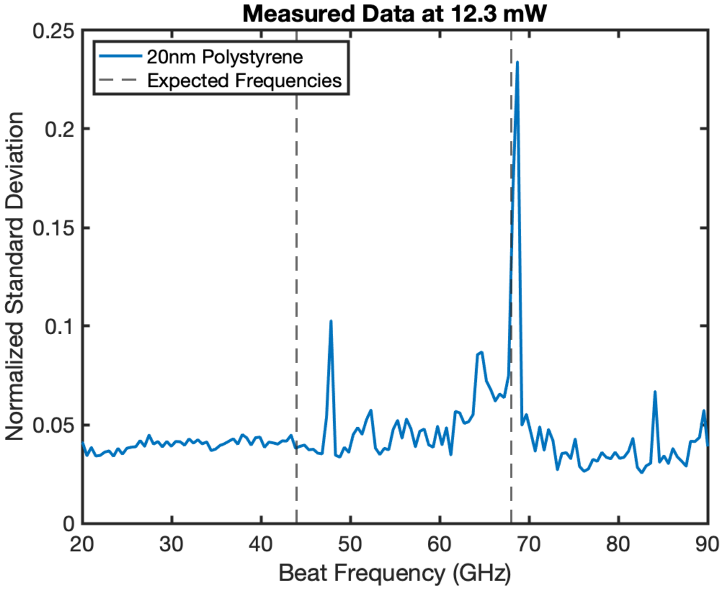

Figure 4.6: EAR spectrum of 20 nm polystyrene at 12.3 mW before the objective lens. Copyright ©2021 SPIE

4.2.3 Conclusion

In this work, we have shown excitation and detection of l = 0 and l = 2 vibration modes for 20 nm polystyrene. Comparing with predicted values, it can be seen that beat frequency peaks can be detected with a resolution of 0.1 cm^{-1} which has not been accessible with other Raman techniques. Here we also probed the effect of incident laser power on EAR measurements. An optimum range of power is needed in order to get sharp peaks in the EARs results and to be able to excite the vibrational modes

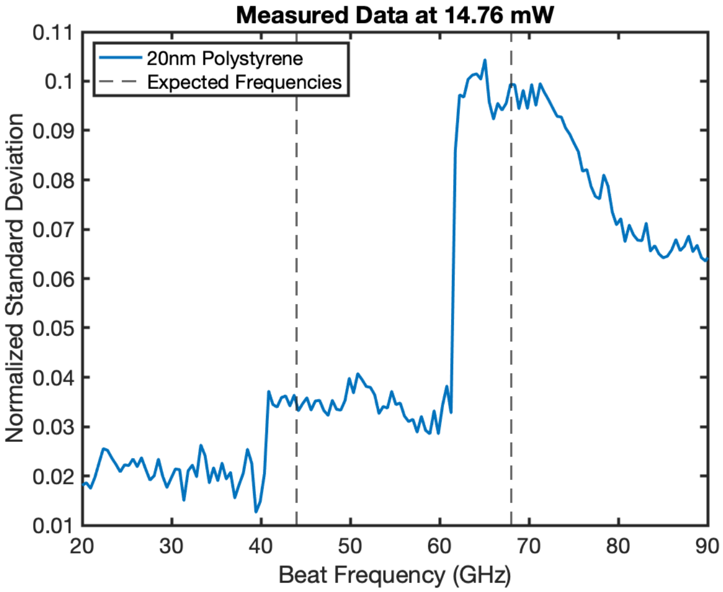

Figure 4.7: EAR spectrum of 20 nm polystyrene probed at a power higher than optimum range (14.76 mW before the objective lens). Copyright ©2021 SPIE

of the particles properly.

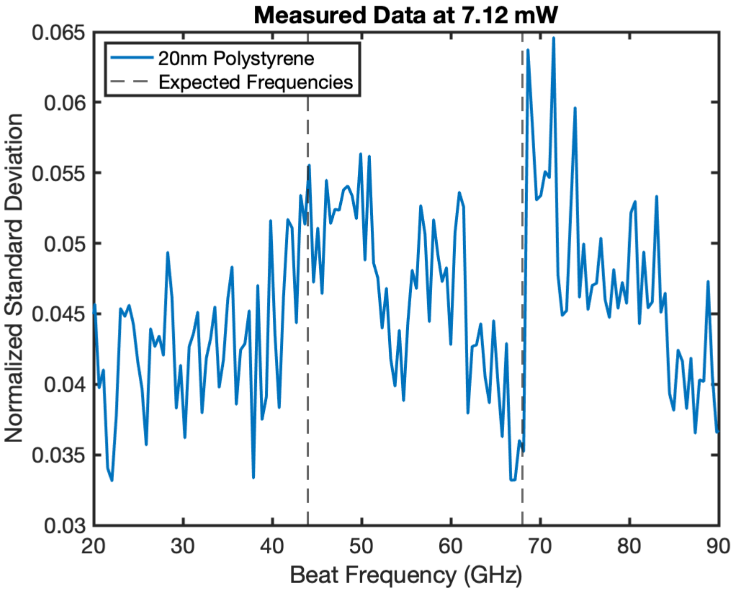

Figure 4.8: EAR spectrum of 20 nm polystyrene probed at a power much lower than the optimum range (7.12 mW before the objective lens). Copyright ©2021 SPIE

Chapter 5

Conclusion and possible future projects

5.1 Conclusion

This thesis is composed of several research endeavors focused on enhancing the sensitivity of SPR sensors and improving trapping capabilities in NOTs. The first project introduces an innovative periodic SRSP design, which can be integrated into existing commercial SPR sensors. In this design, the SRSP operates by coupling with the LSP resonance of rectangular structures. The results demonstrate an impressive 3.3-fold increase in sensitivity. Moreover, noise analysis reveals a four-fold improvement in resolution when utilizing the SRSP design. In the second study, a method is introduced for detecting the location and orientation of DNHs without relying on facilities such as SEM. Additionally, in the typical method of colloidal lithography for fabrication of DNHs, by substituting the PVC substrate, the minimum trapping power decreases by a factor of seven. Furthermore, by employing tape exploitation instead of sonication in ethanol for the removal of polystyrene during the fabrication process of DNHs, the quality of the created apertures improves.

In the last study, using DC voltage in the sample significantly improves protein trapping, making it approximately ten times faster. This method involves positioning the counter electrode on the glass substrate, located on the opposite side of the solution, but in close proximity to the trapping area vertically. This method utilizes the benefits of fringe fields to enhance the speed of particle trapping. Typically, placing the counter electrode within the solution does not contribute significantly to accelerated protein trapping. However, it does demonstrate voltage-dependent acceleration when trapping polystyrene spheres at higher applied voltages. Considering the importance of unmodified protein trapping in NOTs for protein analysis and interaction studies, these modified approaches offer promising solutions. By enabling considerably faster and more straightforward trapping, this technique paves the way for advancements in the field, leading to more efficient and precise analysis of proteins and their interactions.

5.2 Possible future projects

5.2.1 Exploring trapping of lipid nanodiscs

As a future work, it is important to investigate the trapping of lipid nanodiscs, as promising possibilities lie in studying the response of functional G protein-coupled receptors (GPCRs) reconstituted within these nanodiscs using optical tweezers. Trapping lipid nanodiscs not only allows for the exploration of GPCR behavior in a controlled and physiologically relevant lipid environment but also provides an opportunity to examine the effects of specific ligands, such as ZM and NECA. By employing optical tweezers, we can precisely manipulate and trap individual lipid nanodiscs containing reconstituted GPCRs, enabling us to investigate their dynamic response to ligand binding, conformational changes, and downstream signaling pathways. Understanding the impact of ZM and NECA ligands on GPCR function within lipid nanodiscs can offer valuable insights into the intricacies of ligand-receptor interactions and potentially unveil novel therapeutic strategies for modulating GPCR signaling. Therefore, further investigations into the trapping of functional GPCRs reconstituted in lipid nanodiscs, coupled with the examination of ZM and NECA ligands, hold significant promise for advancing our understanding of GPCR biology and facilitating the development of targeted interventions for various physiological processes and diseases.

Figure 5.1 shows preliminary results for the trapping event of GPCR itself, as well as when the ligands are added to the solution in parts b and c.

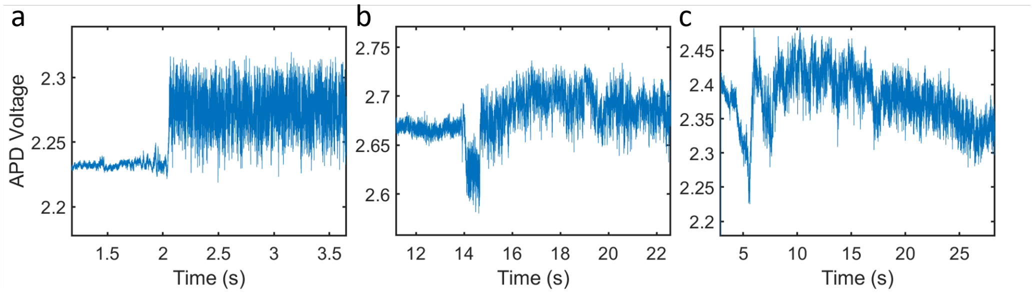

Figure 5.1: Trapping event of a) G protein. b) G protein and NECA ligand c) G protein and ZM ligand.

5.2.2 Small molecule binding

Investigating the effects of small molecule ligands, specifically the small molecule activators of PP2A (SMAPs), is of highest importance. These SMAPs have shown the ability to activate the PP2A complex; however, their precise mechanisms of action remain elusive. To unravel the intricate details of SMAP binding and its impact on PP2A function, the utilization of optical tweezers for trapping the PP2A complex and small molecule ligands is of paramount importance. Trapping the PP2A complex in combination with optical tweezers also enables the exploration of the specific interactions between SMAPs and the complex's subunits, such as the regulatory subunit PR65. Understanding the binding mechanisms and dynamics of SMAPs with PR65 is crucial for unraveling their mode of action in activating PP2A. By observing and manipulating the interactions between PR65 and SMAPs, researchers can gain valuable insights into the structural and functional changes induced by ligand binding, shedding light on the intricate regulatory processes involved in PP2A activation.

Furthermore, optical tweezers provide the means to study the effects of different SMAP variants and their specific structural features on PP2A activation. This knowledge is vital for designing novel SMAPs with improved efficacy and selectivity, paving the way for the development of targeted interventions for various physiological processes and diseases.

Bibliography

[1] SY Wu, HP Ho, Wing Cheung Law, Chinlon Lin, and SK Kong. Highly sensitive differential phase-sensitive surface plasmon resonance biosensor based on the mach–zehnder configuration. *Optics Letters*, 29(20):2378–2380, 2004.

[2] Al A Kolomenskii, PD Gershon, and HA Schuessler. Sensitivity and detection limit of concentration and adsorption measurements by laser-induced surface-plasmon resonance. *Applied optics*, 36(25):6539–6547, 1997.

[3] Timothy M Chinowsky, Linda S Jung, and Sinclair S Yee. Optimal linear data analysis for surface plasmon resonance biosensors. *Sensors and Actuators B: Chemical*, 54(1-2):89–97, 1999.

[4] Lo Gorton. *Biosensors and modern biospecific analytical techniques.* Elsevier, 2005.

[5] Borja Sepúlveda, A Calle, Laura M Lechuga, and G Armelles. Highly sensitive detection of biomolecules with the magneto-optic surface-plasmon-resonance sensor. *Optics Letters*, 31(8):1085–1087, 2006.

[6] Ankun Yang, Danqing Wang, Weijia Wang, and Teri W Odom. Coherent light sources at the nanoscale. *Annual Review of Physical Chemistry*, 68:83–99, 2017.

[7] Erwin Kretschmann and Heinz Raether. Radiative decay of non radiative surface plasmons excited by light. *Zeitschrift für Naturforschung A*, 23(12):2135–2136, 1968.

[8] Andreas Otto. Excitation of nonradiative surface plasma waves in silver by the method of frustrated total reflection. *Zeitschrift für Physik A Hadrons and nuclei*, 216(4):398–410, 1968.

[9] Stefan Alexander Maier. *Plasmonics: fundamentals and applications*. Springer Science & Business Media, 2007.

[10] Jiri Homola, Sookyoung S Yee, and Günter Gauglitz. Long-range surface plasmons on dielectric-coated thin metal films. *Optics Communications*, 162(1-3):1–6, 1999.

[11] Christopher M Michaels, Joseph Chen, Harald Giessen, and Lukas A Schaefer. Observation of short-range surface plasmons in silver nanoparticle arrays by interferometric reflectance imaging. *Optics Express*, 16(22):17654–17666, 2008.

[12] Arthur Ashkin, James M Dziedzic, JE Bjorkholm, and Steven Chu. Observation of a single-beam gradient force optical trap for dielectric particles. *Optics Letters*, 11(5):288–290, 1986.

[13] Arthur Ashkin and James M Dziedzic. Optical trapping and manipulation of viruses and bacteria. *Science*, 235(4795):1517–1520, 1987.

[14] PW Smith, Arthur Ashkin, and WJ Tomlinson. Four-wave mixing in an artificial kerr medium. *Optics Letters*, 6(6):284–286, 1981.

[15] Arthur Ashkin, JM Dziedzic, and PW Smith. Continuous-wave self-focusing and self-trapping of light in artificial kerr media. *Optics Letters*, 7(6):276–278, 1982.

[16] EX Jin and X Xu. Plasmonic effects in near-field optical transmission enhancement through a single bowtie-shaped aperture. *Applied Physics B*, 84(1):3–9, 2006.

[17] Liang Wang, Sreemanth M Uppuluri, Eric X Jin, and Xianfan Xu. Nanolithography using high transmission nanoscale bowtie apertures. *Nano Letters*, 6(3):361–364, 2006.

[18] Bin Ai, Ye Yu, Helmuth Möhwald, and Gang Zhang. Novel 3D Au nanohole arrays with outstanding optical properties. *Nanotechnology*, 24(3):035303, 2012.

[19] Bin Ai, Limin Wang, Helmuth Möhwald, Ye Yu, and Gang Zhang. Asymmetric half-cone/nanohole array films with structural and directional reshaping of extraordinary optical transmission. *Nanoscale*, 6(15):8997–9005, 2014.

[20] Poul M Bendix and Lene B Oddershede. Expanding the optical trapping range of lipid vesicles to the nanoscale. *Nano Letters*, 11(12):5431–5437, 2011.

[21] Arthur Ashkin and JM Dziedzic. Feedback stabilization of optically levitated particles. *Applied Physics Letters*, 30(4):202–204, 1977.

[22] Robert M Simmons, Jeffrey T Finer, Steven Chu, and James A Spudich. Quantitative measurements of force and displacement using an optical trap. *Biophysical Journal*, 70(4):1813–1822, 1996.

[23] Anders E Wallin, Heikki Ojala, Edward Hæggström, and Roman Tuma. Stiffer optical tweezers through real-time feedback control. *Applied Physics Letters*, 92(22):224104, 2008.

[24] Faegheh Hajizadeh and S Nader S Reihani. Optimized optical trapping of gold nanoparticles. *Optics Express*, 18(2):551–559, 2010.

[25] Liselotte Jauffred and Lene B Oddershede. Two-photon quantum dot excitation during optical trapping. *Nano Letters*, 10(5):1927–1930, 2010.

[26] Poul Martin Hansen, Vikram Kjøller Bhatia, Niels Harrit, and Lene Oddershede. Expanding the optical trapping range of gold nanoparticles. *Nano Letters*, 5(10):1937–1942, 2005.

[27] Allen HJ Yang, Sean D Moore, Bradley S Schmidt, Matthew Klug, Michal Lipson, and David Erickson. Optical manipulation of nanoparticles and biomolecules in sub-wavelength slot waveguides. *Nature*, 457(7225):71–75, 2009.

[28] Mathieu L Juan, Reuven Gordon, Yuanjie Pang, Fatima Eftekhari, and Romain Quidant. Self-induced back-action optical trapping of dielectric nanoparticles. *Nature Physics*, 5(12):915, 2009.

[29] CS Adams and E Riis. Laser cooling and trapping of neutral atoms. *Progress in Quantum Electronics*, 21(1):1–79, 1997.

[30] PWH Pinkse, T Fischer, P Maunz, and G Rempe. Trapping an atom with single photons. *Nature*, 404(6776):365–368, 2000.

[31] Takuya Iida and Hajime Ishihara. Theoretical study of the optical manipulation of semiconductor nanoparticles under an excitonic resonance condition. *Physical Review Letters*, 90(5):057403, 2003.

[32] Yuanjie Pang and Reuven Gordon. Optical trapping of 12 nm dielectric spheres using double-nanoholes in a gold film. *Nano Letters*, 11(9):3763–3767, 2011.

[33] Abhay Kotnala and Reuven Gordon. Quantification of high-efficiency trapping of nanoparticles in a double nanohole optical tweezer. *Nano Letters*, 14(2):853–856, 2014.

[34] Abhay Kotnala, Damon DePaoli, and Reuven Gordon. Sensing nanoparticles using a double nanohole optical trap. *Lab on a Chip*, 13(20):4142–4146, 2013.

[35] Skyler Wheaton and Reuven Gordon. Molecular weight characterization of single globular proteins using optical nanotweezers. *Analyst*, 140(14):4799–4803, 2015.

[36] Ahmed A Al Balushi, Abhay Kotnala, Skyler Wheaton, Ryan M Gelfand, Yashaswini Rajashekara, and Reuven Gordon. Label-free free-solution nanoaperture optical tweezers for single molecule protein studies. *Analyst*, 140(14):4760–4778, 2015.

[37] Matthew R Groves, Neil Hanlon, Patric Turowski, Brian A Hemmings, and David Barford. The structure of the protein phosphatase 2A PR65/A subunit reveals the conformation of its 15 tandemly repeated heat motifs. *Cell*, 96(1):99–110, 1999.

[38] Uhn Soo Cho and Wenqing Xu. Crystal structure of a protein phosphatase 2a heterotrimeric holoenzyme. *Nature*, 445(7123):53–57, 2007.

[39] Hans-Jürgen Butt and Michael Kappl. *Surface and interfacial forces*. John Wiley & Sons, 2018.

[40] Soo-Jin Park and Min-Kang Seo. *Interface science and composites*, volume 18. Academic Press, 2011.

[41] Sven H Behrens and David G Grier. The charge of glass and silica surfaces. *The Journal of Chemical Physics*, 115(14):6716–6721, 2001.

[42] K Ohsawa, M Murata, and H Ohshima. Zeta potential and surface charge density of polystyrene-latex; comparison with synaptic vesicle and brush border membrane vesicle. *Colloid and Polymer Science*, 264(12):1005–1009, 1986.

[43] Esben Thormann, Adam C Simonsen, Per L Hansen, and Ole G Mouritsen. Interactions between a polystyrene particle and hydrophilic and hydrophobic surfaces in aqueous solutions. *Langmuir*, 24(14):7278–7284, 2008.

[44] Adarsh Lalitha Ravindranath, Mirali Seyed Shariatdoust, Samuel Mathew, and Reuven Gordon. Colloidal lithography double-nanohole optical trapping of nanoparticles and proteins. *Optics Express*, 27(11):16184–16194, 2019.

[45] Chuchuan Hong, Sen Yang, and Justus C Ndukaife. Stand-off trapping and manipulation of sub-10 nm objects and biomolecules using opto-thermo-electrohydrodynamic tweezers. *Nat. Nanotechnol.*, 15(11):908–913, 2020.

[46] Kevin J Freedman, Lauren M Otto, Aleksandar P Ivanov, Avijit Barik, Sang-Hyun Oh, and Joshua B Edel. Nanopore sensing at ultra-low concentrations using single-molecule dielectrophoretic trapping. *Nature Communications*, 7(1):1–9, 2016.

[47] Avijit Barik, Lauren M Otto, Daehan Yoo, Jincy Jose, Timothy W Johnson, and Sang-Hyun Oh. Dielectrophoresis-enhanced plasmonic sensing with gold nanohole arrays. *Nano Letters*, 14(4):2006–2012, 2014.

[48] Theodore Anyika, Chuchuan Hong, and Justus C Ndukaife. High-speed nanoscale optical trapping with plasmonic double nanohole aperture. *Nanoscale*, 2023.

[49] Peter V Cornish and Taekjip Ha. A survey of single-molecule techniques in chemical biology. *ACS Chemical Biology*, 2(1):53–61, 2007.

[50] Feng Liang, Yuzheng Guo, Shaocong Hou, and Qimin Quan. Photonic-plasmonic hybrid single-molecule nanosensor measures the effect of fluorescent labels on dna-protein dynamics. *Science Advances*, 3(5):e1602991, 2017.

[51] Chenyu Wen, Eva Bertosin, Xin Shi, Cees Dekker, and Sonja Schmid. Orientation-locked dna origami for stable trapping of small proteins in the nanopore electro-osmotic trap. *Nano Letters*, pages 788–794, 2022.

[52] Lee Priest, Jack S Peters, and Philipp Kukura. Scattering-based light microscopy: From metal nanoparticles to single proteins. *Chemical Reviews*, 121(19):11937–11970, 2021.

[53] Mahyar Dahmardeh, Houman Mirzaalian Dastjerdi, Hisham Mazal, Harald Köstler, and Vahid Sandoghdar. Self-supervised machine learning pushes the

sensitivity limit in label-free detection of single proteins below 10 kda. *Nature Methods*, 20:1–6, 2023.

[54] Justus C Ndukaife, Alexander V Kildishev, Agbai George Agwu Nnanna, Vladimir M Shalaev, Steven T Wereley, and Alexandra Boltasseva. Long-range and rapid transport of individual nano-objects by a hybrid electrothermoplasmonic nanotweezer. *Nat. Nanotechnol.*, 11(1):53, 2016.

[55] Elham Babaei, Ghazal Hajisalem, Shohei Iwamoto, Burak Kaynak, Pemra Doruker, Mohsin M Naqvi, Janet Kumita, Feng-Yu Wang, Jhih-Hong Cheng, Che-Min Wu, Shang-Hua Yang, Ivet Bahar, Laura Itzhaki, and Reuven Gordon. Extraordinary acoustic raman spectroscopy of pr65. In *2021 IEEE 16th Nanotechnology Materials and Devices Conference (NMDC)*, pages 1–4. IEEE, 2021.

[56] Paul B Bareil and Yunlong Sheng. Optical trapping of the anisotropic crystal nanorod. *Optics Express*, 23(10):13130–13140, 2015.

[57] Fan Nan and Zijie Yan. Silver-nanowire-based interferometric optical tweezers for enhanced optical trapping and binding of nanoparticles. *Advanced Functional Materials*, 29(7):1808258, 2019.

[58] Yuichi Kozawa and Shunichi Sato. Optical trapping of micrometer-sized dielectric particles by cylindrical vector beams. *Optics Express*, 18(10):10828–10833,

2010.

[59] Ghazal Hajisalem, Mirali Seyed Shariatdoust, Rana Faryad Ali, Byron D Gates, Paul E Barclay, and Reuven Gordon. Single nanoflake hexagonal boron nitride harmonic generation with ultralow pump power. *ACS Photonics*, 8(7):1922–1926, 2021.

[60] Anthony L Forget, Christopher C Dombrowski, Ichiro Amitani, and Stephen C Kowalczykowski. Exploring protein-dna interactions in 3d using in situ construction, manipulation and visualization of individual dna dumbbells with optical traps, microfluidics and fluorescence microscopy. *Nature Protocols*, 8(3):525–538, 2013.

[61] Satish Rao, Saurabh Raj, Stefan Balint, Carlota Bardina Fons, Susana Campoy, Montserrat Llagostera, and Dmitri Petrov. Single dna molecule detection in an optical trap using surface-enhanced raman scattering. *Applied Physics Letters*, 96(21):213701, 2010.

[62] Abhay Kotnala and Reuven Gordon. Double nanohole optical tweezers visualize protein p53 suppressing unzipping of single dna-hairpins. *Biomedical Optics Express*, 5(6):1886–1894, 2014.

[63] Reuven Gordon. Biosensing with nanoaperture optical tweezers. *Optics & Laser Technology*, 109:328–335, 2019.

[64] Dana Cialla, Anne März, René Böhme, Frank Theil, Karina Weber, Michael Schmitt, and Jürgen Popp. Surface-enhanced Raman spectroscopy (SERS): progress and trends. *Analytical and Bioanalytical Chemistry*, 403(1):27–54, 2012.

[65] Adrien Nicolaï, Patrice Delarue, and Patrick Senet. Low-frequency, functional, modes of proteins: all-atom and coarse-grained normal mode analysis. *Computational Methods to Study the Structure and Dynamics of Biomolecules and Biomolecular Processes: From Bioinformatics to Molecular Quantum Mechanics*, pages 483–524, 2014.

[66] Skyler Wheaton, Ryan M Gelfand, and Reuven Gordon. Probing the raman-active acoustic vibrations of nanoparticles with extraordinary spectral resolution. *Nature Photonics*, 9(1):68, 2015.

[67] NN Ovsyuk and VN Novikov. Influence of a glass matrix on acoustic phonons confined in microcrystals. *Physical Review B*, 53(6):3113, 1996.

[68] M Ivanda, A Hohl, M Montagna, G Mariotto, M Ferrari, Z Crnjak Orel, A Turković, and K Furić. Raman scattering of acoustical modes of silicon nanoparticles embedded in silica matrix. *Journal of Raman Spectroscopy*, 37(1-3):161–165, 2006.

[69] Catherine Pighini, Daniel Aymes, Nadine Millot, and Lucien Saviot. Low-frequency raman characterization of size-controlled anatase tio 2 nanopowders prepared by continuous hydrothermal syntheses. *Journal of Nanoparticle Research*, 9(2):309–315, 2007.

[70] T Still, M Mattarelli, D Kiefer, G Fytas, and M Montagna. Eigenvibrations of submicrometer colloidal spheres. *The Journal of Physical Chemistry Letters*, 1(16):2440–2444, 2010.

[71] Elham Babaei, Samuel Mathew, Mirali Seyed Shariatdoust, Demelza Wright, Laura Itzhaki, Ivet Bahar, Shang-Hua Yang, and Reuven Gordon. Analysis of single unmodified proteins and their interactions with nanoaperture optical tweezers: Pr65 case study. In *Optical Manipulation and Its Applications*, pages AM3D–5. Optica Publishing Group, 2023.

[72] Elham Babaei, Ghazal Haji Salem, Shohei Iwamoto, and Reuven Gordon. Probing optimum applied power for extraordinary acoustic raman spectroscopy. In *Optical Trapping and Optical Micromanipulation XVIII*, volume 11798, pages 148–152. SPIE, 2021.

[73] A. Ashkin, J. M. Dziedzic, J. E. Bjorkholm, and S. Chu. Observation of a single-beam gradient force optical trap for dielectric particles. *Optics Letters*, 11(5):288–290, 1986.

[74] Kishan Dholakia, Peter Reece, and Min Gu. Optical micromanipulation. *Chem. Soc. Rev.*, 37:42–55, 2008.

[75] Karel Svoboda and Steven M Block. Optical trapping of metallic rayleigh particles. *Optics letters*, 19(13):930–932, 1994.

[76] A. Aashkin, J. M. Dziedzic, J. E. Bjorkholm, and S. Chu. Observation of a single-beam gradient force optical trap for dielectric particles. *Optics Letters*, 11(5):288–290, 1986.

[77] Ahmed A. Al Balushi, Abhay Kotnala, Skyler Wheaton, Ryan M. Gelfand, Yashaswini Rajashekara, and Reuven Gordon. Label-free free-solution nanoaperture optical tweezers for single molecule protein studies. *Analyst (London)*, 14(14):476–4778, 2015.

[78] Aniket Chowdhury, Deepak Waghmare, Raktim Dasgupta, and Shovan K. Majumder. Red blood cell membrane damage by light-induced thermal gradient under optical trap. *Journal of Biophotonics*, 11(8):e201700222, 2018.

[79] O. L. Kantidze, A. K. Velichko, A. V. Luzhin, and S. V. Razin. Heat stress-induced dna damage. *Actanaturae*, 8(2):75–78, 2016.

[80] Yuanjie Pang and Reuven Gordon. Optical trapping of a single protein. *Nano Letters*, 12(1):402–406, 2012.

[81] Abhay Kotnala and Reuven Gordon. Double nanohole optical tweezers visualize protein p53 suppressing unzipping of single dna-hairpins. *Biomedical Optics Express*, 5(6):1886–1894, 2014.

[82] Skyler Wheaton, Ryan M. Gelfand, and Reuven Gordon. Probing the raman-active acoustic vibrations of nanoparticles with extraordinary spectral resolution. *Nature Photonics*, 9(1):68–72, 2014.

[83] Adrien Nicolaï, Patrice Delarue, and Patrick Senet. *Low-Frequency, Functional, Modes of Proteins: All-Atom and Coarse-Grained Normal Mode Analysis*, pages 483–524. Springer Berlin Heidelberg, Berlin, Heidelberg, 2014.

[84] Elham Babaei, Zohreh Sharifi, and Reuven Gordon. Improving sensitivity of existing surface plasmon resonance systems with grating-coupled short-range surface plasmons. *JOSA B*, 36(8):F144–F148, 2019.

[85] Jonathan Zenneck. Über die fortpflanzung ebener elektromagnetischer wellen längs einer ebenen leiterfläche und ihre beziehung zur drahtlosen telegraphie. *Annalen der Physik*, 328(10):846–866, 1907.

[86] Erwin Kretschmann. Die bestimmung optischer konstanten von metallen durch anregung von oberflächenplasmaschwingungen. *Zeitschrift für Physik A Hadrons and nuclei*, 241(4):313–324, 1971.

[87] Bo Liedberg, Claes Nylander, and Ingemar Lundström. Biosensing with surface plasmon resonance—how it all started. *Biosensors and Bioelectronics*, 10(8):i–ix, 1995.

[88] EN Economou. Surface plasmons in thin films. *Physical Review*, 182(2):539, 1969.

[89] Pierre Berini. Bulk and surface sensitivities of surface plasmon waveguides. *New Journal of Physics*, 10(10):105010, 2008.

[90] Gilad Rosenblatt, Boris Simkhovich, and Meir Orenstein. Brewster plasmons: new optical degrees of freedom driving the forced repose of nanostructures (conference presentation). In *Metamaterials, Metadevices, and Metasystems 2018*, volume 10719, page 107191R. International Society for Optics and Photonics, 2018.

[91] Cavour Yeh and Fred I Shimabukuro. *The essence of dielectric waveguides*. Springer, 2008.

[92] MG Moharam and Thomas K Gaylord. Rigorous coupled-wave analysis of metallic surface-relief gratings. *JOSA A*, 3(11):1780–1787, 1986.

[93] Suntak Park, Gwansu Lee, Seok Ho Song, Cha Hwan Oh, and Pill Soo Kim. Resonant coupling of surface plasmons to radiation modes by use of dielectric gratings. *Optics Letters*, 28(20):1870–1872, 2003.

[94] Peter Offermans, Martijn C Schaafsma, Said RK Rodriguez, Yichen Zhang, Mercedes Crego-Calama, Sywert H Brongersma, and Jaime Gómez Rivas. Universal scaling of the figure of merit of plasmonic sensors. *ACS Nano*, 5(6):5151–5157, 2011.

[95] Marek Piliarik and Jiří Homola. Surface plasmon resonance (spr) sensors: approaching their limits? *Optics Express*, 17(19):16505–16517, 2009.

[96] Prashant Nagpal, Nathan C Lindquist, Sang-Hyun Oh, and David J Norris. Ultrasmooth patterned metals for plasmonics and metamaterials. *Science*, 325(5940):594–597, 2009.

[97] Anna Kossoy, Virginia Merk, Denis Simakov, Kristjan Leosson, Stéphane Kéna-Cohen, and Stefan A Maier. Optical and structural properties of ultra-thin gold films. *Advanced Optical Materials*, 3(1):71–77, 2015.

[98] AV Kabashin, P Evans, S Pastkovsky, W Hendren, GA Wurtz, R Atkinson, R Pollard, VA Podolskiy, and AV Zayats. Plasmonic nanorod metamaterials for biosensing. *Nature Materials*, 8(11):867, 2009.

[99] Ghazal Hajisalem, Elham Babaei, Michael Dobinson, Shohei Iwamoto, Zohreh Sharifi, Jon Eby, Marie Synakewicz, Laura S Itzhaki, and Reuven Gordon. Accessible high-performance double nanohole tweezers. *Optics Express*, 30(3):3760–3769, 2022.

[100] Eun-Soo Kwak, Tiberiu-Dan Onuta, Dragos Amarie, Radislav Potyrailo, Barry Stein, Stephen C Jacobson, WL Schaich, and Bogdan Dragnea. Optical trapping with integrated near-field apertures. *The Journal of Physical Chemistry B*, 108(36):13607–13612, 2004.

[101] Tiberiu-Dan Onuta, Matthias Waegele, Christopher C DuFort, William L Schaich, and Bogdan Dragnea. Optical field enhancement at cusps between adjacent nanoapertures. *Nano Letters*, 7(3):557–564, 2007.

[102] Mathieu L Juan, Maurizio Righini, and Romain Quidant. Plasmon nano-optical tweezers. *Nature Photonics*, 5(6):349–356, 2011.

[103] Quanbo Jiang, Jean-Benoît Claude, and Jérôme Wenger. Plasmonic nano-optical trap stiffness measurements and design optimization. *Nanoscale*, 13(7):4188–4194, 2021.

[104] Daehan Yoo, Kargal L Gurunatha, Han-Kyu Choi, Daniel A Mohr, Christopher T Ertsgaard, Reuven Gordon, and Sang-Hyun Oh. Low-power optical trapping of nanoparticles and proteins with resonant coaxial nanoaperture using 10 nm gap. *Nano Letters*, 18(6):3637–3642, 2018.

[105] J Berthelot, SS Aćimović, ML Juan, MP Kreuzer, J Renger, and R Quidant. Three-dimensional manipulation with scanning near-field optical nanotweezers. *Nature Nanotechnology*, 9(4):295, 2014.

[106] Amr AE Saleh and Jennifer A Dionne. Toward efficient optical trapping of sub-10-nm particles with coaxial plasmonic apertures. *Nano Letters*, 12(11):5581–5586, 2012.

[107] I-Chun Huang, Jeffrey Holzgrafe, Russell A Jensen, Jennifer T Choy, Moungi G Bawendi, and Marko Lončar. 10 nm gap bowtie plasmonic apertures fabricated by modified lift-off process. *Applied Physics Letters*, 109(13):133105, 2016.

[108] Quanbo Jiang, Benoît Rogez, Jean-Benoît Claude, Guillaume Baffou, and Jérôme Wenger. Quantifying the role of the surfactant and the thermophoretic force in plasmonic nano-optical trapping. *Nano Letters*, 20(12):8811–8817, 2020.

[109] Muhammad Usman Raza, Sai Santosh Sasank Peri, Liang-Chieh Ma, Samir M Iqbal, and George Alexandrakis. Self-induced back action actuated nanopore electrophoresis (SANE). *Nanotechnology*, 29(43):435501, 2018.

[110] Hongtao Tan, Huiqian Hu, Lin Huang, and Kun Qian. Plasmonic tweezers for optical manipulation and biomedical applications. *Analyst*, 145(17):5699–5712, 2020.

[111] Yuquan Zhang, Changjun Min, Xiujie Dou, Xianyou Wang, Hendrik Paul Urbach, Michael G Somekh, and Xiaocong Yuan. Plasmonic tweezers: for nanoscale optical trapping and beyond. *Light: Science & Applications*, 10(1):1–41, 2021.

[112] Theodoros D Bouloumis, Domna G Kotsifaki, Xue Han, Síle Nic Chormaic, and Viet Giang Truong. Fast and efficient nanoparticle trapping using plasmonic connected nanoring apertures. *Nanotechnology*, 32(2):025507, 2020.

[113] Abhay Kotnala, Hongru Ding, and Yuebing Zheng. Enhancing single-molecule fluorescence spectroscopy with simple and robust hybrid nanoapertures. *ACS Photonics*, 2021.

[114] Neuton Li, Jasper Cadusch, Amelia Liu, Anders J Barlow, Ann Roberts, and Kenneth B Crozier. Algorithm-designed plasmonic nanotweezers: Quantitative comparison by theory, cathodoluminescence, and nanoparticle trapping. *Advanced Optical Materials*, 9(19):2100758, 2021.

[115] Zhe Xu, Wuzhou Song, and Kenneth B Crozier. Direct particle tracking observation and brownian dynamics simulations of a single nanoparticle optically trapped by a plasmonic nanoaperture. *ACS Photonics*, 5(7):2850–2859, 2018.

[116] Quanbo Jiang, Prithu Roy, Jean-Benoît Claude, and Jérôme Wenger. Single photon source from a nanoantenna-trapped single quantum dot. *Nano Letters*, 21(16):7030–7036, 2021.

[117] Amirhossein Alizadehkhaledi, Adriaan L Frencken, Frank CJM van Veggel, and Reuven Gordon. Isolating nanocrystals with an individual erbium emitter: A

route to a stable single-photon source at 1550 nm wavelength. *Nano Letters*, 20(2):1018–1022, 2019.

[118] Mirali Seyed Shariatdoust, Adriaan L Frencken, Ali Khademi, Amirhossein Alizadehkhaledi, Frank CJM van Veggel, and Reuven Gordon. Harvesting dual-wavelength excitation with plasmon-enhanced emission from upconverting nanoparticles. *ACS Photonics*, 5(9):3507–3512, 2018.

[119] Russell A Jensen, I-Chun Huang, Ou Chen, Jennifer T Choy, Thomas S Bischof, Marko Loncar, and Moungi G Bawendi. Optical trapping and two-photon excitation of colloidal quantum dots using bowtie apertures. *ACS Photonics*, 3(3):423–427, 2016.

[120] Zohreh Sharifi, Michael Dobinson, Ghazal Hajisalem, Mirali Seyed Shariatdoust, Adriaan L Frencken, Frank CJM van Veggel, and Reuven Gordon. Isolating and enhancing single-photon emitters for 1550 nm quantum light sources using double nanohole optical tweezers. *Journal of Chemical Physics*, 154(18):184204, 2021.

[121] Haitian Xu, Steven Jones, Byoung-Chul Choi, and Reuven Gordon. Characterization of individual magnetic nanoparticles in solution by double nanohole optical tweezers. *Nano Letters*, 16(4):2639–2643, 2016.

[122] Maxim Belkin, Shu-Han Chao, Magnus P Jonsson, Cees Dekker, and Aleksei Aksimentiev. Plasmonic nanopores for trapping, controlling displacement, and sequencing of dna. *ACS Nano*, 9(11):10598–10611, 2015.

[123] Yuanjie Pang and Reuven Gordon. Optical trapping of a single protein. *Nano Letters*, 12(1):402–406, 2012.

[124] Xiaolei Peng, Abhay Kotnala, Bharath Bangalore Rajeeva, Mingsong Wang, Kan Yao, Neel Bhatt, Daniel Penley, and Yuebing Zheng. Plasmonic nanotweezers and nanosensors for point-of-care applications. *Advanced Optical Materials*, page 2100050, 2021.

[125] Cuifeng Ying, Edona Karakaci, Esteban Bermudez-Urena, Alessandro Ianiro, Ceri Foster, Saurabh Awasthi, Anirvan Guha, Louise Bryan, Jonathan List, Sandor Balog, Guillermo P Acuna, Reuven Gordon, and Michael Mayer. Watching single unmodified enzymes at work. *arXiv:2107.06407*, 2021.

[126] Daniel Verschueren, Xin Shi, and Cees Dekker. Nano-optical tweezing of single proteins in plasmonic nanopores. *Small Methods*, page 1800465, 2019.

[127] Skyler Wheaton and Reuven Gordon. Single molecule protein sizing in double nano-hole optical tweezers. In *Optical Trapping Applications*, pages OtM3E–5. Optical Society of America, 2015.

[128] Sai Santosh Sasank Peri, Manoj Kumar Sabnani, Muhammad Usman Raza, Elizabeth L Urquhart, Soroush Ghaffari, Jung Soo Lee, Min Jun Kim, Jon Weidanz, and George Alexandrakis. Quantification of low affinity binding interactions between natural killer cell inhibitory receptors and targeting ligands with a self-induced back-action actuated nanopore electrophoresis (SANE) sensor. *Nanotechnology*, 32(4):045501, 2020.

[129] Ahmed A Al Balushi and Reuven Gordon. Label-free free-solution single-molecule protein–small molecule interaction observed by double-nanohole plasmonic trapping. *ACS Photonics*, 1(5):389–393, 2014.

[130] Sai Santosh Sasank Peri, Manoj K Sabnani, Muhammad Usman Raza, Soroush Ghaffari, Susanne Gimlin, Debra D Wawro, Jung Soo Lee, Min Jun Kim, Jon Weidanz, and George Alexandrakis. Detection of specific antibody-ligand interactions with a self-induced back-action actuated nanopore electrophoresis sensor. *Nanotechnology*, 31(8):085502, 2019.

[131] Ana Zehtabi-Oskuie, Hao Jiang, Bryce R Cyr, Douglas W Rennehan, Ahmed A Al-Balushi, and Reuven Gordon. Double nanohole optical trapping: dynamics and protein-antibody co-trapping. *Lab on a Chip*, 13(13):2563–2568, 2013.

[132] J Sotres and AM Baró. AFMimaging and analysis of electrostatic double layer forces on single DNA molecules. *Biophysical Journal*, 98(9):1995–2004, 2010.

[133] Prodip K Das, Subir Bhattacharjee, and Walied Moussa. Electrostatic double layer force between two spherical particles in a straight cylindrical capillary: Finite element analysis. *Langmuir*, 19(10):4162–4172, 2003.

[134] Ahmad Asadinezhad, Márian Lehocký, Petr Sáha, and Miran Mozetič. Recent progress in surface modification of polyvinyl chloride. *Materials*, 5(12):2937–2959, 2012.

[135] Yongan Gu and Dongqing Li. The ζ-potential of glass surface in contact with aqueous solutions. *Journal of Colloid and Interface Science*, 226(2):328–339, 2000.

[136] Haifeng Cai, Yang Wang, Kai Wu, and Weihong Guo. Enhanced hydrophilic and electrophilic properties of polyvinyl chloride (PVC) biofilm carrier. *Polymers*, 12(6):1240, 2020.

[137] Albert Perez-Riba, Marie Synakewicz, and Laura S Itzhaki. Folding cooperativity and allosteric function in the tandem-repeat protein class. *Philosophical Transactions of the Royal Society B: Biological Sciences*, 373(1749):20170188, 2018.

[138] Edward D Palik. *Handbook of optical constants of solids*, volume 3. Academic Press, 1998.

[139] Elham Babaei, Demelza Wright, and Reuven Gordon. Fringe dielectrophoresis nanoaperture optical trapping with order of magnitude speed-up for unmodified proteins. *Nano Letters*, 23(7):2877–2882, 2023.

[140] Sonja Schmid, Pierre Stömmer, Hendrik Dietz, and Cees Dekker. Nanopore electro-osmotic trap for the label-free study of single proteins and their conformations. *Nature Nanotechnology*, 16(11):1244–1250, 2021.

[141] Sarp Kerman, Chang Chen, Yi Li, Wim Van Roy, Liesbet Lagae, and Pol Van Dorpe. Raman fingerprinting of single dielectric nanoparticles in plasmonic nanopores. *Nanoscale*, 7(44):18612–18618, 2015.

[142] Yang Zhao, Amr AE Saleh, and Jennifer A Dionne. Enantioselective optical trapping of chiral nanoparticles with plasmonic tweezers. *ACS Photonics*, 3(3):304–309, 2016.

[143] Yang Zhao, Amr AE Saleh, Marie Anne Van De Haar, Brian Baum, Justin A Briggs, Alice Lay, Olivia A Reyes-Becerra, and Jennifer A Dionne. Nanoscopic control and quantification of enantioselective optical forces. *Nature Nanotechnology*, 12(11):1055–1059, 2017.

[144] Quanbo Jiang, Benoit Rogez, Jean-Benoît Claude, Guillaume Baffou, and Jérôme Wenger. Temperature measurement in plasmonic nanoapertures used for optical trapping. *ACS Photonics*, 6(7):1763–1773, 2019.

[145] Daniel V Verschueren, Sergii Pud, Xin Shi, Lorenzo De Angelis, L Kuipers, and Cees Dekker. Label-free optical detection of dna translocations through plasmonic nanopores. *ACS Nano*, 13(1):61–70, 2018.

[146] Seung Ju Yoon, Da In Song, Jungmin Lee, Myung-Ki Kim, Yong-Hee Lee, and Chang-Kyu Kim. Hopping of single nanoparticles trapped in a plasmonic double-well potential. *Nanophotonics*, 9(16):4729–4735, 2020.

[147] Abhay Kotnala, Pavana Siddhartha Kollipara, Jingang Li, and Yuebing Zheng. Overcoming diffusion-limited trapping in nanoaperture tweezers using opto-thermal-induced flow. *Nano Lett.*, 20(1):768–779, 2019.

[148] Domna G Kotsifaki, Viet Giang Truong, and Sile Nic Chormaic. Fano-resonant, asymmetric, metamaterial-assisted tweezers for single nanoparticle trapping. *arXiv preprint arXiv:2001.08319*, 2020.

[149] Noa Hacohen, Candice JX Ip, and Reuven Gordon. Analysis of egg white protein composition with double nanohole optical tweezers. *ACS Omega*, 3(5):5266–5272, 2018.

[150] Wayne Yang, Madeleine van Dijk, Christian Primavera, and Cees Dekker. Fib-milled plasmonic nanoapertures allow for long trapping times of individual proteins. *iScience*, 24(11):103237, 2021.

[151] John David Jackson. *Classical Electrodynamics*. John Wiley & Sons, Inc., New York, third edition, 1999.

[152] Daniel Otzen. Protein–surfactant interactions: a tale of many states. *Biochim. Biophys. Acta, Proteins Proteomics*, 1814(5):562–591, 2011.

[153] Mark A Hayes. Dielectrophoresis of proteins: Experimental data and evolving theory. *Analytical and Bioanalytical Chemistry*, 412(16):3801–3811, 2020.

[154] Chuchuan Hong and Justus C Ndukaife. Scalable trapping of single nanosized extracellular vesicles using plasmonics. pages 2302.07370. arXiv. http://dx.doi.org/10.48550/arXiv.2302.07370 (accessed March 29, 2023), 2023.

[155] Reto Bader, Andrea Bettio, Annette G Beck-Sickinger, and Oliver Zerbe. Structure and dynamics of micelle-bound neuropeptide y: comparison with unligated npy and implications for receptor selection. *Journal of Molecular Biology*, 305(2):307–329, 2001.

[156] National Center for Biotechnology Information. Pubchem compound summary for cid 16130295, aprotinin, 2023. Accessed on 7 March 2023.

[157] David Akintayo Obe and Toluwase Hezekiah Fatoki. In silico evaluation of the structural dynamics of beta-amylase from sweet potato (ipomoea batatas). *Asian Journal of Biotechnology and Bioresource Technology*, 7(3):1–10, Jun. 2021.

[158] Sigma-Aldrich. Carbonic anhydrase isozyme ii from bovine erythrocytes, 2023. Accessed on 7 March 2023.

[159] Linfang Hu, Leiyan Wu, Chanjuan Lai, Mingliang Li, and Wuying Yang. The influence of ph and concentration on the zeta potential, hydrophobicity of ovt and the relationship between its structure and interfacial behaviors. *Journal of Dispersion Science and Technology*, 43(12):1755–1765, 2022.

[160] Michael Graf, Raquel Galera García, and Hermann Wätzig. Protein adsorption in fused-silica and polyacrylamide-coated capillaries. *Electrophoresis*, 26(12):2409–2417, 2005.

[161] Vida Jafari Azad, Shahab Kasravi, Hojjat Alizadeh Zeinabad, Mehri Memar Bashi Aval, Ali Akbar Saboury, Arash Rahimi, and Mojtaba Falahati. Probing the conformational changes and peroxidase-like activity of cytochrome c upon interaction with iron nanoparticles. *Journal of Biomolecular Structure and Dynamics*, 35(12):2565–2577, 2017.

[162] Nathan Kodjo Mintah Churcher, Sayali Upasham, Paul Rice, Serena Bhadsavle, and Shalini Prasad. Development of a flexible, sweat-based neuropeptide y detection platform. *RSC advances*, 10(39):23173–23186, 2020.

[163] Matheus M Pereira, Rafaela AP Cruz, Mafalda R Almeida, Álvaro S Lima, João AP Coutinho, and Mara G Freire. Single-step purification of ovalbu-

min from egg white using aqueous biphasic systems. *Process Biochemistry*, 51(6):781–791, 2016.

[164] Qian Wang, Min-hsiung Pan, Yi-shiou Chiou, Zhenshun Li, Shudong Wei, Xiaoli Yin, and Baomiao Ding. Mechanistic understanding of the effects of ovalbumin-nanoliposome interactions on ovalbumin emulsifying properties. *LWT*, 157:113067, 2022.

[165] Besnik Krasniqi and Jeremy S Lee. Rnase a does not translocate the alpha-hemolysin pore. *PLoS One*, 9(2):e88004, 2014.

Appendix A

Improving sensitivity of existing surface plasmon resonance systems with grating coupled short range surface plasmons [84]

Originally published:

Babaei E, Sharifi Z, Gordon R. Improving sensitivity of existing surface plasmon resonance systems with grating-coupled short-range surface plasmons. JOSA B. 2019 Aug 1;36(8):F144-8.

Reproduced with permission from Journal of the Optical Society of America B.

A.1 Improving sensitivity of existing surface plasmon resonance systems with grating coupled Short range surface plasmons

A.1.1 Abstract

Here we show that surface plasmon resonance sensors that typically use 760 nm wavelength Kretschmann-Raether coupling to a 50 nm thick gold film can have 3.3 times higher surface sensitivity by using local resonances from periodically arranged short-range modes in the same configuration. Considering shot noise, the resolution was found to improve by four-fold. This was calculated by matching the design wavelength and minima angle as calculated by rigorous coupled wave analysis, giving a grating period of 250 nm in a 10 nm thick gold film and gap length of 40 nm. Finite difference time domain simulations were used to confirm that the short-range modes correspond to a localized surface plasmon resonances. The present short-range plasmon approach can be used to improve the sensitivity in monitoring biomolecule interactions.

A.1.2 Introduction

Conducting surfaces permit guided waves called surface plasmon polaritons (SPPs), the mathematical solutions of which have been known for over a century [85]. A prism can be used to couple light into these surface waves, matching the wave-vector in the high-index prism to the wave-vector of the surface plasmon [7, 86]. Since the metal is lossy, light is absorbed at the coupling condition and this leads to a dip in the reflection [86].

The SPP is exponentially bound to the surface, which gives good sensitivity to changes in refractive index near the surface. This is the premise behind the commercialized surface plasmon resonance (SPR) biosensors [87]. These commercial systems have been engineered with consideration of many factors: the light source wavelength, the light source type (LED vs. laser), the metal type, the metal thickness, the detector type (single channel vs. detector array), the data acquisition (dynamic range, analogue to digital conversion and acquisition time) and cost. With all of this engineering already in place and many such machines in laboratories around the world, it is interesting to consider leveraging the existing commercial SPR platform while using a more sensitive sensor chip.

One potential direction to obtain even greater surface sensitivity is to use short-range surface plasmon (SRSP) modes [88, 89]. In particular, insulator-metal-insualtor (IMI) structures permit SRSP modes that become more tightly confined to the surface as the thickness of the metal is reduced. This leads to greater surface sensitivity. Here we consider the use of these SRSP modes in sensing applications while retaining the popular prism coupling configuration.

The SRSP modes have a larger propagation constant than the usual surface plasmon polaritons. Therefore, to couple into these modes while retaining the same Kretschmann geometry as the usual 50 nm thick gold film, we employ a periodic structure with localized surface plasmon (LSP) resonances. Another feature of these modes is that they are more lossy; therefore, it is expected that their reflection dip will broaden upon coupling.

In this paper, we find a design for SRSP sensing using a rectangular stripe grating and a 10 nm gold film. The 10 nm gold is thick enough to allow for continuous films with standard deposition techniques. Using rigorous coupled wave analysis, we find that the surface sensitivity of these films to an adlayer is 3.3 times higher in terms of angle units and the resolution is improved by four-fold, while operating in the same range as commercial SPR systems. Therefore, we believe these chips may be used for more sensitive SPR sensing in the near future.

A.1.3 Design

A. Standard SPR Sensing

Figure A.1 shows the schematics of typical surface coupling for a conventional SPR and the proposed IMI-grating structure. A metal film is confined between two dielectric layers. Incident light couples to the SPP in case of SPR. Surface resonance only happens when incident angle toward the structure is greater than the critical angle. The parallel component of incident light should match the surface plasmon wave-vector of the metal. Minimum reflection occurs when the energy of the incident photon is transferred to surface plasmon wave.

Figure A.1 (a) shows the standard configuration for uniform 50 nm gold film. Uniform films are suitable for SPPs of a single surface. Figure A.1 (b) shows the proposed scheme with periodic gold structure on glass. This structure allows decreasing gold thickness to 10 nm which increases the confined coupled field significantly.

In conventional SPR sensors, for SPP coupling, the light is angled in the prism to match the SPP wave-vector. The SPP wave-vector is given by:

$$k_{\mathrm{SP}} = k_0 \sqrt{\frac{\epsilon_m \epsilon_d}{\epsilon_m + \epsilon_d}} \tag{A.1}$$

where $k_0 = 2\pi/\lambda$ ($\lambda = 760$ nm), ϵ_m is the relative permittivity of the metal, ϵ_d is the relative permittivity of the adjacent dielectric (in this case water). The wave-vector in the prism is given by:

$$k_{\text{prism}} = k_0 n_{\text{prism}} \sin\theta \tag{A.2}$$

where θ is the angle of incidence in the prism and n_{prism} is the prism's refractive index. In this case the SPP coupling occurs where $k_{\text{SP}} = k_{\text{prism}}$ as shown in Figure A.2.

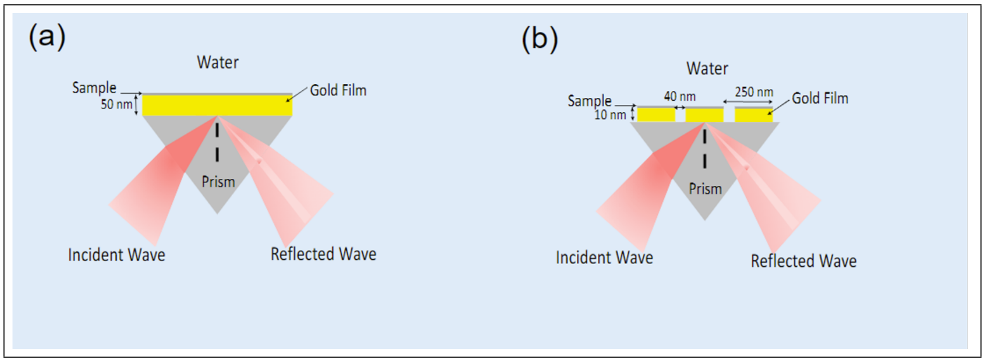

Figure A.1: (a) Prism coupled SPR structure for 50 nm gold film (b) Modified structure for 10 nm gold film using a grating. Copyright ©2019, Journal of the Optical Society of America B

Figure A.3 shows the reflection of a 50 nm gold film when incident through a prism as a function of incident angle. The refractive index of the prism is 1.5 and the top layer is considered to be water with refractive index 1.33. It is clear from this figure that the reflection dip of optimal SPP coupling occurs at around 73°, as expected from the coupling analysis above. (Of course, rigorous coupled wave analysis, or RCWA, is not required for this analysis, since standard transfer matrix theory is applicable to this uniform layer). It is noted that surface plasmon dispersion is for a semi-infinite surface, and so the treatment of using wave coupling through the film is approximate,

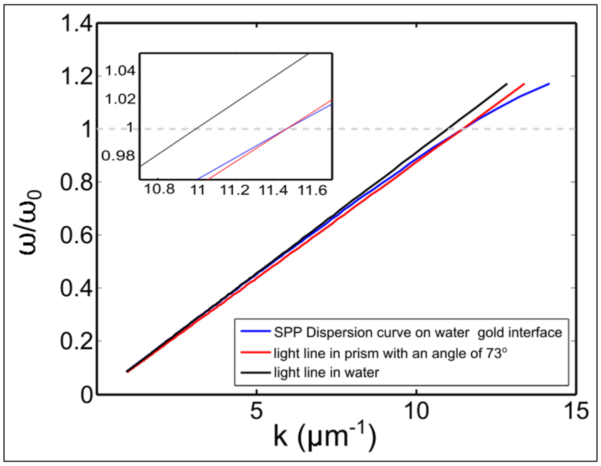

Figure A.2: Dispersion for coupling to surface plasmon at water-gold interface when incident from glass-gold side of the prism. The intersection point is at 73°, which gives a dip due to losses in the SPP. Copyright ©2019, Journal of the Optical Society of America B

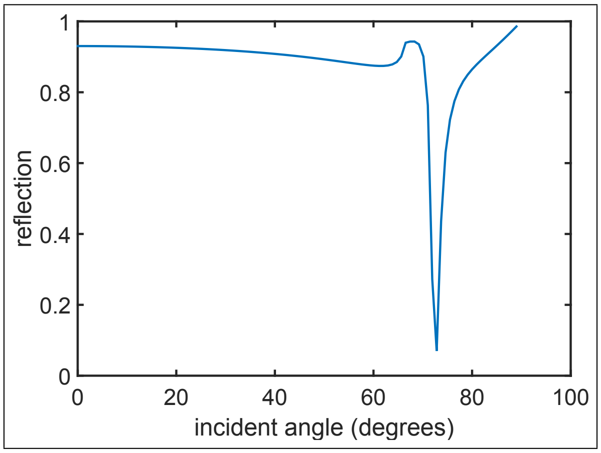

Figure A.3: Reflection from a 50 nm thick gold film on glass with a water top layer for different incident angles. Copyright ©2019, Journal of the Optical Society of America B whereas the RCWA is not [90].

B. SRSP grating-assisted coupling

The propagation constant of a surface plasmon wave on a thin metal film with thickness of h which is bounded by two dielectric media, with subscripts 1 and 3, is determined by following equations [91]:

$$\tanh p_m h(1 + s_1 s_3) = -(s_1 + s_3) \tag{A.3}$$

$$s_1 = \frac{p_1}{p_m}\frac{\epsilon_m}{\epsilon_1} \tag{A.4}$$

$$s_3 = \frac{p_3}{p_m}\frac{\epsilon_m}{\epsilon_3} \tag{A.5}$$

$$p_1^2 = \beta^2 - k_0^2\epsilon_1 \tag{A.6}$$

$$p_m^2 = \beta^2 - k_0^2\epsilon_m \tag{A.7}$$

$$p_3^2 = \beta^2 - k_0^2\epsilon_3 \tag{A.8}$$

where β is the wavevector of the SRSP and k_0 is the free-space wavevector. s_1, s_2 and s_3 are defined for simplicity.

Using these equations, we find that the effective index of the SRSP is 2.58. From this, one can couple to the SRSP by using a periodic structure period of 636 nm to match the wavevector of light in the prism to that of the SRSP using the equation:

$$k_{\text{prism}} + K_G = \beta \tag{A.9}$$

where:

$$K_G = \frac{2\pi}{\Lambda} \tag{A.10}$$

with Λ being the grating period and β is the propagation constant of the SRSP.

We attempted this configuration, and found that coupling was weak (a dip in the reflection of around 30 %). As a result, we considered the possibility of using stronger resonances found in LSPs in an array format.

C. LSP coupling

LSPs are supported by finite metal nanostructures. We first employed RCWA to study periodic LSP structures for prism coupling. RCWA is typically used to study the interaction of an electromagnetic wave with a surface plasmons on a metallic relief grating. RCWA is also reliable approach to determine dips in reflection as a function of wavelength and angle [92, 93].

Figure A.4 shows reflection spectrum for different structures using RCWA method. p is the period of the grating and g is the size of the gap. As shown in the figure for grating period of 250 nm and gap length of 40 nm, the dip occurred for 760 nm incident light, which is the operating wavelength desired at this angle of incidence.

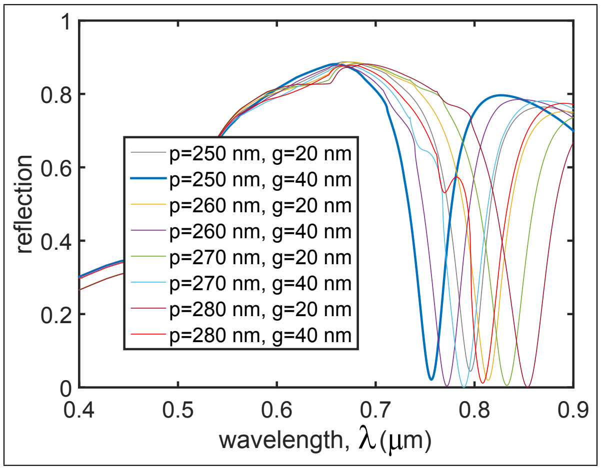

Figure A.4: Reflection spectra periodic structure supporting SRSP mode with an incidence angle of 73°. The period, p, and gap g were varied in each curve to find the case which is most closely matched to the operating wavelength of 760 nm. Copyright ©2019, Journal of the Optical Society of America B

To verify that the origin of this dip is from the LSP resonance, we performed finite-difference time-domain (FDTD) simulations of an isolated structure using the commercial package by Lumerical. We use a grid size of 0.2 nm in the direction perpendicular to the layers and 1 nm in the direction of SRSP propagation. The total domain simulated was 280 nm by 5.75 μm, and bounded by perfectly matched layers. The glass and gold layers were taken from the Palik database. The gold thickness was 10 nm, and its length was 250 nm. A dipole source was placed at one end of the rectangular gold structure and the field intensity was monitored at the peak at the other end of the structure.

Figure A.5 shows the electric field intensity at the end of the gold nanostructure, with a clear peak at the desired operation wavelength of 760 nm. Figure A.6 shows the field intensity at the opposite end of the rectangular structure, with clear edge enhancement, but also strongly confined light at the metal surface.

A.1.4 Sensing performance

A. Sensitivity calculations

To investigate the improved sensitivity of the resonant periodic structure supporting the SRSP, a 1 nm adlayer is applied on the top of the gold with refractive index 1.5. Figure A.7 shows the reflection for different angles of incidence, both for a 50 nm thick gold film and for the 10 nm thick periodic structure. In each figure, the reflection is

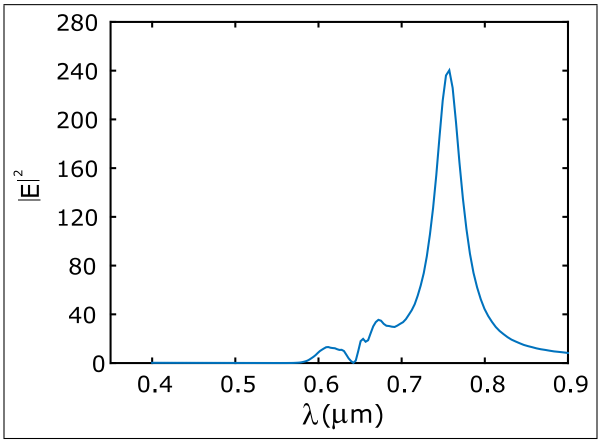

Figure A.5: Electric field intensity monitored near a 10 nm thick and 250 nm long rectangular gold structure on glass with a water surrounding. The peak in the LSP resonance is at 760 nm as desired for the SPR sensor configuration. Copyright ©2019, Journal of the Optical Society of America B

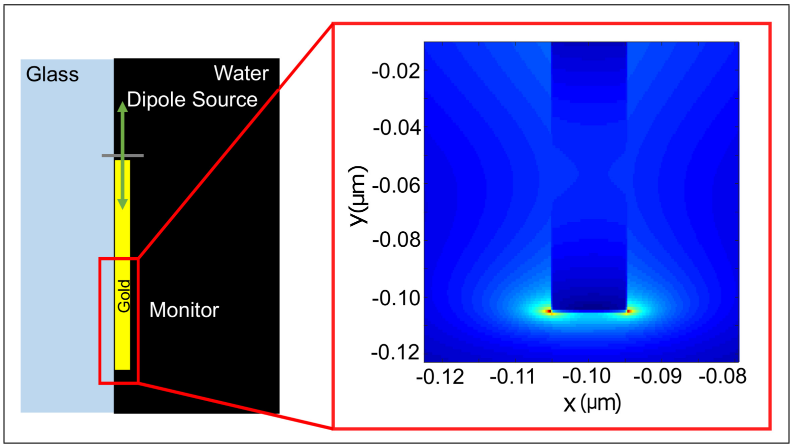

Figure A.6: The field intensity distribution at the LSP resonance. Copyright ©2019, Journal of the Optical Society of America B plotted for the bare structure and the structure with an adlayer. As demonstrated in the inset figures, the 10 nm gold periodic structure has 3.3 times higher sensitivity than for 50 nm continuous gold. (Note, that restricting the adlayer to the top surface is done for analytic simplicity, and may be achieved in practice by masking the sidewalls).

B. Resolution calculations

To compare the resolution of the gold film with the thickness of 50 nm and structured film with 10 nm thickness, we added shot noise to the digitized reflection. The digitization used 1024 bins for angle of incidence and 4096 bins for reflection intensity. We fit the noisy response to various adlayer index values (thickness 1 nm), and repeated the procedure to ensure a suitably averaged response. In this way, the resolution was determined to be 8×10^{-5} RIU/nm for 50 nm gold and 2×10^{-5} RIU/nm for 10 nm gold SRSP structure.

A.1.5 Discussion

It is clear from the analysis presented that the 10 nm thick gold film with a stripe grating structure has 3.3 times higher sensitivity and 4 times improved resolution.

Many have suggested that having a narrower peak will improve the performance of SPR detection systems because it allows for more precisely determining the position of the reflection dip. For this reason, a figure-of-merit of wavelength shift divided

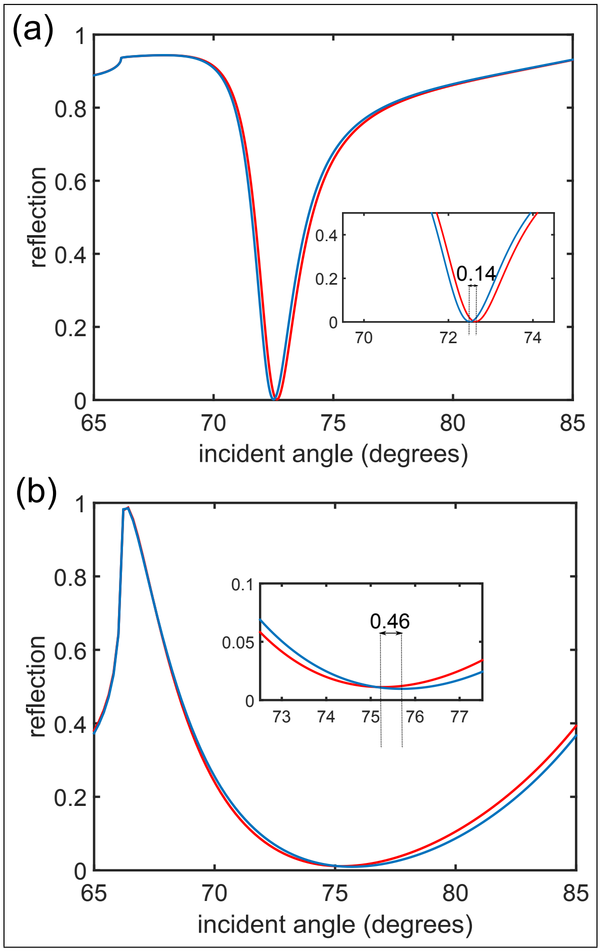

Figure A.7: Sensitivity calculations for (a) a 50 nm thick gold film with a 1 nm adlayer, and (b) a 10 nm thick gold film with 250 nm period and 210 nm length of each gold segment and a 1 nm adlayer. The insets are shown to clearly depict the angle shifts with the adlayer in each case. Blue line is related to the structure without adlayer and the red line is related to the structue with adlayer. Copyright ©2019, Journal of the Optical Society of America B by peak width is often used [94]. There are arguments to suggest that this is not always true. Consider the extreme case where the peak is much narrower than even one pixel spacing of the detector array, then there is no change in the signal detected for a sub-pixel sized shift with an adlayer. Therefore, having a very narrow peak can give no signal at all, even though the usual figure-of-merit is huge. Here, we have done the resolution calculations and found that the broader peak actually allows for improved resolution because the signal is supported by a greater number of bins (therefore, the noise in each bin can be averaged to reduce the overall noise). This noise analysis focuses on shot noise, where the noise is proportional to the square root of the detected counts. A well-engineered system will be shot noise limited [95]. Low cost fabrication of these grating structures is also an important consideration. We believe that these structures can be readily manufactured at low cost using existing template stripping approaches [96].

It is possible to push the sensitivity even higher by looking at ultra-thin gold films. While 10 nm continous gold films are commercially available, special methods can be used to create continuous films down to 5.4 nm that are stable under ambient conditions [97].

We are also aware of extremely high sensitivity demonstrations using nanorods (and similar works) [98]. While it is interesting to consider such approaches further, there are potential advantage of our design. We have already mentioned that our design is compatible with existing SPR machines, and may be readily mass produced using template stripping or other similar approaches. In addition, our design uses a mainly flat surface and so fouling that can occur with highly structured surfaces is not as big a concern.

A.1.6 Conclusion

In this work, we consider a perioidic SRSP sensor design that is compatible with existing commercial SPR sensors. The SRSP works by coupling to the LSP resonance of a rectangular structure. The design shows a 3.3 times higher surface sensitivity, which is promising for high-performance detection applications (such as low index contrast materials or sub-monolayer absorption). A noise analysis shows that the resolution also improves in the SRSP design.

A.1.7 Funding information

This work is supported by an NSERC Discovery Grant.

Appendix B

Accessible high-performance double nanohole tweezers [99].

Originally published:

Hajisalem G[1], Babaei E[1], Dobinson M, Iwamoto S, Sharifi Z, Eby J, Synakewicz M, Itzhaki LS, Gordon R. Accessible high-performance double nanohole tweezers. Optics Express. 2022 Jan 31;30(3):3760-9.

Reproduced with permission from Optics Express, The Optical Society of America.

---

[1] equal contribution

B.1 Accessible high-performance double nanohole tweezers

B.1.1 Abstract

Nanohole optical tweezers have been used by several groups to trap and analyze proteins. In this work, we demonstrate that it is possible to create high-performance double nanohole (DNH) substrates for trapping proteins without the need for any top-down approaches (such as electron microscopy or focused-ion beam milling). Using polarization analysis, we identify DNHs as well as determine their orientation and then use them for trapping. We are also able to identify other hole configurations, such as single, trimers and other clusters. We explore changing the substrate from glass to polyvinyl chloride to enhance trapping ability, showing 7 times lower minimum trapping power, which we believe is due to reduced surface repulsion. Finally, we present tape exfoliation as a means to expose DNHs without damaging sonication or chemical methods. Overall, these approaches make high quality optical trapping using DNH structures accessible to a broad scientific community.

B.1.2 Introduction

Nanohole optical tweezers have been broadly used to investigate nanoparticles, starting with early works on circular and rectangular apertures [100, 101, 28, 102, 103].

Double nanohole (DNH), coaxial and bowtie aperture and similar shaped aperture optical tweezers have been used in the analysis of particles smaller than 20 nm [28, 104, 105, 106, 107, 108, 109, 110, 111, 112, 113, 114, 115], including optical emitters and quantum emitters [116, 117, 118, 119, 120], magnetic particles [121], DNA [122], proteins [123, 36, 124, 125, 126, 63, 127]. These apertures have also been used in protein-DNA interactions [62], protein-small molecule interactions [128, 129, 36], protein-antibody interactions [130, 131], protein-protein interactions [32], and to study protein vibrations [66].

The benefit of using a DNH aperture is to have a high field enhancement localized in the gaps as small as 10 nm [32]. Most of these past works have used top-down methods, such as focused ion beam, to fabricate the apertures [62, 108]. Recently, we explored the use of colloidal lithography to create DNH apertures and used scanning electron microscope (SEM) to find them [44]. This still limits the use of the technique to those with SEM facilities, and introduces an extra registration step, where the SEM has to be compared with the microscope image using some fiduciary markers.

To make DNH aperture trapping more accessible, here we introduce a polarization and transmission dependence technique to localize DNHs on a substrate, as well as determine their orientation. We also characterize other aperture clusters and singles with this approach. We explore the use of low-repulsion substrates for improved trapping efficiency and tape-fabrication for gentle exposure of high-quality apertures.

B.1.3 Polarization dependent DNH localization and orientation

Figure B.1(a) shows a schematic of an optical tweezer setup, where a continuous wave (CW) diode laser beam was collimated, expanded, and focused through a 100× microscope objective (1.25 NA) into a nanoaperture. The transmitted signal was collected by a 10× microscope objective (0.25 NA) and measured by an avalanche photodiode (APD – Thorlabs, APD120A). The reflected laser beam and the transmitted LED light were directed to a charge-coupled device (CCD) camera. Fig. B.1(b) shows a CCD image of the aperture sample while the LED was on and the laser was off, and Fig. B.1(c) shows a CCD image of the sample while both the LED and laser were on and the laser beam was aligned and focused into an aperture.

Nanoapertures in gold on glass substrate were fabricated by using the colloidal lithography method [44]. Briefly, a 10 μL solution of 300 nm polystyrene nanospheres in ethanol was drop-coated on a glass microscope slide. Then, 5 nm titanium adhesion layer followed by a 70 nm gold film was deposited on the sample using a sputtering system (Mantis). The Au-Ti coated sample was sonicated for 5 minutes in ethanol to remove the polystyrene nanospheres and to reveal the nanoapertures on the film. Variations in the size of polystyrene spheres and the etching time results in varying of gap sizes and apertures diameters. Plasmonic nanoapertures on plastic substrate were fabricated following the the same process as described above but using polyvinyl chloride (PVC) slides instead of glass microscope slides (for SEM images see the Supplementary Material). Further, the omission of the sonication step in lieu of the tape-removal is discussed below.

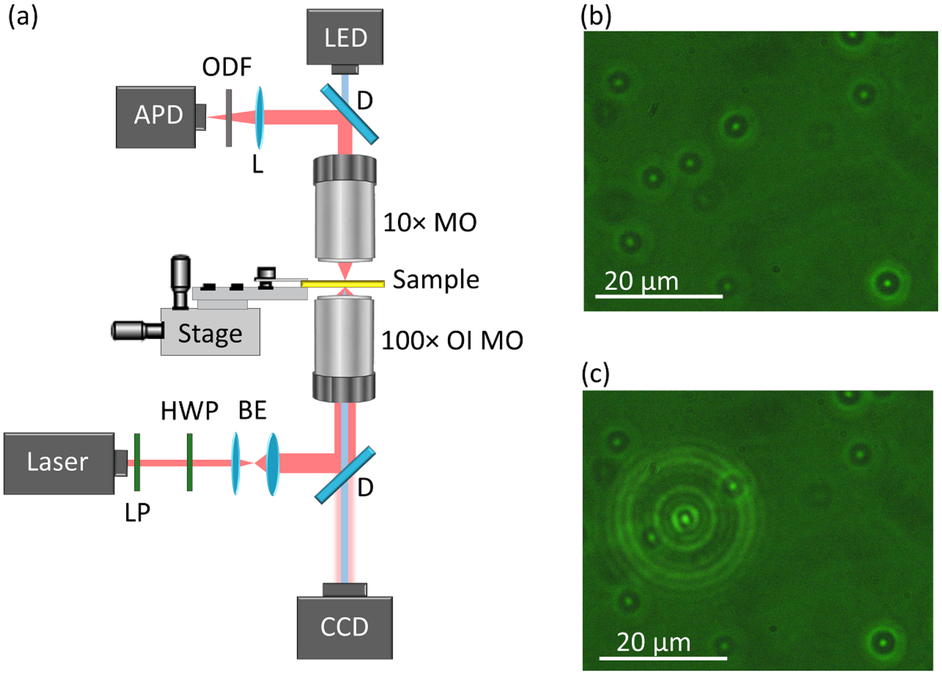

Figure B.1: Experimental optical trapping setup. (a) Schematic of an optical tweezer setup: linear polarizer (LP), half-wave plate (HWP), beam expander (BE), shortpass dichroic mirror (D), 100 × oil immersion microscope objective (100 × OI MO), piezo stage (stage), 10 ×microscope objective (10 ×MO), lens (L), optical density filter (ODF), and avalanche photodetector (APD). (b) A CCD image of a sample with nanoapertures when the LED light was on and the laser was off. (c) a CCD image of the sample when both the LED light and laser were on and the laser beam was focused into an nanoaperture. Transmitted LED light from nanoapertures varied for different shapes and resulted in varying of brightness of nanoapertures in the CCD image. Copyright ©2022, Optics Express

The colloidal lithography method resulted in formation of varying of nanohole configurations, i.e. single, double, and variable clusters nanoholes. In this method, dominant nanoapertures structures, average density of nanoapertures, diameter size of apertures and their separation gap size of DNHs on a sample were controlled through the fabrication process [44]. However, location and number of nanoapertures on a sample could not be controlled through the fabrication process (see the Supplementary Material) and this resulted in formation of varying of nanoaperture structures over the sample.

To find a DNH aperture, here we used a combination of CCD camera images and polarization dependent transmission of the laser beam, not only to align the laser beam with a nanoaperture, but also to distinguish between different nanoaperture structures on a sample. In addition, the transmitted LED light from nanoapertures varied for different nanoaperture structures, resulting in varying their brightness in the CCD image (see Figs. B.1(b) and (c)).

Figures B.2(a-d) show CCD images for varying of nanohole configurations and their transmitted signals (Figs. B.2(e-h)) measured in the APD. We can rapidly identify DNH candidates by the white light transmission imaged on the CCD. For example, Fig. B.2(a) shows a dimmer spot that was a single nanohole (determined later by SEM that is shown in the inset of the Fig. B.2(a)), whereas Fig. B.2(b) shows a brighter spot that was a DNH. By ignoring all the dimmest apertures, we can rule out single apertures. Fig. S2 of the Supplementary Material shows more details of

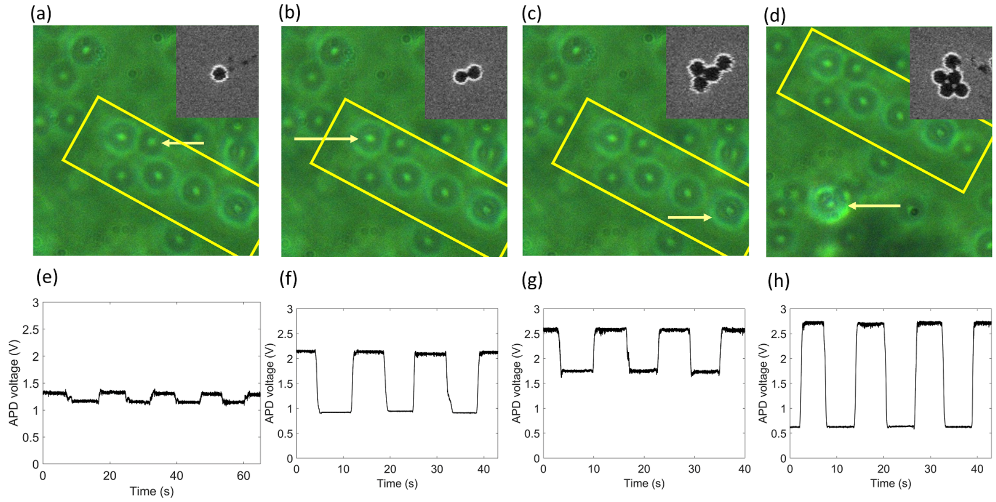

Figure B.2: Identifying DNHs and other nanohole configurations on a sample. (a-d) CCD images of white light transmission of single, double and varying of cluster apertures. In these images, the same area was artificially marked with yellow contours and an aperture of interest was shown with a yellow array. Brightness of apertures were varying depended on nanoholes configuration: (a) single nanoholes (SNHs) were the dimmest structures, (b) DNHs were brighter than SNHs but dimmer than clusters, (c and d) clusters were the brightest apertures among varying of configurations. Inset of figures (a-d) show SEM images of the marked nanoaperture (full SEM image is shown in the Supplementary Material. (e-h) Maximum and minimum polarization dependence of the laser transmission of an aperture of interest, marked in (a) to (d) and measured with the APD: (e) polarization dependence of the SNH shown in (a). (f) Polarization dependence of the DNH shown in (b). (g and h) polarization dependence of the clusters shown in (c) and (d), respectively. The HWP was switched between maximum and minimum transmission values in the plots (e-h). Copyright ©2022, Optics Express

identifying DNH by using CCD images and changing the distance of the focusing microscope objective to the substrate. Next we use polarization dependence of the laser transmission. DNH and clusters show a polarization dependence (generally) as shown in Figs. B.2(f-h). The small polarization dependence of the single nanohole is a combination of slight anisotropy and some polarization in the optics setup. Among Figs. B.2(f-h), the DNH could be reliably found by the polarization dependence and intensity. It should be noted that the HWP was switched between maximum and minimum transmission values in these plots.

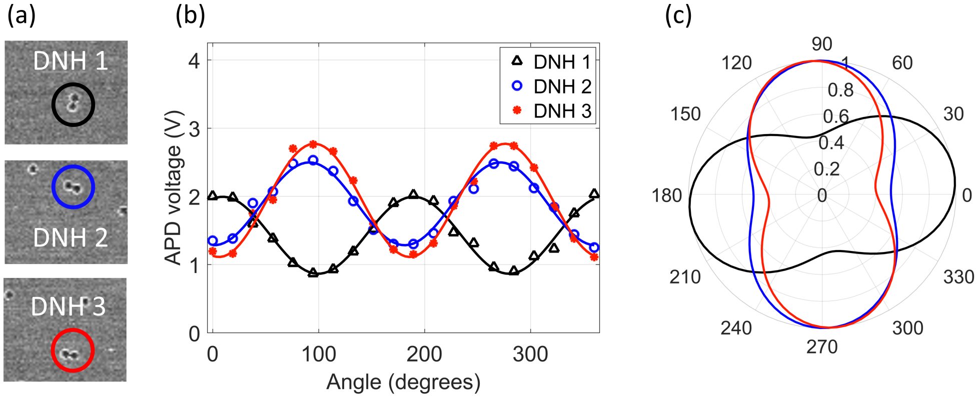

Figure B.3: Polarization dependence of the laser transmission of DNHs. (a) SEM images of DNHs with their axes normal or parallel in respect to each other. Full SEM image is shown in the Supplementary Material. (b) Parallel DNHs show similar polarization dependence of the laser transmission, and DNHs with normal axes in respect to each other show opposite transmission response of the laser beam. The laser polarization direction was rotated by using a HWP in front of the lasrt output, starting from the zero-order line of the HWP. (c) Polar plots of normalized transmissions for DNHs shown in (a and b). Copyright ©2022, Optics Express

Figure B.3 shows that the orientation of the DNHs could be determined by the detailed polarization analysis. Maximum transmission through a DNH occurs when the laser polarization is along the short axis of the DNH. In these measurements, the polarization direction of the laser beam was rotated in steps by a HWP in front of the laser, starting from the zero-order line of the HWP. The transmitted signal through an aperture was measured by the APD. Figs. B.3(a) shows SEM images of three DNHs with parallel or normal orientations in respect to each other (the full SEM image is shown in the Supplementary Material). We observed that DNHs with parallel axes had similar polarization responses, while DNHs oriented normal in respect to each others showed orthogonal polarization response (Fig. B.3(b)). Fig. B.3(c) shows polar plots of normalized polarization dependence of the DNHs in (a) and (b). Normalized transmission in the polar plots was obtained by dividing transmission values by the maximum transmission value.

Figures B.4 and B.5 show that this applies to triangular (three holes) and diamond (4 holes) clusters as well. These apertures could also be located and oriented.

Figure B.4 shows the polarization dependence of the transmission laser beam through two triangular clusters with different orientations. Fig. B.4(a) shows SEM images of the triangular apertures and Figs. B.4(b) and (c) show the transmitted signals and the normalized polar plots of the transmitted signals through the triangular apertures shown in (a). We also trapped 20 nm polystyrene nanospheres by using triangular apertures showing similar behavior as DNHs (see the Supplementary Material).

Figure B.5(a) shows SEM images of two diamond configurations clusters with

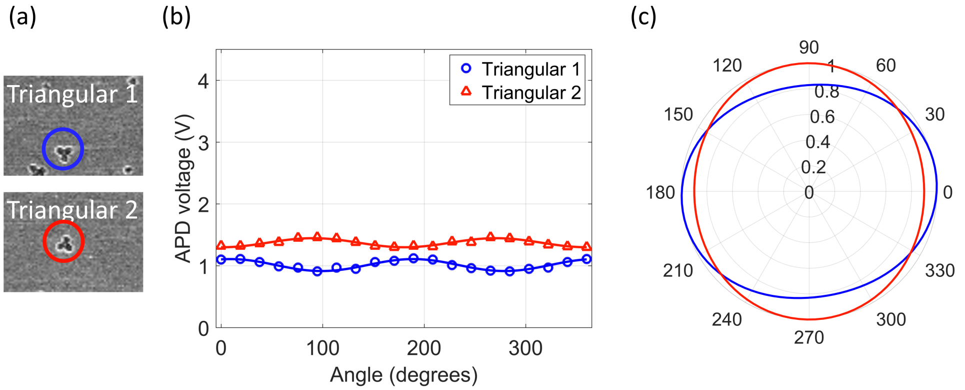

Figure B.4: Polarization dependence of triangular clusters with different orientation. (a) SEM images of two triangular clusters (labeled as Triangular 1 and Triangular 2) on a sample. (b) Polarization dependence of transmission through the aperture was obtained by rotating the HWP in front of the laser and measured the transmission signal in the APD. (c) Polar plot of the normalized transmission signals shown in (b). Copyright ©2022, Optics Express

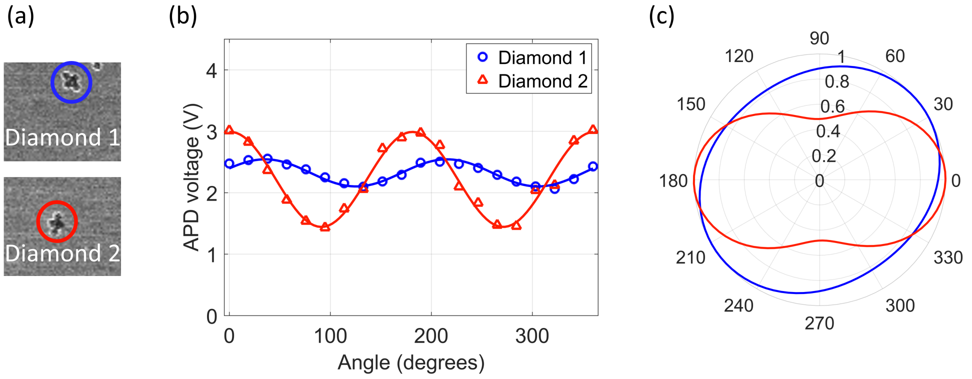

Figure B.5: Polarization dependent response of two clusters with diamond configuration on a sample. (a) SEM images diamond apertures (also see the Supplementary Material), marked with yellow contours. (b) Polarization dependence of the transmission laser beam of the diamond apertures shown on (a). (c) Polar plots of normalized transmission of (b). Copyright ©2022, Optics Express different orientations in respect to each other. Figs. B.5(b and c) show the polarization dependence and normalized polarization dependence of the transmission signals through the apertures. These show that diamond clusters had polarization dependence while they had higher transmission that DNHs.

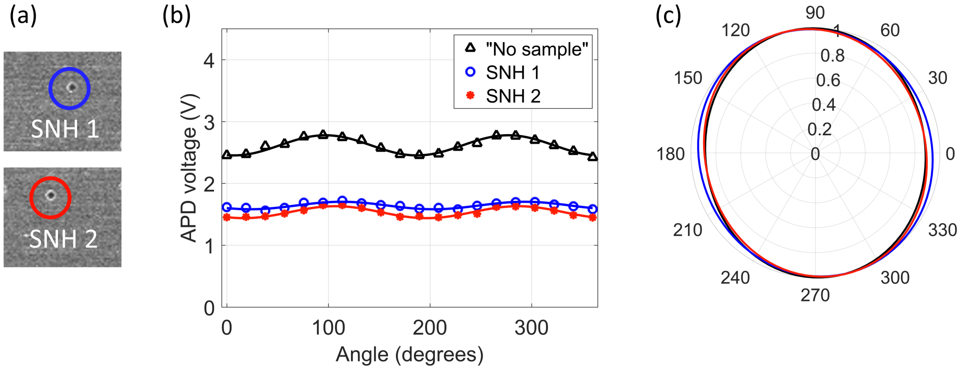

Figure B.6: Polarization dependent response of SNHs and polarization rotation of the laser beam without any sample (labeled as ”No sample”. SNHs showed the same polarization responses and also the same response as the laser beam without any sample. We believe this mainly comes from the polarization dependence of the setup. Copyright ©2022, Optics Express

Figure B.6 shows that a SNH show a slight polarization dependence but these are all the same and also the same as not having any sample there (labeled as “No sample”). Therefore, we believe this is mainly coming from the polarization dependence of the setup.

B.1.4 Improved trapping by substrate modification

Figure B.7 shows trapping events of 20 nm polystyrene nanospheres with a DNH in gold on glass substrate (Fig. B.7(a)) and with a DNH in gold on a PVC plastic substrate (Fig. B.7(b)). We used DNHs with similar gap size of ∼50 nm and aperture diameter of ∼215 nm in 70 nm gold film on glass and plastic substrates (SEM images are shown in the Supplementary Material). Trapping a particle in a DNH aperture resulted in increasing the transmission, observed by a jump of in the APD signal. Additionally, when particles were trapped the level of noise also increased. For trapping measurements of > 5 samples for each glass and plastic substrates, trapping on glass substrate showed on average a 5% jump of the APD signal, whereas trapping on plastic substrate showed on average a 10% jump in transmission signal, suggesting that the particle was positioned closer to the maximum intensity of the beam, causing increased light transmission through the aperture. Furthermore, the level of noise for the plastic trapping was less than that of the glass trapping indicating that there was less movement of the particle, and that trapping with a plastic substrate was more stable than with glass. Also, we observed that the initial laser power required to trap polystyrene with glass substrate was ∼5.8 mW, while for the plastic the initial required power was ∼1.4 mW.

Figure B.8 shows the mean APD voltage of trapping events for varying the incident laser power, along with the level of noise characterized by the standard deviation

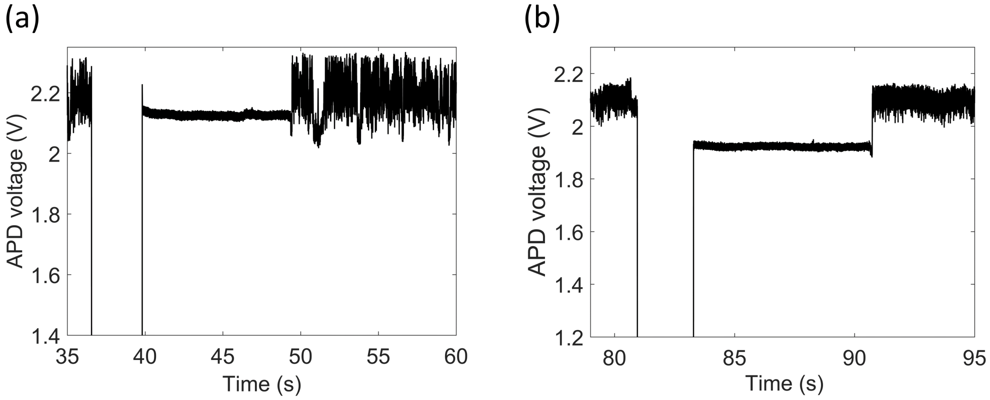

Figure B.7: Trapping event of 20 nm polystyrene (a) with a DNH in gold on a glass substrate, and (b) with a DNH in gold on a PVC plastic substrate. Copyright ©2022, Optics Express

(STDev), for glass and plastic substrates. With the plastic substrate, it was possible to keep a 20 nm polystyrene in trapping for laser powers as low as ∼0.6 mW, whereas for the glass substrate the minimum laser power needed to keep the particle in trapping was ∼4.2 mW. Fig. S7 of the Supplementary Material shows the transmission measurement data. This shows changing the substrate from glass to plastic reduced the minimum trapping power by 7 times and improved the trapping ability, which we believe is due to reduced surface repulsion because a glass substrate will charge strongly in water [41, 132, 133]. Since glass is much more hydrophilic than PVC plastic [134], glass ionizes easily in water[41], which increases the bulk concentration of ions surrounding the glass surface, contributing to a stronger repulsion force [135, 136].

While we primarily show data for trapping polystyrene nanospheres, we also trapped PR65 proteins (see the Supplementary Material) [137].

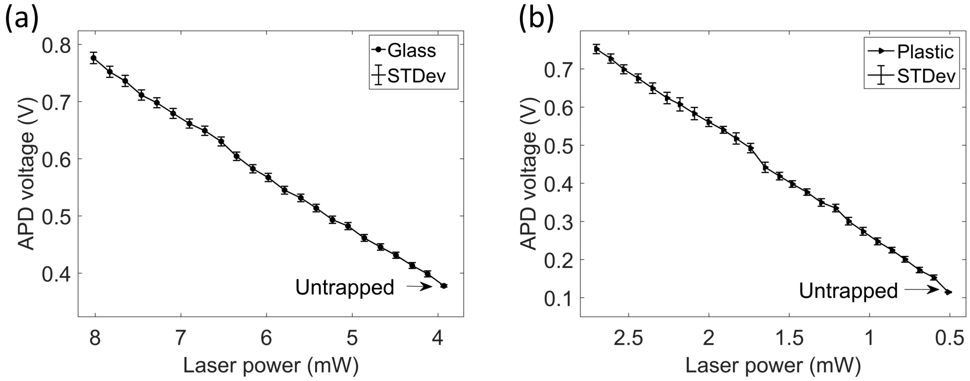

Figure B.8: The mean APD voltage of trapping 20 nm polystyrene for varying the incident laser powers. (a) Trapping with a DNH in gold on a glass substrate, and (b) trapping with a DNH in gold on a plastic substrate, with the STDev indicating the width of the trapping signal. Each measurement was conducted by decreasing the incident laser power while the particle was still trapped. The incident laser power was decreased until it was too low to keep the particle in trapping site and particle was released. Copyright ©2022, Optics Express

B.1.5 Tape exfoliation

Figure B.9 shows the fabrication process of DNH apertures using the colloidal lithography [44] by using the tape-removal of nanoparticles instead of the sonication step. The original colloidal lithography method used sonication to remove the polystyrene nanospheres, but it was common for the metal film to begin to detach from the surface before all the nanospheres are removed. Here we used Scotch tape to fully exfoliate the polystyrene nanospheres without damaging the gold surface. In this method, tape

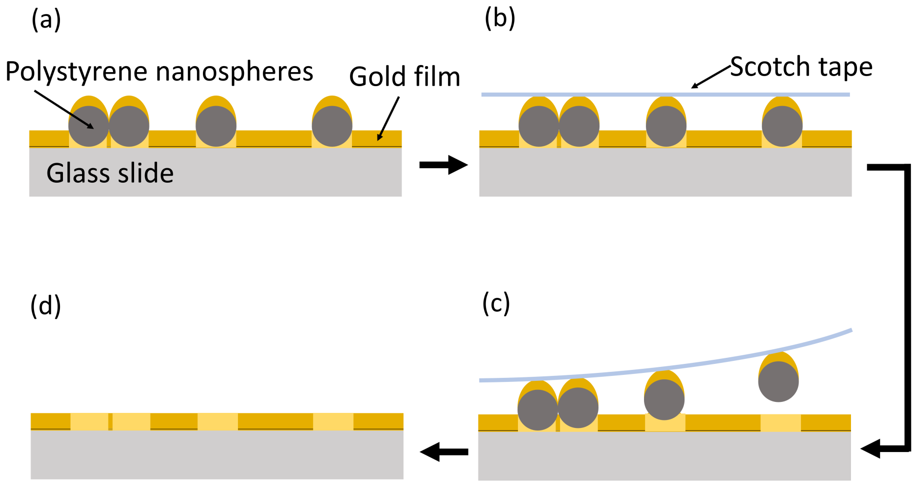

Figure B.9: An illustration of fabrication process using tape exfoliation to remove nanospheres and reveal apertures: (a) a titanium adhesion layer following by a gold film was deposited on top of polystyrene nanospheres on a glass substrate, (b) a tape was applied to a small area on the surface, (c) the tape was gently removed from the sample resulted in pulling away the polystyrene nanospheres, and (d) revealing the nanoapertures on the gold film. Copyright ©2022, Optics Express

was applied to a small area on the surface and then gently removed to pull away the polystyrene spheres, this step was repeated until the desired area has been exfoliated, taking care not to cover the same area multiple times. This was then followed by washing in ethanol. Care was taken to apply the tape to a sufficiently small area to reduce the chance of adhering to the gold. Figure B.10 shows SEM images of the apertures fabricated by using the tape exfoliation process. Here the nanoparticles were reliably removed, revealing high quality apertures without damage that can come from sonication or using chemicals.

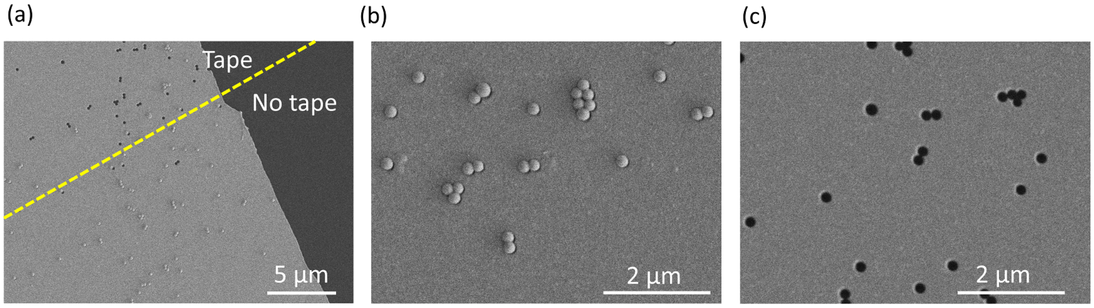

Figure B.10: Nanopaertures fabricated by tep-removal method. (a) An SEM image of an area on the surface where a tape exfoliation was applied and an area without applying the tape. (b) An SEM image of the surface before the tap-removal, and (c) an SEM image of the surface where the tape exfoliation was applied. Copyright ©2022, Optics Express

B.1.6 Conclusion

We have demonstrated a way to identify the location and orientation of DNHs in-situ, without the need for SEM or other complicated processes. This makes the approach much more accessible without ready access to such facilities, requiring only the use of an evaporator, as well as eliminating time-consuming characterization and registration steps.

We have also improved the trapping by switching the substrate from glass to PVC, which reduces repulsion in aqueous environments and reduces the minimum trapping power by 7 times. A further improvement in the aperture quality is obtained by using tape exfoliation instead of sonication in ethanol.

We believe that this low-cost and high-quality approach to DNH trapping will enable greater adoption of the technique by the biophysics and quantum emitter communities. In biophysics, the emphasis can be shifted to protein characterization and interactions studies rather than fabrication and characterization of apertures.

B.1.7 Backmatter

Funding

The authors acknowledge funding from the Natural Sciences and Engineering Research Council of Canada (NSERC) RGPIN-2017-03830. GH and EB were supported by the Human Frontier Science Program (HFSP) RGP0027/2020-ITZHAKI grant.

Acknowledgments

The authors acknowledge use of facilities of the Centre for Advanced Materials and Related Technologies (CAMTEC).

Disclosures

The authors declare no conflicts of interest.

Data availability statement

Data underlying the results presented in this paper are not publicly available at this time but may be obtained from the authors upon reasonable request.

Supplementary document

See Supplement 1 for supporting content.

B.2 Supplementary material: Accessible high-performance double nanohole tweezers

Scanning electron microscopy (SEM) was used to characterize the structures analyzed in this work and provide a reference for constellation mapping of the sample when observed in the CCD camera. Figure B.11 shows an SEM image and a CCD image of the sample shown in the Figure B.2 of the main text.

Figure B.11 shows an SEM image of a sample and three CCD images of the same sample with three distances of the 100× microscope objective from the surface of the sample, which revealed varying of brightness of apertures for varying nanohole configurations. The bright area in the CCD image is a scratch in the gold layer that serves as a fiducial marking for finding the corresponding location in the trapping setup.

Figure B.12 shows several of the structures analyzed in the main text. The structure of each aperture was confirmed using the SEM images.

Figure B.13 shows the transmission simulation for varying the polarization angle of the incident beam for a triangular structure, obtained by finite-difference time-domain (FDTD) method (Ansys Lumerical 2020 R2.3) at 973 nm wavelength, confirming that the transmission shows negligible polarization dependence. A triangular aperture

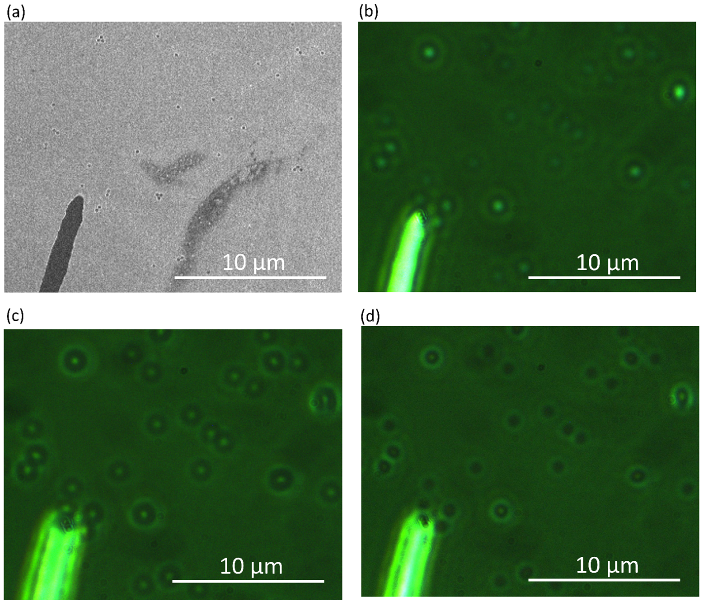

Figure B.11: Distinguishing between varying of apertures by varying the distance of the 100× focusing microscope objective from the surface of a sample. (a) An SEM image of the sample with an scratch marker on it. (b-d) CCD images of the same sample with the microscope objective adjusted (b) focused on the cover glass, (c) focused on top of apertures, (d) focused at bottom of apertures. Changing the distance between the sample and the microscope objective were used to show variation of the brightness different apertures. Copyright ©2022, Optics Express

with 70 nm gap size and 280 nm aperture diameter in a 70 nm gold film was simulated with the same dimensions as Triangular 1 in the Figure 4 of the main text. The refractive index of gold was chosen as Au (Gold) – Palik [138]. A layer of water (H_2O (Water) – Palik) with 200 nm thickness was placed above the gold layer. Also the triangular aperture material was selected as water similar to experiments. A glass (SiO_2 (Glass) – Palik) substrate was created with the thickness of 2 μm and lateral dimensions of 2.8 μm × 2.8 μm, the same lateral dimensions as the gold

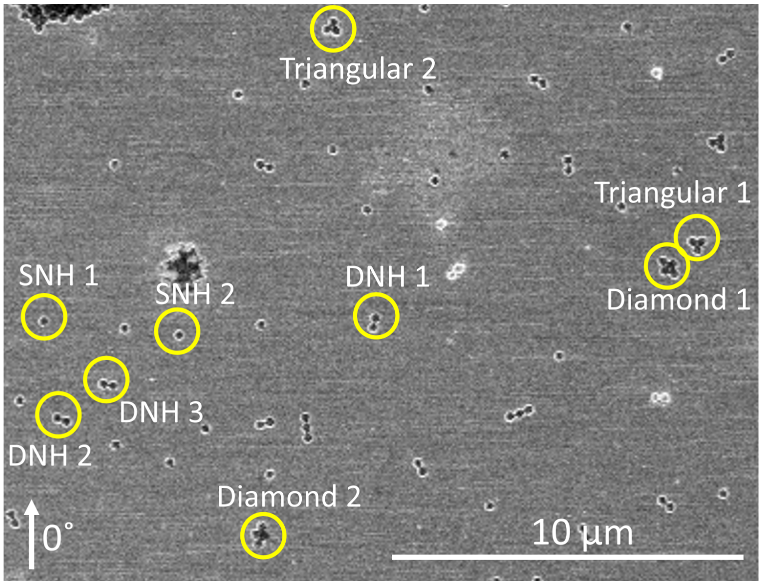

Figure B.12: SEM image of the sample used in the measurements shown in Figures 3-6 of the main text. Labels are the same as used on the main text. Copyright ©2022, Optics Express

and glass layers. For the FDTD simulations, we used the following parameters: the simulation volume had dimensions of 1.3 μm × 1.3 μm × 170 nm in the x, y and z directions. A uniform mesh of 5 nm was used. Perfectly matched layers were used on all boundaries. A total-field scattered-field (TFSF) source with 800 to 1200 nm wavelength range was used. The TFSF region dimensions in x, y and z directions were 800 nm × 800 nm × 110 nm and the source was placed 30 nm above the gold film. To obtain the polarization dependence of the transmission, a frequency-domain field and power monitor was placed 10 nm above the gold film. Transmission at 973 nm was recorded for varying of the polarization angles of the source from 0° to 90°. Insets show the electric field distribution of the triangular structure for 0°, 45°,

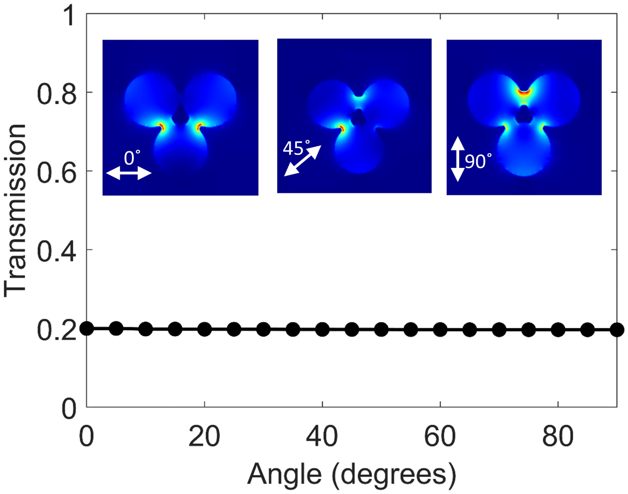

Figure B.13: The transmission for varying the polarization angle of the incident beam for a triangular structure, obtained by FDTD simulations. The triangular structure showed negligible polarization dependence. Insets show the electric field distribution of the triangular structure for 0°, 45°, and 90° directions of the incident electric field. Triangle nanostructure was simulated with the same dimensions as Triangular 1 in the Figure 4 of the main text. Copyright ©2022, Optics Express

and 90° polarization angles of source, measured with a frequency-domain field and power monitor which was placed in the middle of the gold film.

Trapping is typically performed on DNH structures, but other structures are capable of trapping. Figure B.14 shows a trapping event of a 20 nm polystyrene sphere using a triangular-shaped aperture.

Figure B.15 shows close-up SEM images of DNHs created using the colloidal lithography method on glass and plastic substrates.

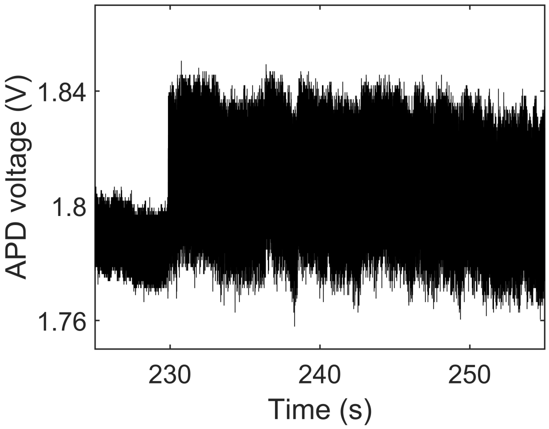

Figure B.14: Trapping event of a 20 nm polystyrene with the Triangular 1 (the SEM is shown in Fig. B.12 with the incident laser power of 10 mW. Copyright ©2022, Optics Express

As a proof of concept for the common application of protein trapping, the DNH structures found using the characterization approach presented in the main text were used to trap the PR65 protein. Figure B.16 shows a trapping event of a PR65 protein with a glass and with a plastic substrate.

Figure B.17 shows the transmitted laser signal for the data provided in the Figure B.8 of the main text. The APD voltage was measured for varying of the incident laser power while a polystyrene nanosphere was trapped with a DNH on the glass

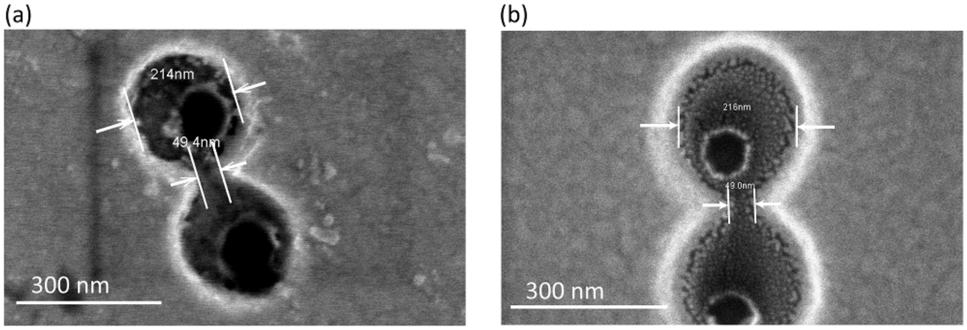

Figure B.15: An SEM image of a DNH in gold on a glass substrate, and (b) an SEM image of a DNH in gold on a plastic substrate. DNHs on both had aperture size of ∼215 nm and gap size of ∼50 nm, and they were fabricated by colloidal lithography method in a 70 nm gold film on top of a glass or plastic substrate, respectively. Copyright ©2022, Optics Express

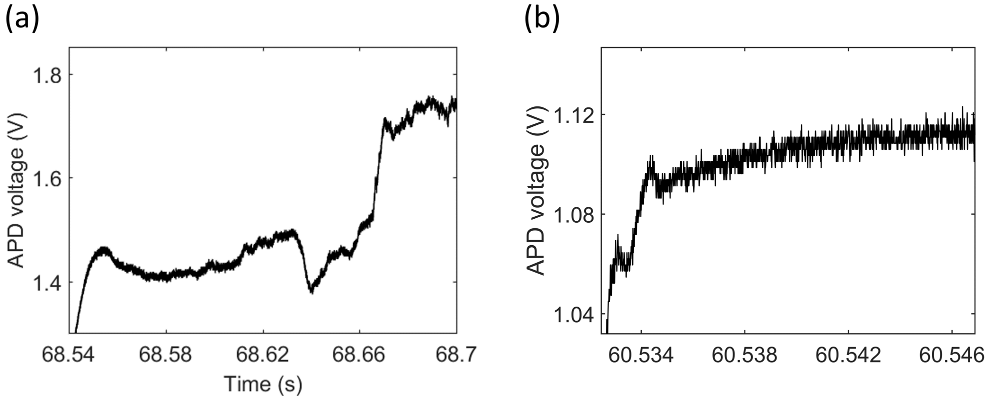

Figure B.16: Trapping a PR65 protein with glass and plastic substrates. (a) Trapping with a DNH on a glass substrate, and (b) trapping with a DNH on a plastic substrate. Copyright ©2022, Optics Express

substrate (Fig. B.17(a)) and a DNH on the plastic substrate (Fig. B.17(b)).

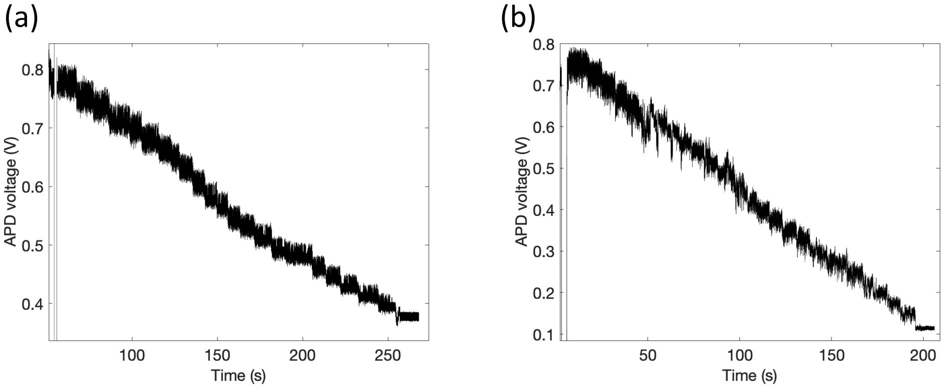

Figure B.17: The transmitted voltage measured in the APD for trapping events of polystyrene nanospheres with plasmonic DNHs on a glass and a plastic substrates for varying the incident laser power, while the polystyrene nanosphere was still trapped. Copyright ©2022, Optics Express

Appendix C

Fringe dielectrophoresis nanoaperture optical trapping with order of magnitude speed-up for unmodified proteins [139]

Babaei E, Wright D, Gordon R. Fringe dielectrophoresis nanoaperture optical trapping with order of magnitude speed-up for unmodified proteins. Nano Letters. 2023 Mar 31;23(7):2877-82.

Reproduced with permission from Nano Letters, ACS Publication.

C.1 Fringe dielectrophoresis nanoaperture optical trapping with order of magnitude speed-up for unmodified proteins

C.1.1 Abstract

Single molecule analysis of proteins in an aqueous environment without modification (e.g., labels or tethers) elucidates their biophysics and interactions relevant to drug discovery. By combining fringe-field dielectrophoresis with nanoaperture optical tweezers we demonstrate an order of magnitude faster time-to-trap for proteins when the counter electrode is outside of the solution. When the counter electrode is inside the solution (the more common configuration found in the literature), electrophoresis speeds up the trapping of polystyrene nanospheres, but this was not effective for proteins in general. Since time-to-trap is critical for high-thoughput analysis, these findings are a major advancement to the nanoaperture optical trapping technique for protein analysis.

C.1.2 Paper content

Single-molecule techniques can resolve heterogeneity in behavior and give access to kinetics without synchronization [49]. Ideally these methods would allow for seeing dynamics at a rapid timescale without modifications to the protein, in a physiological environment and be able to study small and large biomolecules. While used extensively in free-solution studies, modifications like labelling and tethering disrupt the natural function of biomolecules with significant impact on properties such as diffusion, surface potential and binding kinetics. [50]

Various single molecule techniques allow for analyzing unmodified proteins in aqueous environments, including nanopores, iScat and nanoaperture optical tweezers (NOTs). NEOtrap is a nanopore technique that sizes proteins by monitoring changes in ionic current for a blocked nanopore [140], and it has recently been used to achieve sizing of 14 kDa proteins [51]. Early works on iScat achieved a 40 kDa size limit of detection, [52] which can be further enhanced below 9 kDa by using sophisticated machine learning techniques [53]. NOTs have previously sized single proteins down to 6.5 kDa, even in heterogeneous unprocessed solutions [35, 125]. More generally, various shaped apertures have been used to trap and analyze nanoparticles [100, 32, 28, 106, 105, 141, 142, 143, 130, 119, 109, 144, 145, 126, 108, 115, 114, 141, 146, 147, 104, 148].

Later works combined nanopores with NOTs, which confirms that single proteins were trapped in NOTs, as generally expected due to natural repulsion [126, 130, 128]. Even without nanopores, the normal single protein analysis of NOTs is clear from the uniform distinct steps observed with rare multiple-trapping events [149] and from the consistent single-particle mass sizing results [35]. While trapped, single protein dynamics have been observed, including conformational changes (giving information about protein shape) and enzyme action [125, 150].

Previous works have introduced electric fields with nanoapertures in metal films to manipulate nanoparticles. By applying an AC electric field for a counter electrode in solution, as well as a laser beam, a balance was achieved between electroosmotic and thermophoretic forces to trap fluorescently labelled proteins at a distance from an array of holes [45]. Dielectrophoresis has also been used with gold-coated nanopipettes to isolate individual fluorescently labelled DNA where the counter electrode was again placed in solution [46]. Similarly, dielectrophoresis was used to enhance surface trapping and sensing of proteins and polystyrene particles with a nanohole array in a metal film. [47] There are two main distinctions between these (and similar) past works and our present work: we are applying the use of electrodes to NOTs for the first time without the use of fluorescence, and we are changing the placement of the counter electrode to create a fringe field and thereby enhance performance.

Here we examine the use of a electrode for enhancing the trapping speed of a NOT for unlabelled proteins. When the counter electrode is placed on the dielectric substrate supporting the gold film (on the opposite side from the solution), so that a fringe field is created in the solution by the nanohole, an order of magnitude reduction in trapping time is achieved. This occurs for both negative and positive applied voltage (and AC voltage) demonstrating that the speedup comes from dielectrophoresis. When the counter electrode is placed in the solution, which is the more common practice, a positive voltage on the gold film with respect to the counter electrode speeds up the trapping of polystyrene nanospheres, but this was not generally effective for proteins.

Figure C.1(a) shows a schematic of the optical tweezer system containing a gold film with double nanoholes, fabricated as described previously [44, 99]. Nanohole film samples were prepared in gold on glass as in a past work [99]. The dimensions were 20 nm for the cusp size and 330 nm for the diameter. A typical electron micrograph of the sample is shown in the Supporting Information Figure C.5. The sample was cleaned with acetone between runs. After a few runs, samples were cleaned with KOH and H_2O_2 solution. The optical tweezer setup was modified from Thorlabs OTKB by replacing the 980 nm laser diode with an 850 nm laser diode. The laser power was maintained at 16 mW.

A counter electrode is placed on the opposite side of the glass substrate to the sensing volume (away from protein solution) to achieve a fringe field through the aperture, as shown schematically in Figures C.1 (b) and (c). The fringe field can attract particles in the solution by dielectrophoresis. We have confirmed that the intensity field gradient increases towards the aperture for the counter electrode above the glass as shown by finite element method simulations (as shown in Supporting Information Figure C.12 and C.13), which is schematically represented in Figure C.1(c). If the counter electrode is placed in solution, the opposite gradient appears (also shown in Supporting Information Figure C.14 and C.15).

Figure C.2 shows a typical trapping event for the protein aprotinin (6.5 kDa). The

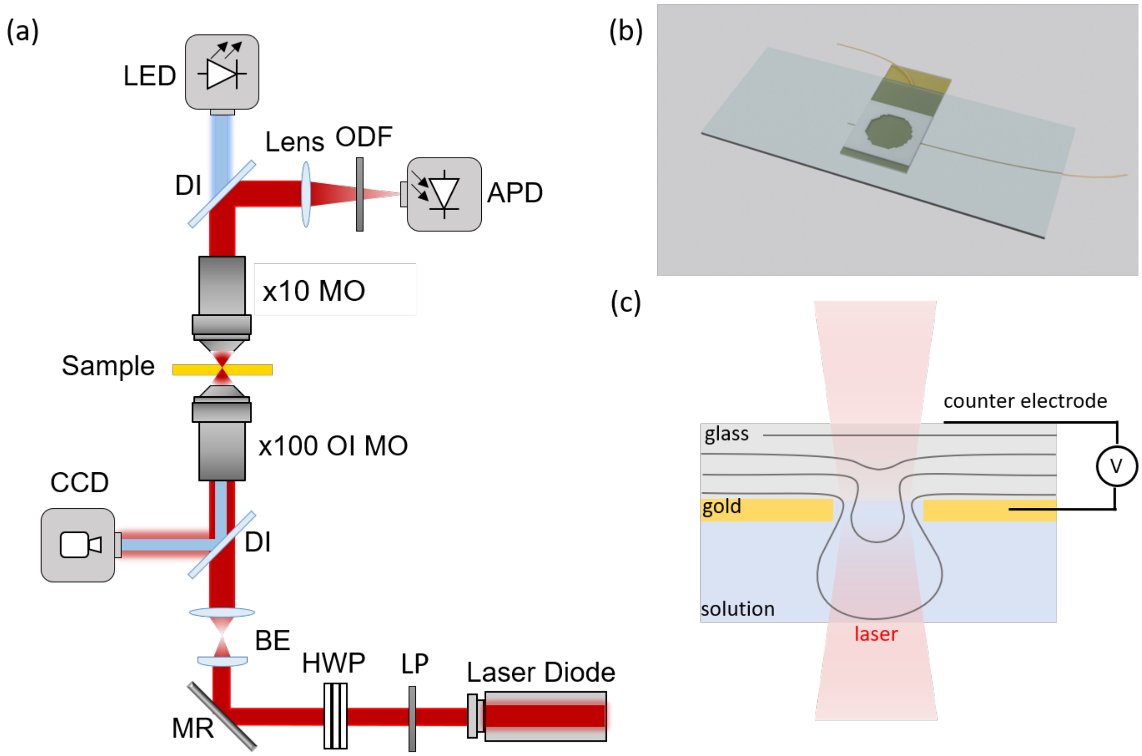

Figure C.1: Dielectrophoretic double nanohole trapping. (a) Schematic of optical setup. APD: Avalanche Photodiode, ODF: Optical Density Filter, OI: Oil Immersion, MO: Microscope Objective, CCD: Charge Coupled Device, DI: Dichroic, BE: Beam Expander, HWP: Half-Wave Plate, LP: Linear Polarizer, MR: Mirror. (b) Schematic of microwell sample with electrode placement. (c) Side view of electrode connections and equipotential lines of fringe electric fields around nanoaperture. Copyright ©2023 American Chemical Society laser is turned on at 2.5 seconds and then 42 seconds elapses before there is a rapid discontinuity in the signal (trapping) and a large increase in noise (protein undergoing Brownian motion in the trap). The elapsed time is called the time-to-trap, T.

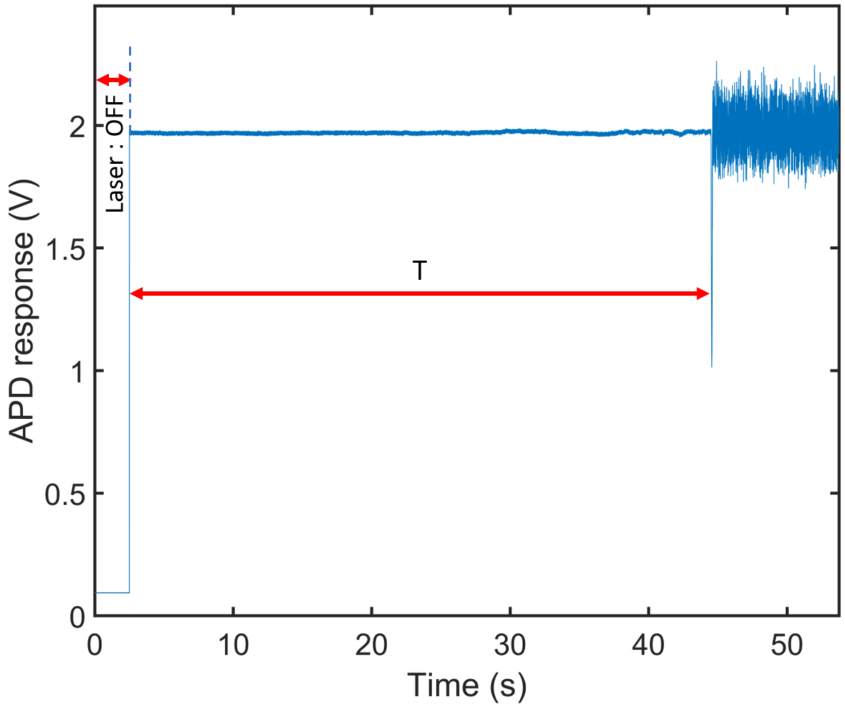

Figure C.2: Time-to-trap (T) in a typical protein trapping event of aprotinin. Copyright ©2023 American Chemical Society

We performed trapping measurements for several proteins in three experiments: with no voltage applied, with DC voltage applied, and with AC voltage applied. Cytochrome c, bovine serum albumin, β amylase were from the GE LMW filtration calibration kit (GE28-4038-41, Sigma Aldrich), and ovalbumin, conalbumin, aprotinin, carbonic anhydrase, ribonuclease were from Cytovia. The concentration of 0.1 percent weight per volume was used for all the proteins in 0.01 M phosphate buffer.

Figure C.3(a) summarizes the results. Applying a DC voltage reduced the time-to-trap substantially (between 3 and 11 times). The results were repeated between 3 and 10 times for each protein and the mean value is reported in the figure.

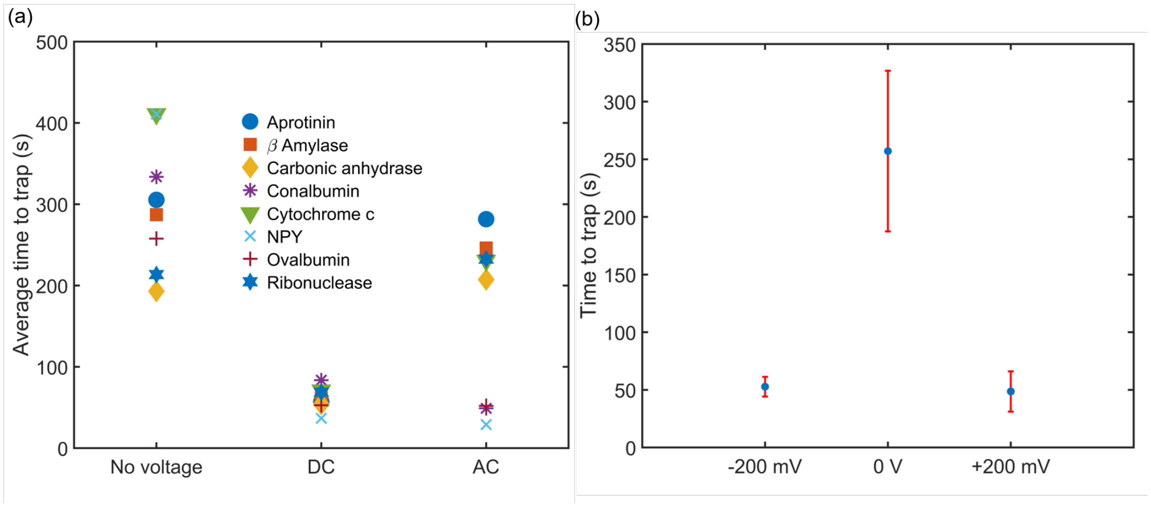

Figure C.3: (a) Average time-to-trap vs. applied DC and AC voltages for different proteins. (b) Trapping time for ovalbumin trapped applied DC voltage with dielectrophoresis method. Copyright ©2023 American Chemical Society

We also experimented with applying an AC voltage, with frequencies between 10 Hz and 1 kHz. Based on these initial studies, we selected 100 Hz for AC trapping; however, the speed-up was not as consistent with AC fields as for DC. While either AC or DC voltages can result in a speed-up for trapping, we have not found a correlation between this effect and protein charge (zeta potential, see Supporting Information Table 1), highlighting that dielectrophoresis, a particle polarization effect, is likely to be the dominant mechanism. A different version of Figure C.3(a) is given in the Supporting Information Figure C.18, which shows the error bars representing the standard deviation over multiple measurements.

Figure C.3(b) shows that the polarity of the DC field did not impact the time-to-trap, which distinguishes dielectrophoretic from electrophoretic effects. Since the speed-up was agnostic to sign, the observed trapping is dielectrophoretic in nature.

After trapping a particle with both voltage and laser on, we found that the particle remained in the trap if the voltage was turned off. We also turned the voltage on prior to turning on the trapping laser. This led to a small speed up on the time to trap, but not appreciable. The voltage was not sufficient to trap the particle without the laser.

We also placed the counter electrode inside the solution, as shown schematically in Figure C.4(b). This is expected to have two effects: first, the fringe field should have a negative gradient towards the nanoaperture [151] (decreasing field strength when approaching the aperture) and second, any surface-charge electrostatic interaction can be offset by the applied field. The difference between the two configurations is the gradient of the fringe field. In one case it is increasing towards the aperture and in the other it is decreasing towards the aperture, as shown in COMSOL simulations in the Supporting Information Figure C.12, C.13, C.14 and C.15. The electrode-aperture distance was similar in both configurations of the order of 1 mm. The height of the channel was 100 microns, but the electrode was offset laterally in both cases by a comparable amount. We found that having the counter electrode inside the solution did not speed up trapping for proteins in general (see Supporting Information

Figure C.11); however, it did reduce the time-to-trap for 20 nm polystyrene spheres systematically. Furthermore, applying a greater positive potential to the gold film systematically reduced the time-to-trap, but a negative voltage did not allow for stable trapping, as shown in Figure C.4(d). This suggests that an electrostatic interaction was attracting the negatively charged polystyrene particles to the surface to enhance trapping speed. We believe that the electrostatic effect is more pronounced for the polystyrene particles because they are significantly larger (typical protein size is a few nm), and therefore there is more effect from the surface charge.

Considering diffusion alone, we expect that the time-to-trap would be less than a millisecond, assuming diffusion coefficient of around 100 μ^2/s and average spacing of 0.1 μm (typical at micromolar concentrations). But this is not what is seen in NOTs: in the best case, trapping usually takes minutes, and in some extreme cases, tens of minutes [123]. In some cases, it can be faster (10s of seconds for 20 nm polystyrene nanospheres) [150]. This can also be sped up by using surfactants to modify the Soret coefficient and then attract particles to the trap [108]. However, surfactants can have a damaging effect on proteins [152].

Trapping is slow because of competing effects that can keep the nanoparticles away from the trapping site. These effects include electrostatic repulsion and thermophobicity (when the trapping site at higher temperature due to the laser). Nanopores have been used to direct biomolecules to the trapping site with electrophoresis [126, 128]. While this allows for rapid trapping, it requires: fabrication of a nanopore in addition

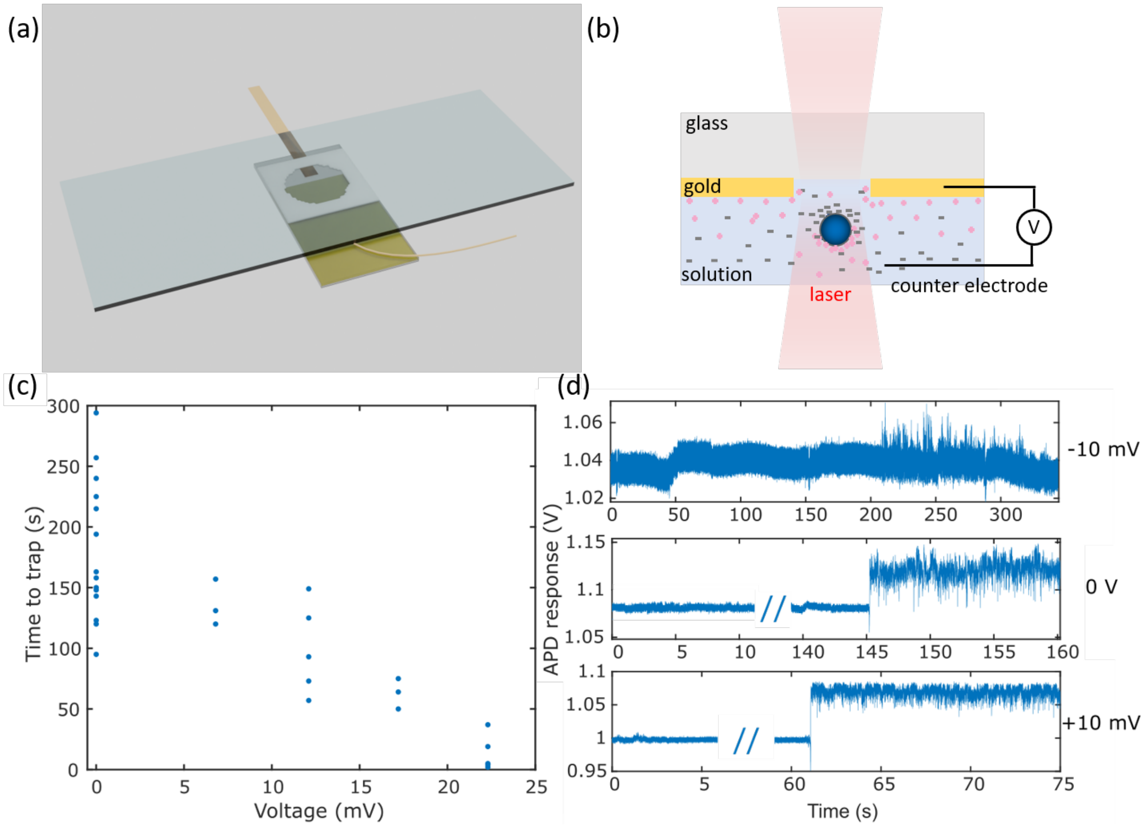

Figure C.4: (a),(b) Method of sample preparation and electrode connections for applying voltage in electrophoresis technique. (c) Time-to-trap versus applied DC voltage for 20 nm polystyrene. (d) Trapping event of 20 nm polystyrene sphere at different DC voltages. Copyright ©2023 American Chemical Society

to the trapping nanoaperture in a gold film (more nanofabrication time/cost); using a fragile thin membrane for the nanopore (more delicate); and, using two chambers (more complicated). Considering these challenges, the present approach does not add nanofabrication steps, uses a robust substrate and uses a simple single chamber.

This study shows that the location of the counter electrode plays an important role. In most works, the counter electrode is placed within the solution, and this can lead to repulsive electro-osmotic flow [45]. If we aim to direct the particles to the trapping site, repulsion is not desirable. Dielectrophoretic effects are sensitive to the location of the counter electrode. The field gradient changes when moving the counter electrode from the solution to the opposite side of the film. If the counter electrode is placed in solution, the aperture in the metal plate sets up an opposing dipole to the applied normal electric field and therefore, the field decreases towards the aperture (negative gradient) [151]. This causes a repulsive dielectrophoretic force (assuming the Claussius Mossitti factor is positive for a highly polarizable particle). On the other hand, placing the counter electrode on the opposite side of the metal film creates a positive field gradient that attracts particles by dielectrophoresis, which would lead to faster trapping as seen in the experiments for this configuration.

We believe that part of the reason dielectrophoresis works so well is because the proteins are highly polarizable (but perhaps not as polarizable as some other particles, like nucleic acid molecules) in part because of their surface water interactions; however, this is a topic of ongoing investigation [153]. We confirmed both positive and negative voltages worked, proving that this was dielectrophoresis and not electrophoresis. At the time of review, we became aware of a preprint using applied field to manipulate and trap extracellular vesicles with a double-nanohole. [154] In that work, the double nanohole was surrounded with many holes and these additional holes pushed the particle towards the center where the double nanohole was located. Therefore, a repulsive force was seen from the presence of the external apertures when the counter-electrode was in solution for that work. Without the holes surrounding, this would not help trapping. Their interpretation of the results are slightly different from ours and this may be debated in future works; however, the experimental results are clear and consistent with our work.

We have also used this technique to analyze various proteins, as done in the past, making use of noise amplitude and time constant to get information about the protein size (both from a hydrodynamic and optical scattering point of view, which are in general different quantities). The results are presented in the Supporting Information Figure C.7 and C.8. Generally, the proteins showed linear increase in the noise amplitude with particle size, and a -2/3 exponent dependence with time constant (which was extracted for various proteins by fitting a Lorentzian to the power spectrum of the trap data, to retrieve the corner frequency of the power spectrum density of the thermally driven fluctuations). An exception was Neuropeptide Y, which showed significantly higher than expected noise amplitude but it did fit the time constant curve well. The larger fluctuations are possibly because of its rod-like shape and flexible tail end [155]. Of interest, neuropeptide Y is the smallest protein we have trapped so far, at only 4 kDa.

In conclusion, a simple modification of placing an external counter electrode to the double-nanohole containing metal film allows for an order of magnitude faster trapping of unmodified proteins in solution. The speed-up was observed for both negative and positive potentials, showing that this is a dielectrophoretic effect. The approach was most effective at DC applied voltage. By contrast, putting the counter electrode in solution did not generally speed up trapping of proteins; it did lead to voltage dependent faster trapping of polystyrene spheres, with increasing applied voltage, which we attribute to changes in the repulsive surface potential since it only worked for positive applied voltages. Since rapid trapping is required for high-throughput analysis of proteins and their interactions, this is a promising approach for the application to single molecule biosensors based on NOTs.

C.2 Supporting information for "Fringe dielectrophoresis nanoaperture optical trapping with order of magnitude speed-up for unmodified proteins"

Figure C.5 shows a typical scanning electron microscope image of the double nanohole used for protein trapping.

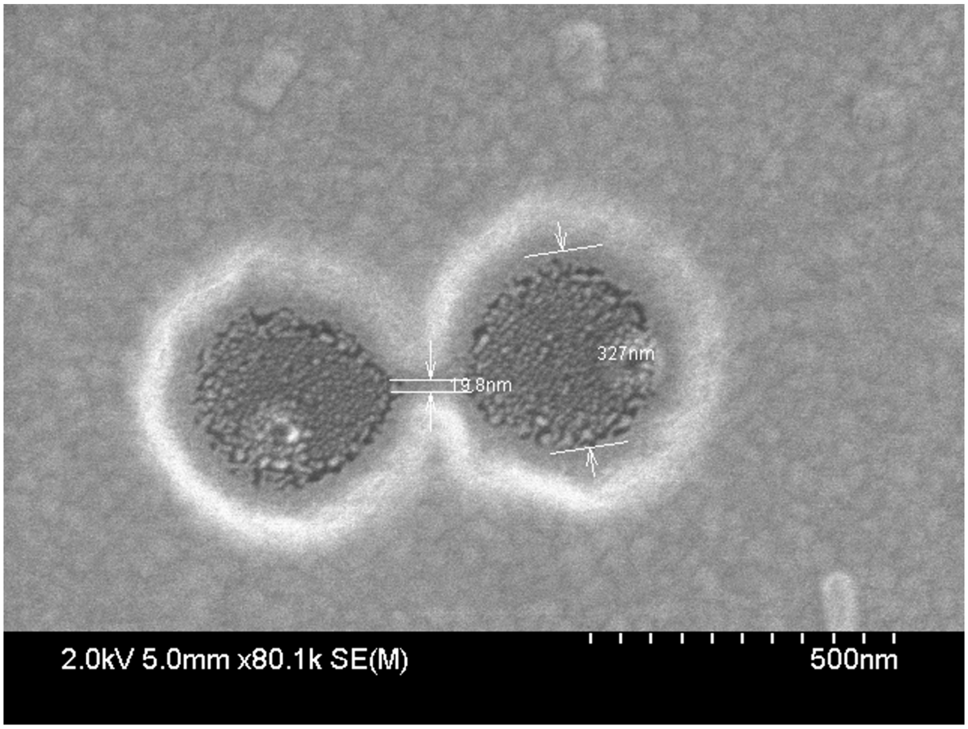

Figure C.5: A typical electron micrograph of the sample. Copyright ©2023 American Chemical Society

Figure C.6 shows a typical trapping signal obtained for Neuropeptide Y (4 kDa), the smallest protein we have trapped so far.

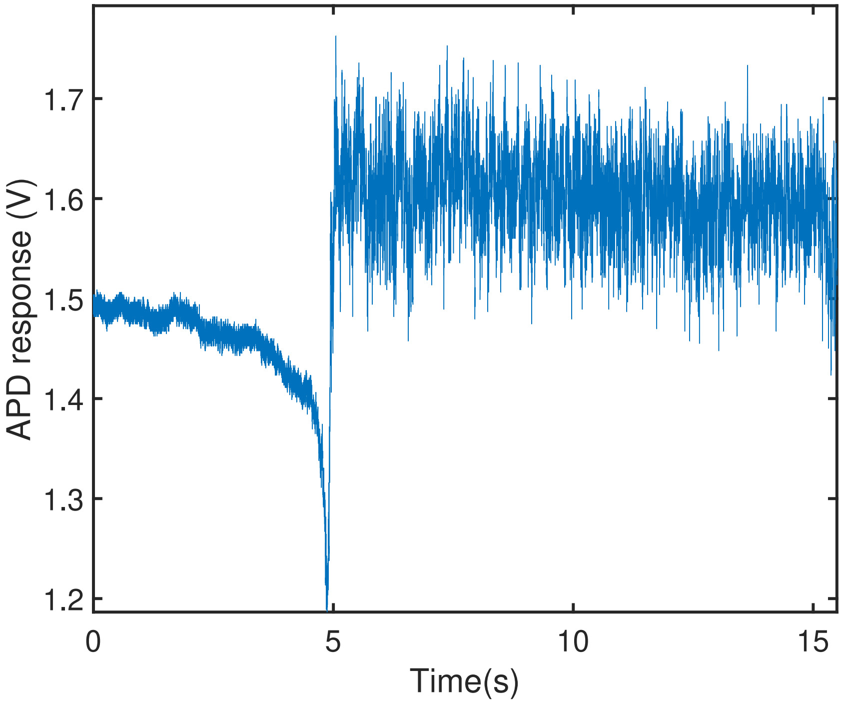

Figure C.6: Typical trapping signals obtained for neuropeptide y (4 kDa). Copyright ©2023 American Chemical Society

Figure C.7 shows the time constant extracted for various proteins from the corner frequency of the power spectrum plot. The fit on the log-log plot is -0.64, whereas a simple theory predicts -2/3 [35].

Figure C.8 shows a linear dependence of noise amplitude with protein mass, except the smallest protein trapped, neuropeptide Y (4 kDa). The neuropeptide Y showed a much larger than expected noise signal, which may be related to its has a rod-like shape and a highly mobile end [155]. The time-constant for this protein, however, was suitable in sizing.

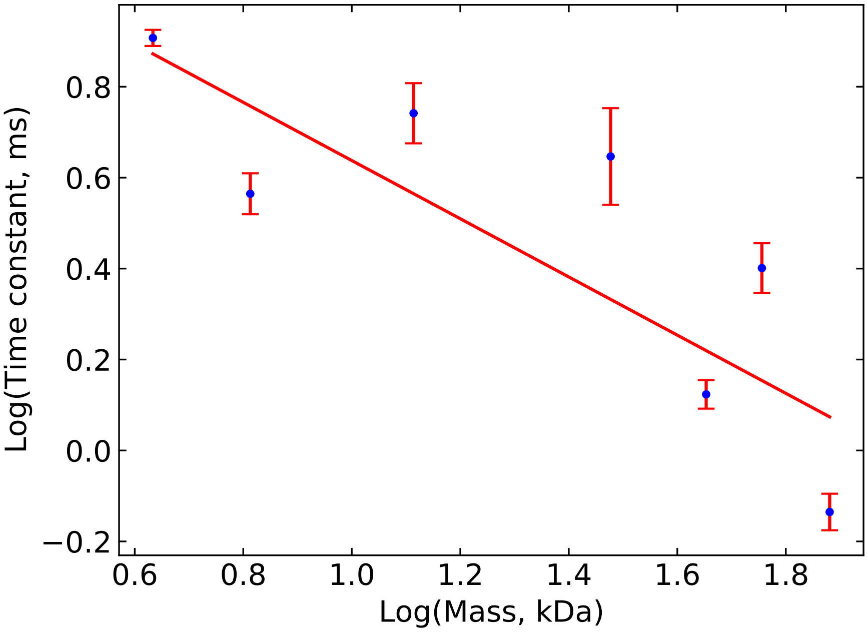

Figure C.7: Time constant as a function of protein mass. Copyright ©2023 American Chemical Society

Figure C.9 shows typical power spectral density plots and Lorentzian fitting for neuropeptide Y and conalbumin. The fitting to Lorentzian functions gave more robust time constant fitting than fitting exponentials that we have used in the past [35].

Figure C.10 shows the a Gaussian probability distribution fit to the noise amplitude histogram for neuropeptide Y.

Figure C.11 shows the voltage dependent trapping of carbonic anhydrase and bovine serum albumin for the counter electrode in solution. Bovine serum albumin did not show a speed up on the time-to-trap with applied voltage.

We used a COMSOL Multiphysics model (finite element method) to simulate the

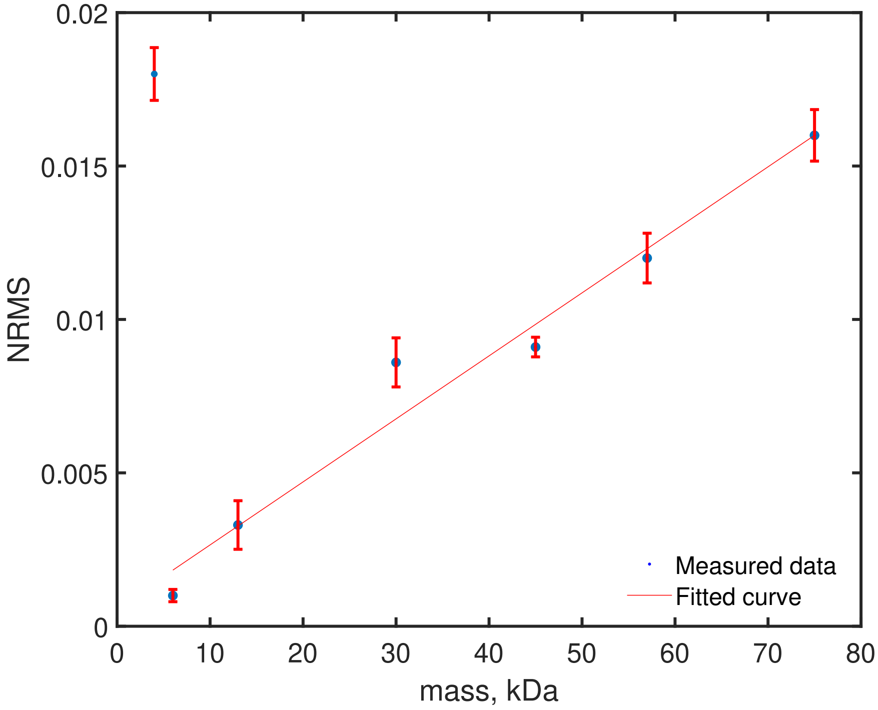

Figure C.8: Normalized root-mean-square (RMS) of trapped signals, with zero corresponding to an empty trap. Copyright ©2023 American Chemical Society

distribution of electric fields around the aperture when the counter electrode is on the other side of the glass or in solution. The model consists of 3D geometry representing double nanohole aperture with radius of 165 nm and cusp size of 20 nm in a gold film with thickness of 70 nm. The film is between water at the bottom and glass at the top. The voltage of the gold was set to -0.5 V and the counter electrode to 0 V in both cases.

Figures C.12 and C.13 show the electric potential simulated in COMSOL for x-z and y-z planes, showing a concentration around the aperture when the counter electrode is placed on the glass side. Figures C.14 and C.15 show the electric potential

Protein	Molecular weight (kDa)	Isoelectric point	Distance from pH 7.4	Zeta potential (mV)
Aprotinin	6	10.5[156]	+3.1	
β-amylase	57	5.0 [157]	-2.4	
Carbonic anhydrase	30	5.4 [158]	-2.0	
Conalbumin	75	6.5 [159]	-0.9	-1.0 [159] *
Cytochrome c	12	9.6 [160]	+2.2	11.7 [161]
Neuropeptide Y	4	7.9 [162]	+0.5	
Ovalbumin	40	4.5 [163]	-2.9	-19.5 [164]
Ribonuclease	13	9.3 [165]	+2.2	-0.9 [165]

Table C.1: Isoelectric points and zeta potentials for proteins studied in this work, sourced from literature. *Note: not measured in PBS buffer.

	Voltage ON before laser	Voltage OFF before laser
Aprotinin	37	110
	63	51
	85	89
Ovalbumin	59	49
	33	27
	42	45

Table C.2: Time to trap values in seconds for proteins when dielectrophoresis voltage is switched on before or after laser.

simulated in COMSOL for x-z and y-z planes, showing field reducing around the aperture when the counter electrode is placed in solution.

Figure C.16 is a schematic showing the control measurement where voltage is switched on before or after the laser.

Table C.1 contains isoelectric points and zeta potentials for the proteins studied in this work.

Table C.2 contains values for the time to trap for events where the voltage is switched on before or after the laser.

Figure C.17 depicts the equivalent circuit model for the dielectrophoresis optical tweezer.

Figure C.18 shows a comparison of the simple arithmetic mean of the time to trap of 8 proteins in three different states of applying no voltage, DC voltage, and AC voltage to the sample. The error bars show the standard deviation of the data.

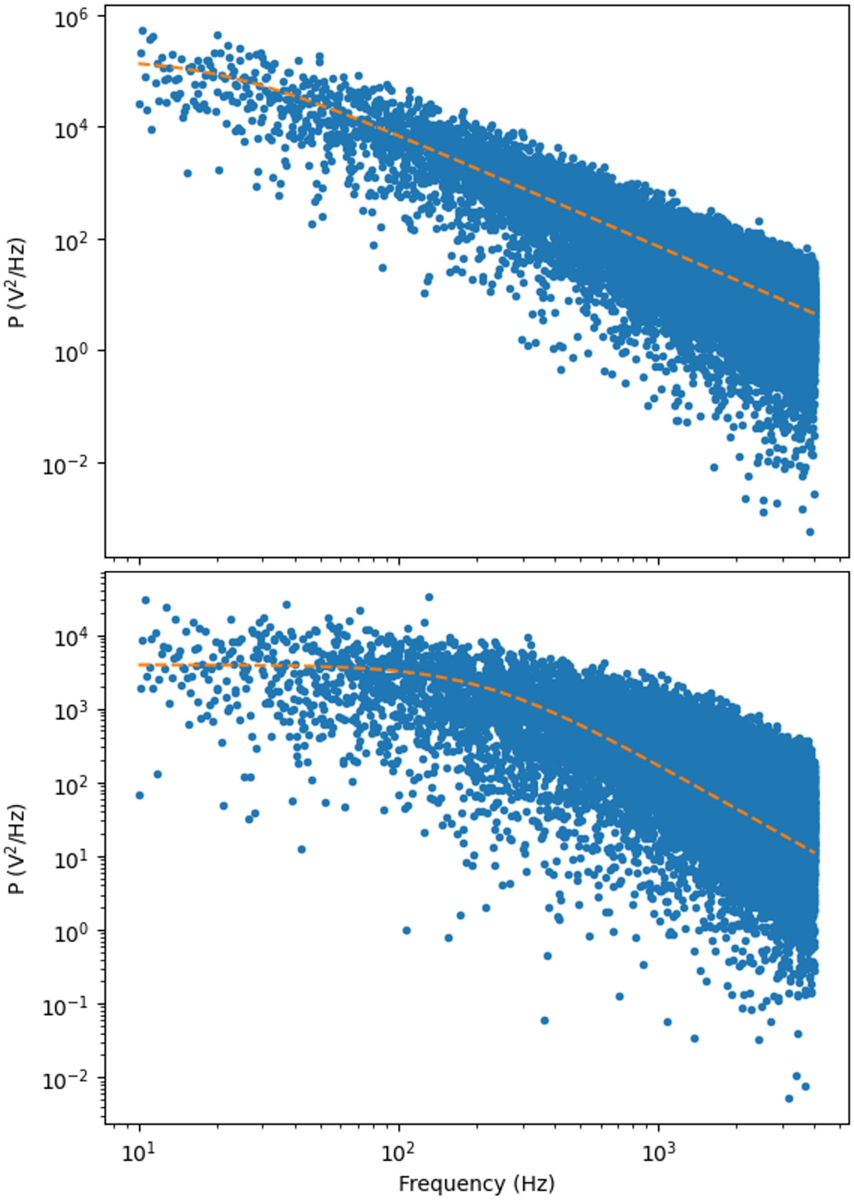

Figure C.9: Comparing power spectral density of NPY (Top) and conalbumin (Bottom). Copyright ©2023 American Chemical Society

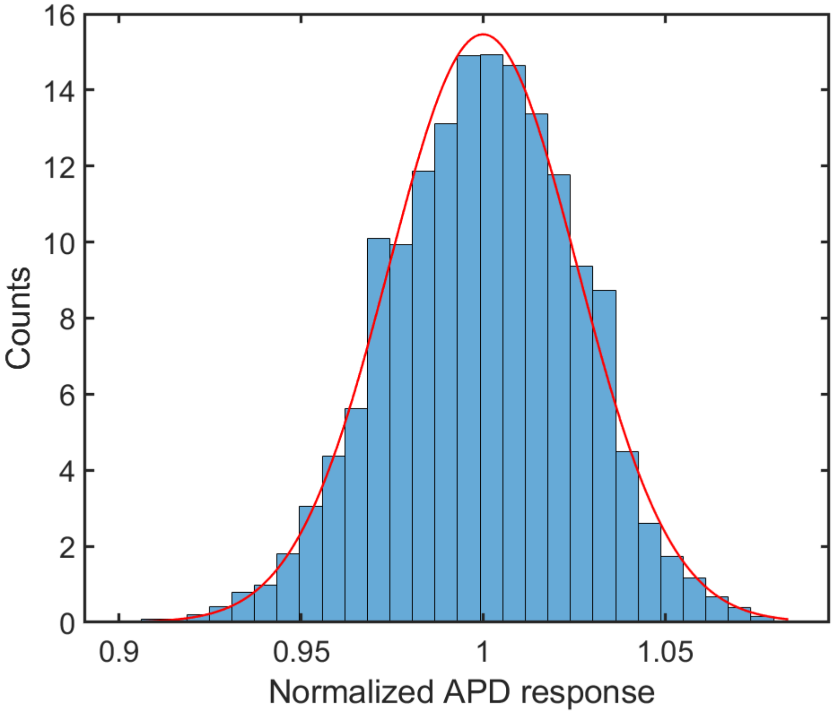

Figure C.10: Normalized histograms (blue) and Gaussian probability density functions (red line) of trapped signal for neuropeptide. Copyright ©2023 American Chemical Society

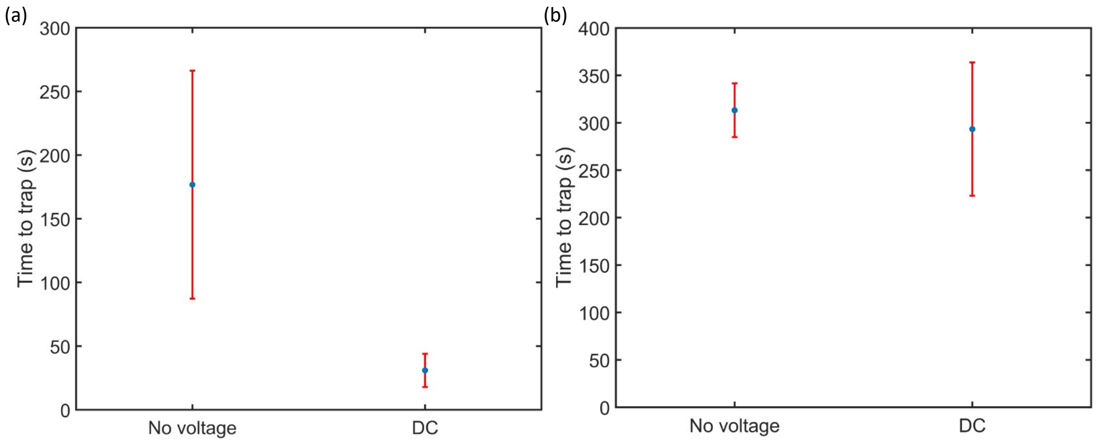

Figure C.11: Comparing time to trap with applied DC voltage and with no voltage applied for proteins: (a) carbonic anhydrase (b) bovine serum albumin. Copyright ©2023 American Chemical Society

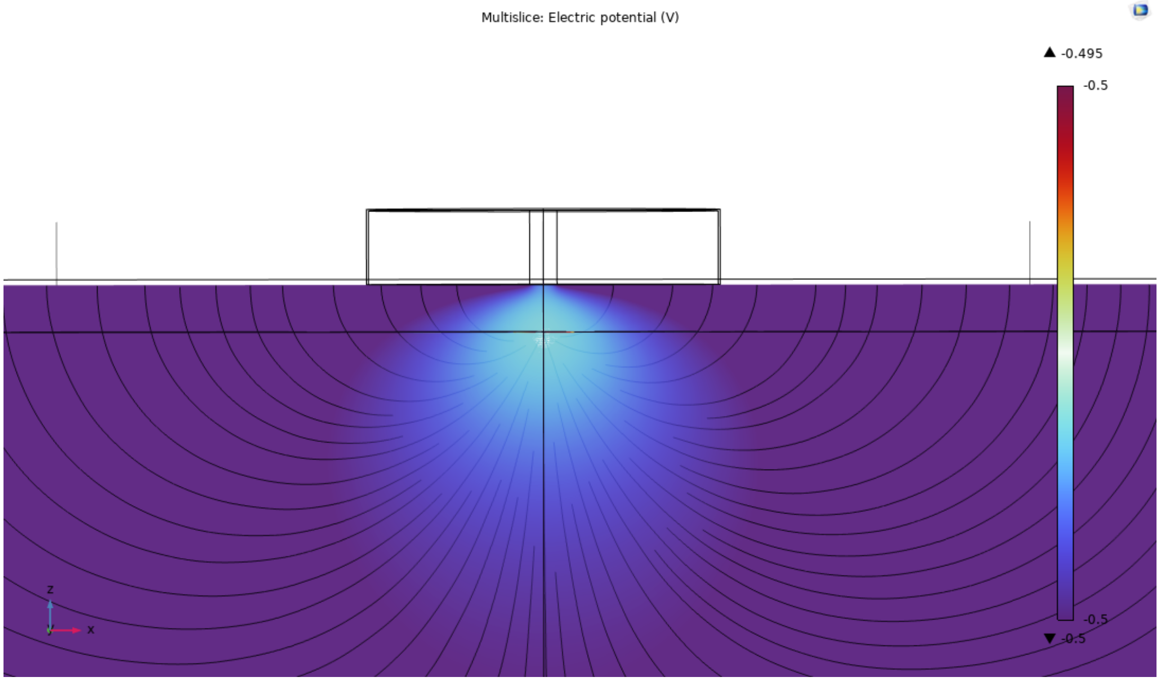

Figure C.12: Electric potential from xz view when one electrode is gold and one at the top of glass.Copyright ©2023 American Chemical Society

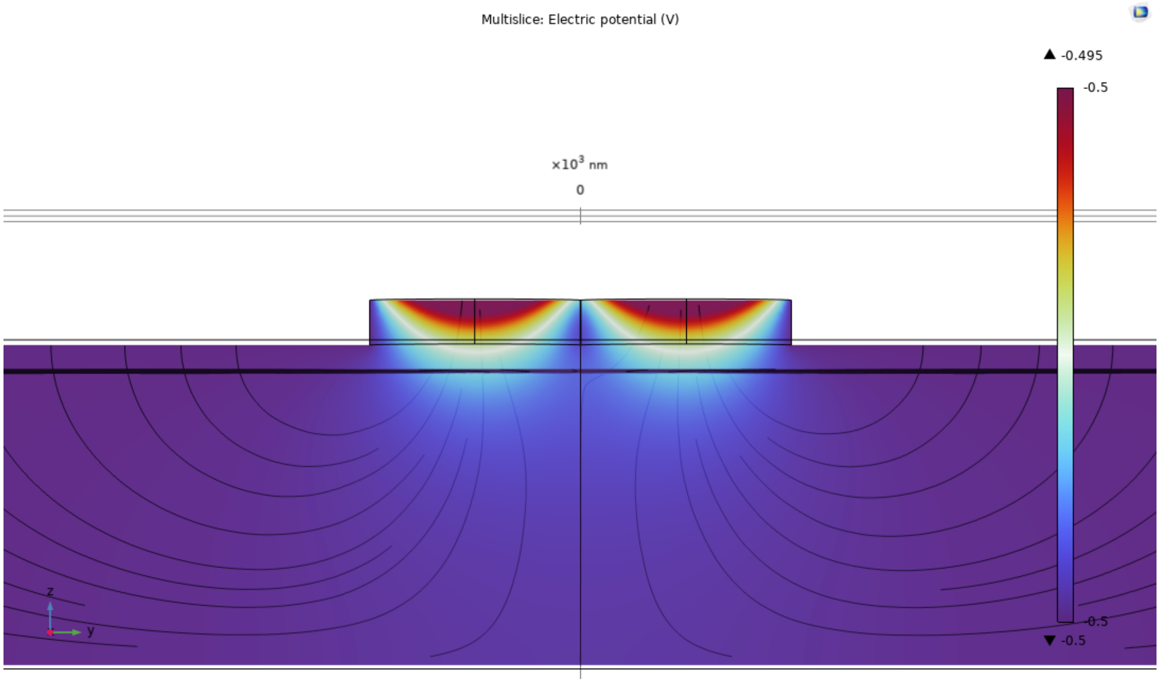

Figure C.13: Electric potential from yz view when one electrode is gold and one at the top of glass.Copyright ©2023 American Chemical Society

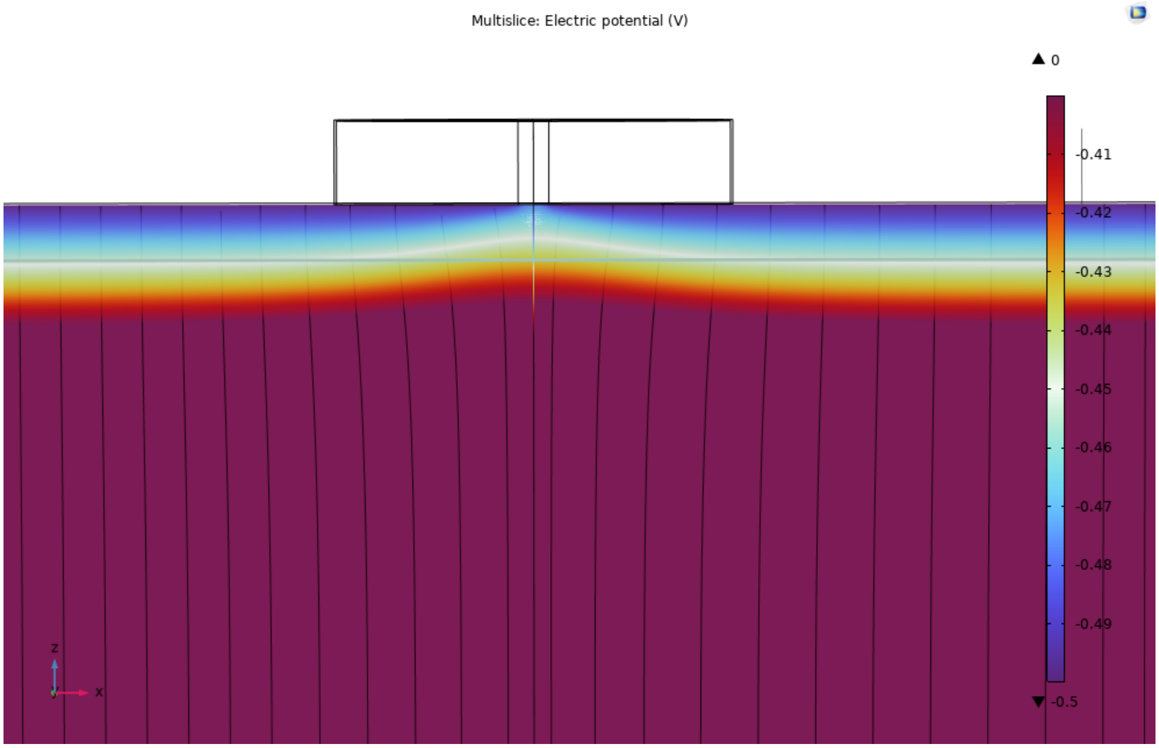

Figure C.14: Electric potential from xz view when one electrode is gold and one in the solution.Copyright ©2023 American Chemical Society

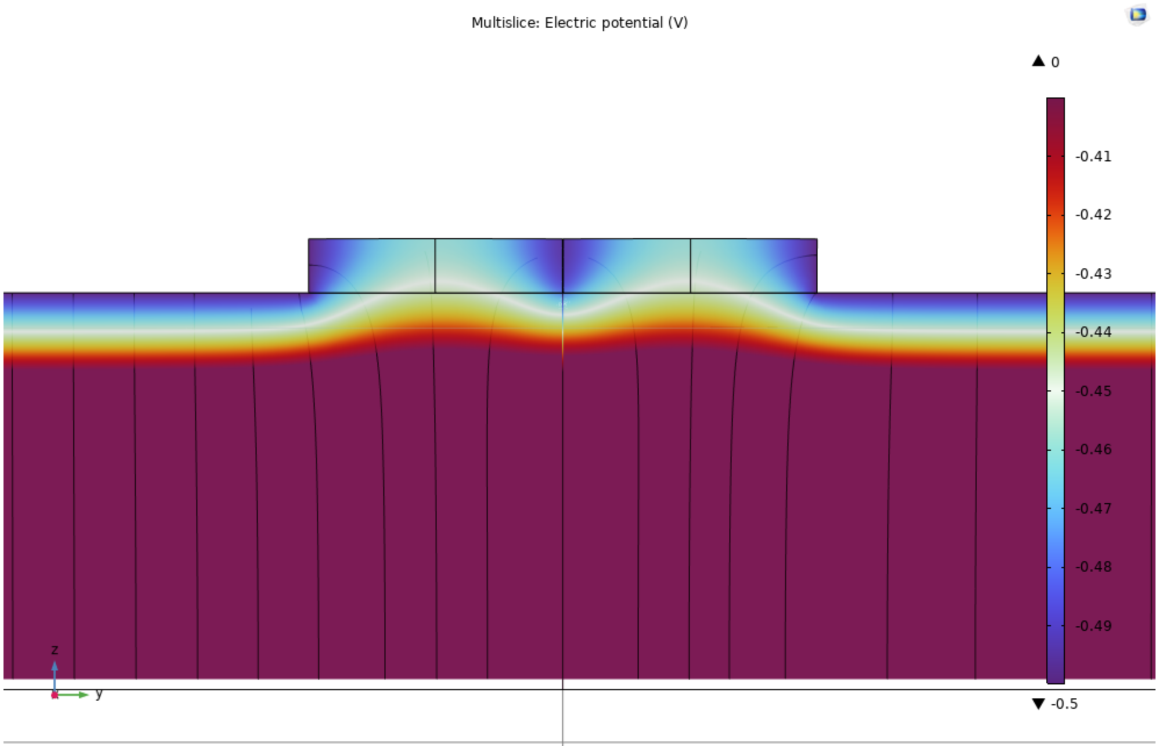

Figure C.15: Electric potential from yz view when one electrode is gold and one in the solution.Copyright ©2023 American Chemical Society

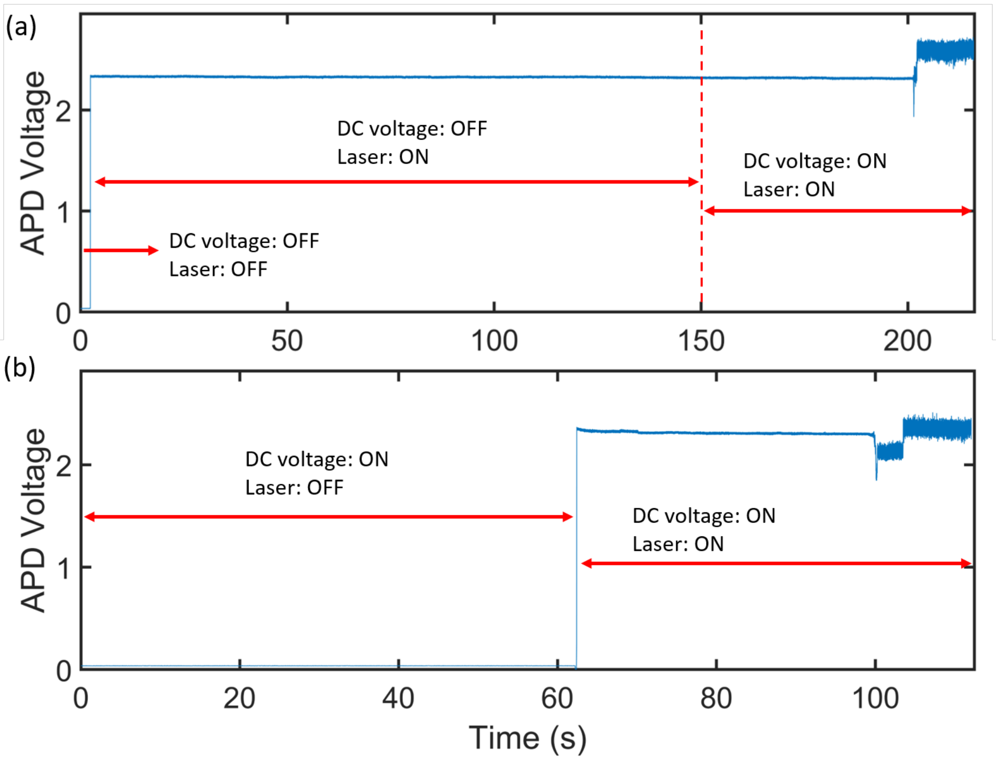

Figure C.16: Separating dielectrophoresis effect from optical trapping behavior (a) applying Voltage after laser (b) having the voltage before making the laser ON.Copyright ©2023 American Chemical Society

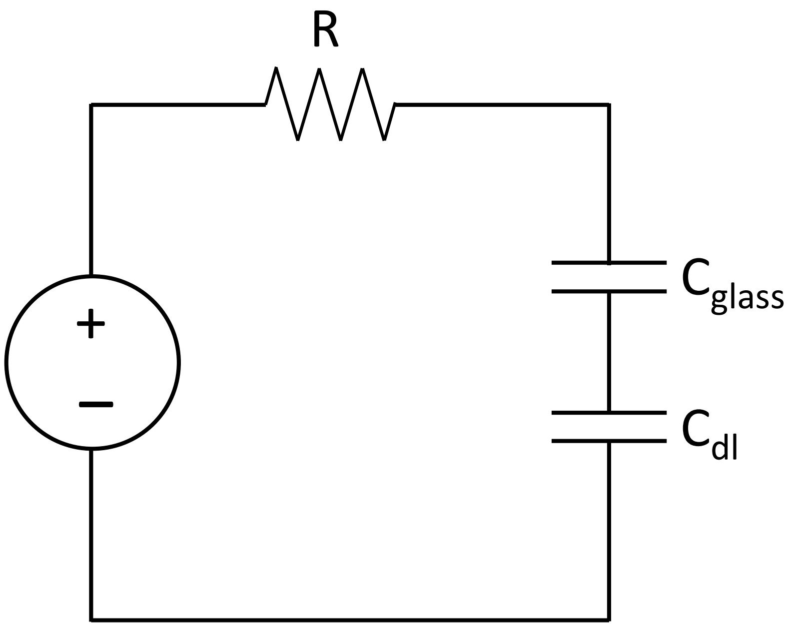

Figure C.17: Equivalent circuit model of the dielectrophoresis optical tweezer.Copyright ©2023 American Chemical Society

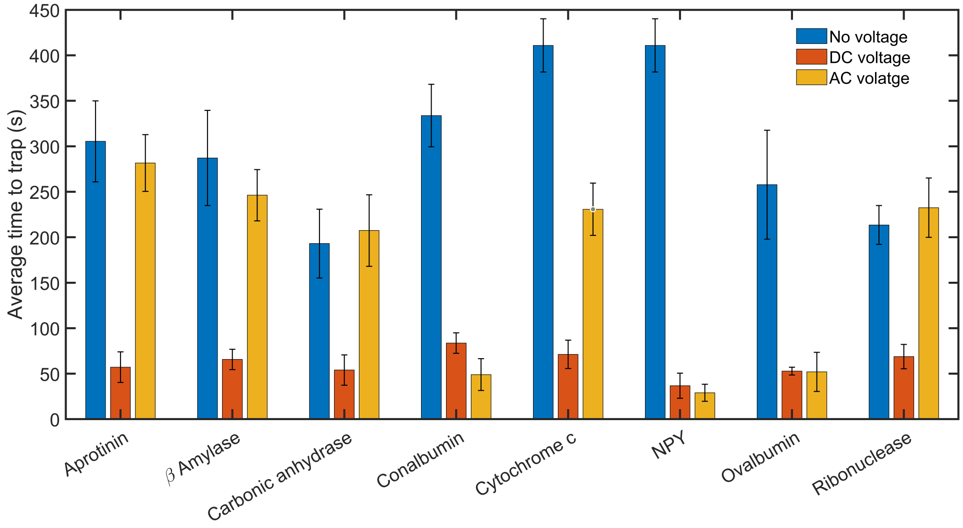

Figure C.18: Average time-to-trap of different proteins for three states of no voltage, applied DC and AC voltages. Copyright ©2023 American Chemical Society